A Three-Dimensional MOT of YO Towards Narrow-Line Cooling

by

Alejandra L. Collopy

B.S., Stanford University, 2010

M.S., University of Colorado, 2012

A thesis submitted to the

Faculty of the Graduate School of the

University of Colorado in partial fulfillment

of the requirements for the degree of

Doctor of Philosophy

Department of Physics

2018

This thesis entitled:
A Three-Dimensional MOT of YO Towards Narrow-Line Cooling
written by Alejandra L. Collopy
has been approved for the Department of Physics

Jun Ye

Eric Cornell

Date

The final copy of this thesis has been examined by the signatories, and we find that both the content and the form meet acceptable presentation standards of scholarly work in the above mentioned discipline.

Collopy, Alejandra L. (Ph.D., Physics)

A Three-Dimensional MOT of YO Towards Narrow-Line Cooling

Thesis directed by Jun Ye

Laser cooling and magneto-optical trapping of neutral atoms has been a driving force in physics over the last few decades by providing an efficient method to produce cold and dense samples of cold atoms. Polar molecules which can have strong, long-range dipolar interactions and possess more rich internal structure promise a wide range of new physics and chemistry studies if they can be controlled efficiently. Until recently, the only way to achieve sub-milliKelvin level temperatures in molecules was to associate two precooled atomic species, which while very effective, has a firm bound on the chemical diversity accessible. While laser cooling of molecules relies on fortuitous molecular properties, it will significantly increase the choices of species available for molecular cooling.

In this thesis I present the improved optical deceleration of the molecule yttrium monoxide (YO) and the loading of molecules into a 3-D magneto-optical trap (MOT). By making an improved choice of repumping scheme from our groups' previous work, our photon scattering rate has been increased. By also improving our buffer gas cell source, we produce a much larger flux ($\sim$2000 times higher) of slowed molecules at 5 m/s to reach the trapping region. I have designed and implemented 3-D MOT field coils operating at 5 MHz, and demonstrated a successful operation of a 3-D MOT. This is the first 3-D laser trapping of an oxide and the first of a molecule with an electronic state intermediate to the main cycling transition states.

I have also performed a study of the transition from the ground state to the intermediate electronic state, which has a narrower linewidth of $\sim$150 kHz, in contrast to the main cycling transition's linewidth of 5 MHz. This transition is well suited to second-stage narrow line cooling after loading molecules with the main MOT transition, which will allow direct laser cooling of a molecule to the 10 uK regime.

Dedication

For my family: past, present, and future

Acknowledgements

Words could never be enough, but I'll give it a try. So many different people have gotten me to where I am today, and I am truly grateful. Without your help, guidance, and commiseration graduate school would have been a very different experience, and the work described herein could never have come to be.

Firstly, I'd like to thank my advisor, Jun Ye. You have always been the optimist giving us confidence that someday we actually would succeed at trapping molecules, even when the path forward was murky. You always teach us so much, from how to be an effective scientific communicator to giving your invaluable perspective on how to solve the many problems that crop up in day to day scientific advances and setbacks. Thank you for your resolve and your patience.

I've had the great fortune to work with many wonderful labmates over the years. In particular, I'd like to thank Matt Hummon for being an excellent teacher, from how to assemble vacuum chambers to optical alignments. Mark Yeo inducted me into the land of the frequency comb and laser locking, without which the experiment couldn't continue to exist. Bo Yan was forever cheerful and helping to fix the many broken pieces of equipment that would otherwise bring us to a halt. Yewei Wu tackled the problem of learning how the entire system works, and succeeded with flying colors. It is in his hands that I confidently leave the future of our experiment. Thank you so much for your enthusiasm and humor. In the last couple of years I've gotten to work with two great postdocs, Shiqian Ding and Ian Finneran. They are both very capable and anxious to push on to new experimental frontiers. I can't wait to see where it takes them. Our sister experiment, OH, has been manned with two graduate students during the majority of my time here, Dave Reens and

Hao Wu. It's been amazing sharing a lab, ideas, and molecule angst with you guys.

There are many others in JILA with whom I've had great problem solving discussions, interesting physics ideas, and most importantly, laughs. They've provided such great advice and support (in no particular order): Ed Marti, Michelle Miller, Cory Goldsmith, Yomay Shyur, Craig Benko, Brian Lester, Bryce Bjork, Shimon Kolkowitz, Ben Spaun, Will Cairncross, Cathy Klauss, Hans Green, Corey Keasling, J.R. Raith, James Fung-A-Fat.

I'd like to thank my family, Aria, Pam, and Paul Collopy for always loving, supporting, and being there for me. You were the first to instill an excitement for science in me and I'm so glad. I'm also very thankful for my soon-to-be family, Tom, Sherry, and Alexander who have so overwhelmingly welcomed me.

Finally, I'd like to thank my fiance Andrew for hanging in there through the frustrations and late nights and being there for all the joys and excitments. I can't wait for our future adventures.

Contents

Chapter

Tables

Table

Figures

Figure

Chapter 1

Overview

1.1 Why cold molecules?

Cooling of molecules has far-flung applications, from tests of fundamental symmetries [1, 2, 3], study of long range anisotropic interactions [4], to cold chemistry [5, 6]. The more complex structure of molecules as compared to atoms, though it provides a rich field of study, also makes difficult the cooling methods readily available to atoms. Indirect methods have so far produced the coldest molecules, via magneto-association and adiabatic transfer [7]. Unfortunately, the number of species that can be produced in this way is limited, and so we must look to direct cooling methods to support a wider range of molecular species. Cold molecular beams can be produced via supersonic expansion [8] or from a cryogenic buffer gas beam source [9]. Such beams can be decelerated with techniques such as Stark deceleration [10, 11], Zeeman deceleration [12], or via centrifugal deceleration [13]. From a low velocity beam, a two photon process has been used to directly load a magnetic trap [14].

For a long time, it was thought that laser cooling of molecules was impractical due to the large number of states and therefore lasers required to implement an optical cycling transition capable of many photon scatters. However, in 2004 it was proposed [15] that a large class of molecules has sufficently diagonal Franck-Condon factors to be amenable to laser cooling. The identified molecules were diatomic hydrides or halides. In 2008 the first concrete proposal was made for a class of cycling transitions that through angular selection rules, avoids all dark states for molecules, enabling quasi-closed cycling and so the scattering of many photons [16]. It was also noted that these laser coolable

molecules could include diatomic carbides, oxides, or sulfides, suggesting that the potential chemical diversity for laser-cooled molecules is quite large. In the intervening time, optical cycling has been demonstrated in a number of diatomic species, leading to the demonstration of laser cooling in the SrF molecule[17], radiation pressure slowing in SrF [18], CaF [19], and YO molecules [20]. This laid the foundation for the realization of magneto-optical trapping in two dimensions of YO in 2013 [21] and in three dimensions for SrF in 2014 [22], followed by CaF in 2017 [23, 24]. The last few years have been truly exciting on the cold molecule frontier! For polyatomic molecules which are similar enough in structure to the identified diatomics, quasi-cycling transitions can also be realized. In this way one dimensional Sisyphus [25] cooling has been performed on the SrOH molecule (which is isoelectronic to SrF). Additionally, it has been proposed that the optical bichromatic force [26] or ultrafast stimulated slowing [27] can be used for molecular beam deceleration and cooling [28]. The lowest temperature realized with these direct cooling techniques is so far that of the magneto-optical trap (MOT) followed by a sub-Doppler cooling stage of a blue [29, 30] or gray [31] optical molasses with temperatures reaching the $\sim$50 μK level.

I have had the great privilege of working on this experiment from near its inception. By building up a buffer gas source and lasers to address the first three vibrational levels in YO, we were able to demonstrate transverse Doppler cooling of YO to $\sim$10 mK. By further implementing a 2-D quadrupole field coil resonant at 2 MHz, we showed that the magneto-optical effect worked with our cycling transition in YO, and further reduced the transverse temperature to the 2 mK level [21]. Logistically, some experimental aspects are simplified by working with a molecular beam, but in order to move forward to 3-D trapping we needed to implement deceleration of the molecules produced by our buffer gas cell. We utilized the same cycling transition that allows for laser cooling to optically decelerate the molecules from production speeds of $\sim$70 m/s to less than 10 m/s, using a combination of frequency chirping of the laser beams and white-light sidebands on the slowing light [20].

In this thesis I present the first three dimensional MOT for YO. This is the beginning of the expansion beyond fluorides to the wide range of species that laser cooling of molecules promises to

open. By improving our group's earlier slowing results [20], and guided by principles of our 2D MOT implementation [21], we designed and implemented a slowing and trapping sequence that yields approximately 1000 molecules in our trap. Looking to the future, while a short-lived excited state is desirable for quickly slowing a molecular beam, a viable option to decrease the final temperature of the MOT is to use a narrower linewidth transition [32, 33]. Having recently implemented a MOT for YO on the broad main cooling transition, we also identify a transition in YO that is amenable to use in narrow-line cooling [34]. We anticipate that this transition will enable narrow line cooling to the Doppler temperature $T_D = \hbar\gamma/2/k_B \approx 5\ \mu$K where $\hbar$ is the reduced Planck constant, γ is the linewidth of the transition, and k_B Boltzmann's constant. Our proposed scheme will only require the addition of one laser to the broad cooling setup of the YO molecule.

1.2 Cooling process

The process to take YO from initial production temperatures down to the μK scale involves a number of steps, as depicted in Figure 1.1. The initial temperature of YO after ablation is high

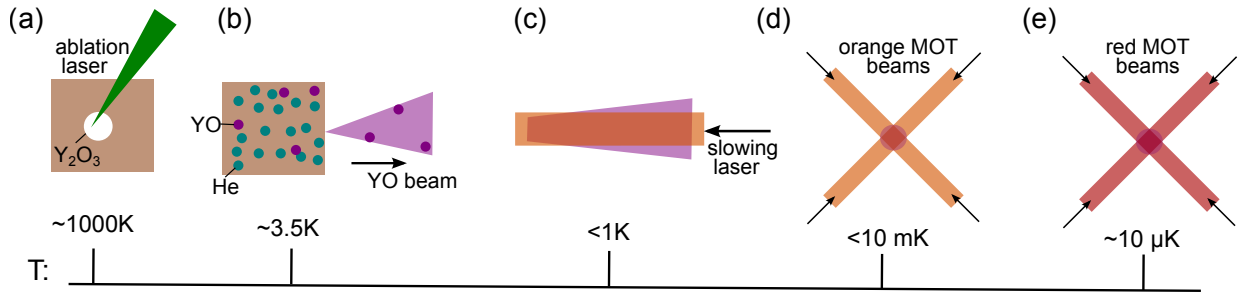

Figure 1.1: Cooling process schematic. After production via ablation (a), YO molecules thermalize with helium at 3.5 K in a cryogenic buffer gas cell (b). Upon exiting, the beam has velocity ∼120 m/s. Longitudinal slowing produces molecules <5 m/s (c), loadable into a MOT. The orange MOT will produce cold molecules less than ∼10 mK (d). Narrow line cooling can then be performed on the red transition (e). Steps (a) through (d) have been implemented experimentally, with (e) being our next planned step forward

both rotationally and translationally, whereas any optical cycling scheme requires a large number of molecules in a single state. To meet this requirement, we utilize a cryogenic buffer gas cell [21] to produce cold YO molecules. The buffer gas cell is anchored to a 3.5 K cold plate and helium gas

is constantly flowed in to maintain a high density ($\sim 10^{16}/\mathrm{cm}^{-3}$) of helium in the cell. The helium collisions with the cell walls cool the helium, and YO collisions with the helium buffer gas then rotationally, vibrationally, and translationally cool the YO molecules. The net result is a beam of YO molecules with forward velocity distribution peaked at 120 m/s with a 40 m/s full width at half maximum. Longitudinal slowing of the YO beam is accomplished [20] with a frequency chirped slowing beam, resulting in a population of YO molecules with speeds under 10 m/s, sufficiently slow to load into our MOT. In the future, we plan to perform secondary laser cooling with a narrow-line MOT, analagous to the methods demonstrated for several atomic species [33, 35, 36, 37, 38, 39, 40].

1.3 Overview of thesis

In order to provide an understanding of the YO molecule and how we can scatter many photons with it, I detail the level structure and several different repumping schemes in Chapter 2. In Chapter 3 I explain the nuts and bolts of the experimental apparatus that we use to produce, decelerate, trap, and image molecules, including the laser, microwave, photon collection, cryogenic, and vacuum systems. We systematically studied several characteristics of our buffer gas cell, such as geometry, nanopowder coatings, the addition of oxidizers, and the ablation of Y metal instead of Y_2O_3. These studies are detailed in Chapter 4. In the intervening years since our last slowing publication [20] we have achieved a number of improvements to the slowing efficacy of our system. Detailed in Chapter 5, these improvements range from transitioning our cell and laser systems to accomodate a single-stage buffer gas cell rather than a two-stage cell, to changing the repumping scheme used to decelerate the molecules, to changing the repetition rate of the experiment. Chapter 6 explains the design considerations, construction, impedance matching, and characterization of the AC magnetic field coils that make up our trap. Results of loading molecules into our trap are detailed in Chapter 7, where I explain the sequence we use for trapping and perform characterizations of the loaded molecules. Finally, our future goals are described in Chapter 8, where I analyze a transition and a repumping scheme that we will use to perform narrow-line cooling in YO.

Chapter 2

Level structure and optical cycling transitions in YO

2.1 Level structure of YO

Developing an understanding of the level structure of YO is necessary for any effort to slow or trap the molecules. This structure determines the frequencies of the lasers we use to interact with the molecules, as well as determining the ability to scatter many photons and so exert a reasonable force. The molecule YO has three electronic states that are of primary concern to us: the $X^2\Sigma$ ground state, the $A^2\Pi$ excited state, and the $A'^2\Delta$ intermediate state, as shown in Figure 2.1(a). For describing the angular momentum coupling in these states we follow the notation used by Brown and Carrington [41]. When discussing a specific value of angular momentum, the factor of $\hbar$ is omitted. For the states we consider in YO, we have electronic spin $S = 1/2$ and nuclear spin $I= 1/2$. Only the Y atom has nuclear spin; the oxygen atom's nuclear spin is zero. Electron orbital angular momentum is labeled $\mathbf{L}$, while rotational and total angular momenta are labeled $\mathbf{R}$ and $\mathbf{F}$ respectively. Energy eigenstates of the molecule are frequently superposition states of $\mathbf{R}$, and so we use intermediate angular momenta to describe the states: $\mathbf{J} = \mathbf{F} - \mathbf{I}$, and $\mathbf{N} = \mathbf{J} - \mathbf{S} = \mathbf{R} + \mathbf{L}$. Parity of states is indicated by (+) or (-). As well as possessing an array of rotational levels, each state also has a ladder of vibrational levels labeled with quantum number v.

We begin by considering the electronic ground state $X^2\Sigma$. Because $\mathbf{L}$ is 0, there is no spin-orbit coupling, and so the state can be described by Hund's case ($b_{\beta S}$). The effective Hamiltonian

for this case that describes the coupling of momenta in this state is:

$$H_{\text{eff}} = \gamma \mathbf{S} \cdot \mathbf{N} + b\mathbf{I} \cdot \mathbf{S} + cI_z S_z \tag{2.1}$$

where $\gamma = -9.2$ MHZ, b $= -763$ MHz, and $c = -28$ MHz, representing the spin-rotation, Fermi contact, and electron-nuclear spin dipolar interaction respectively [42]. The strong Fermi contact interaction couples the electron and nuclear spin to form intermediate angular momentum $\mathbf{G} = \mathbf{I}+\mathbf{S}$. The total angular momentum is then formed by the additional coupling of $\mathbf{N}$ through the spin-rotation interaction yielding $\mathbf{F} = \mathbf{G} + \mathbf{N}$. We also note for Σ states, orbital angular momentum $\mathbf{L}$ is zero and so $\mathbf{N} = \mathbf{R}$. For $N>0$, levels can be expressed as a superposition of J levels $J=N \pm 1/2$ ($J=1/2$ for $N=0$). In this state, the rotational splittings are giving by $B \times N \times (N+1)$ with rotational constant B.

The excited $A^2\Pi_{1/2}$ and $A'^2\Delta_{3/2}$ states are well described by Hund's case (a). The rotational states are labeled by angular momenta $\mathbf{J}$ and $\mathbf{F}$, though the hyperfine interaction in these states is small and is not resolvable via optical transitions with the $X^2\Sigma$ state. The quantum number Ω is given by the projection of $\mathbf{L} + \mathbf{S}$ onto the internuclear axis. For Π states, $L=1$, while for Δ states $L=2$. So, for the $A^2\Pi$ states, Ω is $1/2$ or $3/2$, and for $A'^2\Delta$ states Ω is $3/2$ or $5/2$. The value of Ω is indicated by the subscript on the molecular term symbol, e.g. $A'^2\Delta_{3/2}$ has $\Omega = 3/2$. Additionally, the two senses of projections of $\mathbf{L}$ onto the internuclear axis give rise to a pair of states with opposite parity for each J level, called lambda doubling. In the $A^2\Pi_{1/2}$ state, the lambda doubling term, p, is 4.5072 GHz, indicating a splitting of 4.5 GHz for the opposite parity levels in the $J = 1/2$ level [43]. In the $A'^2\Delta_{3/2}$ state, the lambda doubling is expected to be small, and has so far not been measured. These states have rotational splittings given by $B \times J \times (J+1)$. Throughout this thesis single primes (') denote quantum numbers belonging to an excited state, whereas double primes (") denote ground state levels.

The $X^2\Sigma$ to $A^2\Pi_{1/2}$ transition (v"$=0$ to $v'=0$) is at 614 nm, as depicted in Figure 2.1(a). While $A^2\Pi_{1/2}$ primarily decays back to $X^2\Sigma$, it has a $\sim 3\times10^{-4}$ chance of decaying to $A'^2\Delta_{3/2}$ [20]. As will be discussed in more detail in chapter 8 while the $A'^2\Delta_{3/2}$ to $X^2\Sigma$ transition is nominally

electric dipole forbidden, it does in fact occur due to mixing of the nearby $A^2\Pi_{3/2}$ state with the $A'^2\Delta_{3/2}$ state [44]. This narrower transition has a wavelength of 690 nm, and linewidth $2\pi\times160$ kHz [34].

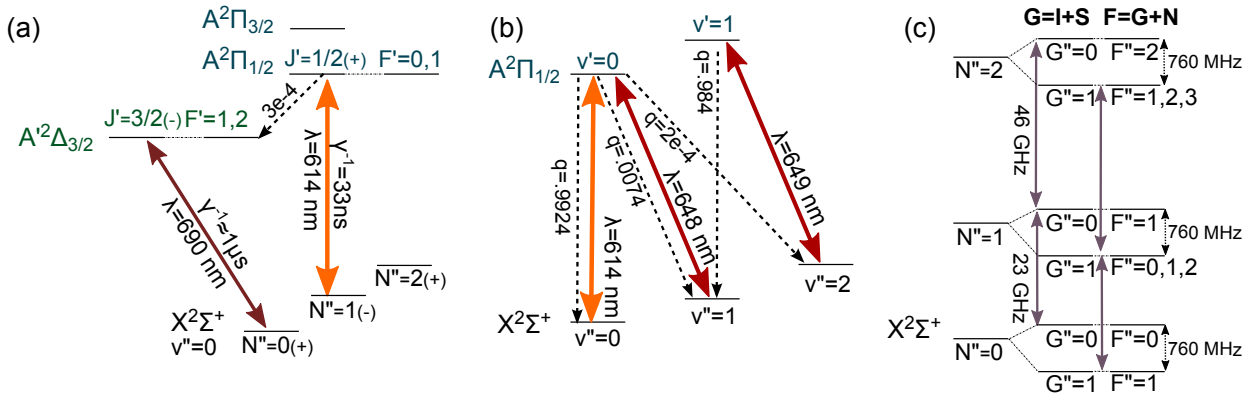

Figure 2.1: Relevant level structure of the YO molecule. (a) Electronic structure and ground state rotational structure. Solid lines indicate the broad (orange) and narrow (maroon) transitions that will be used to make MOTs in YO. (b) Vibrational structure and repumping scheme. Solid lines indicate lasers for first stage cooling (orange) and vibrational repumps (red). Dashed lines show spontaneous decays and are labeled with Franck-Condon factors. (c) Ground state rotational and hyperfine structure. For each G level, F ranges from $|G-N|$ to $|G+N|$.

2.2 Optical Cycling Transition

The transition we leverage as a cycling transition in YO is at 614 nm from $X^2\Sigma$, N"=1 to $A^2\Pi_{1/2}$, J'=1/2, as shown in Figure 2.1(a). We have demonstrated optical cycling using this cooling transition as a one and two dimensional MOT [21], and for molecular beam slowing [20]. Decays to rotational levels other than N"=1 are forbidden by parity and angular momentum selection rules. We address vibrational branching by repumping the v"=1 level directly to the $A^2\Pi_{1/2}$, v'=0 level using 648 nm light (Figure 2.1(b)). The v"=2 level is repumped using a two step process, first exciting it to $A^2\Pi_{1/2}$, v'=1 at 649 nm, which predominantly decays to the v"=1 level, and then allowing the v"=1 repump light to take the molecule back to the v"=0 level. Molecules that decay

to $X^2\Sigma$ via $A'^2\Delta_{3/2}$ end in the N"=0 or 2 levels because of parity and angular momentum selection rules. To maintain cycling, we apply microwave mixing resonant with the N"=0↔N"=1 and the N"=1↔N"=2 rotational transitions, depicted as gray arrows in Figure 2.1(c). In total, we estimate that the setup yields a closed cycling transition up to the $\sim 10^{-6}$ level of enclosure, sufficient to slow and trap a subset of the molecules. Our largest unplugged leaks at this stage will likely be to the v"=1, N"=0,2 levels.

The G"=1: F"=1,2 levels are subject to Zeeman splitting in an applied magnetic field, thus allowing us to not only Doppler cool on the $X^2\Sigma$ state to $A^2\Pi_{1/2}$ state transition, but to also implement a MOT. For this transition, the greater multiplicity of states in the ground state means that coherent dark states can form [45], limiting the total number of photons which can be scattered. In our setup, we avoid this issue by switching our laser polarization at a rate approximately equal to the transition linewidth, eliminating long-lasting dark states. Type-II MOTs like ours, which operate from F" to $F' = F" - 1$, tend to have weaker trapping forces and be larger than their type-I counterparts, which operate from F" to $F' = F"+1$. The final sizes tend to be on the order of 1 mm [46]. We anticipate the final temperature of the orange MOT to be on the order of 500 μK [47, 24], even though the rapid polarization and magnetic field switching in our system should help to negate the weakness of the type-II MOT [48] This is larger than the Doppler temperature $T_D = 110\mu K$, but so far type-II MOTs do not reach the Doppler limit [49, 22]. It has been theorized that the final temperature of type-II MOTs is limited by competition between Doppler and sub-Dopper effects [50].

To achieve our goal of slowing and trapping a large number of YO molecules, we would like to exert large slowing and trapping forces. This requires a laser cooling scheme that can rapidly cycle photons in our molecule, and so we must pay careful attention to the photon scattering rate that we can achieve. The maximum scattering rate that can be realized while exciting an optical transition is determined by the steady state population of the excited state divided by the total number of states that are coupled (either optically or with microwaves, in our instantiation) to the excited state. In a case where only one lower and one excited state are involved that have equal

degeneracy, this reduces to $\Gamma/2$, where Γ is the natural linewidth of the transition. For the $X^2\Sigma$ state to $A^2\Pi_{1/2}$ state transition, Γ is equal to $2\pi\times5$ MHz. In YO, the excited state $A^2\Pi_{1/2}$, J'=1/2 (+) has a degeneracy of 4 (F'=0 or 1). The ground states which can be optically connected to the excited state are $X^2\Sigma$ v"=0, N"=0,1, or 2 and v"=1, N"=1, which have allowed values of $F$of 0,1|1,0,1,2|2,1,2,3|1,0,1,2, respectively, giving degeneracies of 4|12|20|12, using the same ordering of states. In all of our previous work[21, 20], all of these states were coupled to the excited state, indicating a maximum possible scattering rate of $\Gamma\times4/52$, or $\Gamma/13$. Later in this chapter are detailed a number of other possiblities for increasing the scattering rate.

2.3 Optical repumping of N"=2, v"=0

Endeavouring to realize a larger photon scattering rate in YO, we experimented with modifying the choice of repumping scheme described in the previous section. By using microwaves to remix only N"=0 and 1 levels in v"=0, and optically repumping the N"=2 level through the negative parity level in the $A^2\Pi_1$ state, J'=1/2 level which then decays to N"=0,2, we can increase the scattering rate on our main cycling transition. This is diagramatically shown in figure 2.2. Because of the change in the number of states connected to the same excited state, the scattering rate is increased by $\sim$60 percent with this choice of rempumping scheme, from $\Gamma/13$ to $\Gamma/8$. As will be discussed in more detail in Chapter 5, implementing this scheme dramatically increased our optical deceleration rate and the number of molecules slowed to trappable velocities.

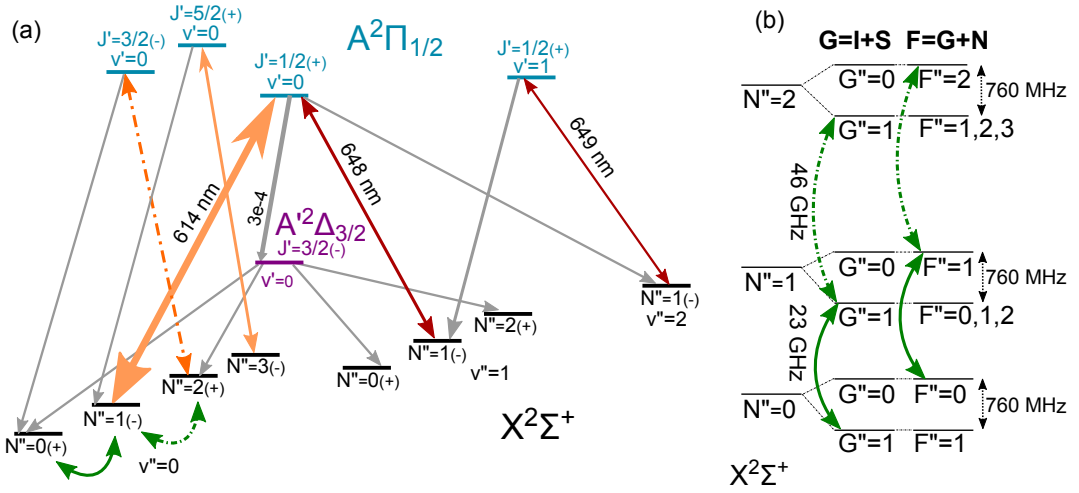

Figure 2.2: Choice of cycling transition for repumping N"=2 either optically or with microwaves at 46 GHz. Optical repumping uses the dashed-dotted orange arrow transition, while microwave mixing uses the dashed-dotted green arrrows transitions. We only apply one or the other, not both. We anticipate the largest unplugged leak at this point is into N"=0 and 2 of the v"=1 state via the $A'^2\Delta_{3/2}$ state.

2.4 N"=3

In case of unintended excitation to an unplanned excited state leading to leakage to excited rotational levels in the ground state, we implemented a laser pumping out the N"=3 population via the $A^2\Pi_{1/2}$ state, J'=5/2 level. This has no effect on the main cycling transition rate as it is connecting to a different excited state. Molecules can either decay back to N"=3, or they can decay to N"=1 where they can rejoin the normal cycling transition. This frequency is 9.775 GHz from the N" = 2 repump, and so is obtained by sending the N" = 2 light through an EOM. The effects of this repump laser on our MOT operation are detailed in Chapter 7.

2.5 Is a v"=3 repump necessary?

Based on the estimated Franck-Condon factors (vibrational overlap integrals) of 2×10^{-6} [34] between the $A^2\Pi_{1/2}$ v"=0 state and the $X^2\Sigma$ v"=3 state, we would not anticipate a significant amount of leakage to v"=3 or higher vibrational states within the number of photon scatters required

for slowing and trapping. While monitoring the MOT signal, we did apply a laser throughout the expected frequency range to see if a v"=3 to v'=2 repump would increase the number or the lifetime of our MOT, but we did not see an effect. This also suggests that we do not have a substantial initial population in v"=3. We further confirmed this hypothesis by failing to detect in-buffer-gas-cell absorption on that transition. While it is possible that we missed the correct location of the transition, our estimates suggest we know the frequency to within 100 MHz and we traced out ∼1 GHz in each case. We conclude that v"=3 is not affecting our experiment at this point in time, though we have the laser on hand if we ever wish to experiment with it again.

2.6 Microwave mixing

Just as with our optical cycling and our need to prevent polarization dark states when exciting on a $F" > F'$ transition, we need to consider a similar issue when using microwave mixing. With circularly polarized light, as in our MOT beams, it is straightforward to realize that σ^+ light cannot drive a $\Delta\ F = 0$ or -1 transition, and likewise that σ^- polarized light will not drive a $\Delta\ F = 0$ or +1 transition. So, one of the streched F" states will always be unaddressable. Likewise, with linearly polarized light, there can always be a superposition state that will be unaddressable to the light for $F" > F'$.

Similarly, when driving microwave transitions we have to be conscientious of the F number of states that we are driving to and from. In our best slowing scheme so far realized (using microwave mixing of N"=0 and 1 and optical addressing of N"=1 and 2) we note that we are relying on driving N"=0 to N"=1, where the F_{goal} is greater than the F_{start}. In our less optimal configuration (See Chapter 5 for further details), where we use microwaves to mix N"=0,1,2, and optically address only N"=1, we find we may have difficulty. For the N"=2 to 1 microwave pumping, we are reliant on pumping to a F_{goal} less than F_{start}, and so can be susceptible to issues arising from polarization dark states. This can be ameliorated by rapidly switching between microwave horns of orthogonal polarization or introducing a varying phase shift between horns of orthogonal polarization. While we have preliminarily tried rapid switching between two 46 GHz horns of orthogonal polarization

during the slowing sequence, we have not yet found an improvement. This may not be currently a limiting factor. However, when we work towards a narrow-line MOT for YO on the $X^2\Sigma$ state to $A'^2\Delta_{3/2}$ state transition, depending on the choice of microwave mixing scheme we will want to be diligent about carefully addressing all possible states. The details of our plans for the narrow-line transition are laid out in Chapter 8.

2.7 Decoupling the N"=1,v"=1 manifold

In the interest of increasing the photon scattering rate even higher, there are other laser schemes we can consider. By removing the laser exciting the N"=1, v"=1 manifold to the excited J'=3/2 (+) level, we could further increase the photon scattering rate, akin to the gain realized by the optical repumping of N"=2. This modified repumping scheme is depicted in Figure 2.3. The scheme would reduce the maximum realizable scattering rate even further, from $\Gamma/8$ with N"=2 optically repumped to $\Gamma/5$. The difference in frequency between the current transition to J'=1/2 and the one to J'=3/2 is only 27.916 GHz, within the tuning range of the laser. In order for this scheme to be effective, it is necessary to have the N"=3 to J'=5/2 repump that was discussed earlier in the chapter in use, so as to recycle molecules that end up in N"=3 after being repumped through the J'=3/2 level.

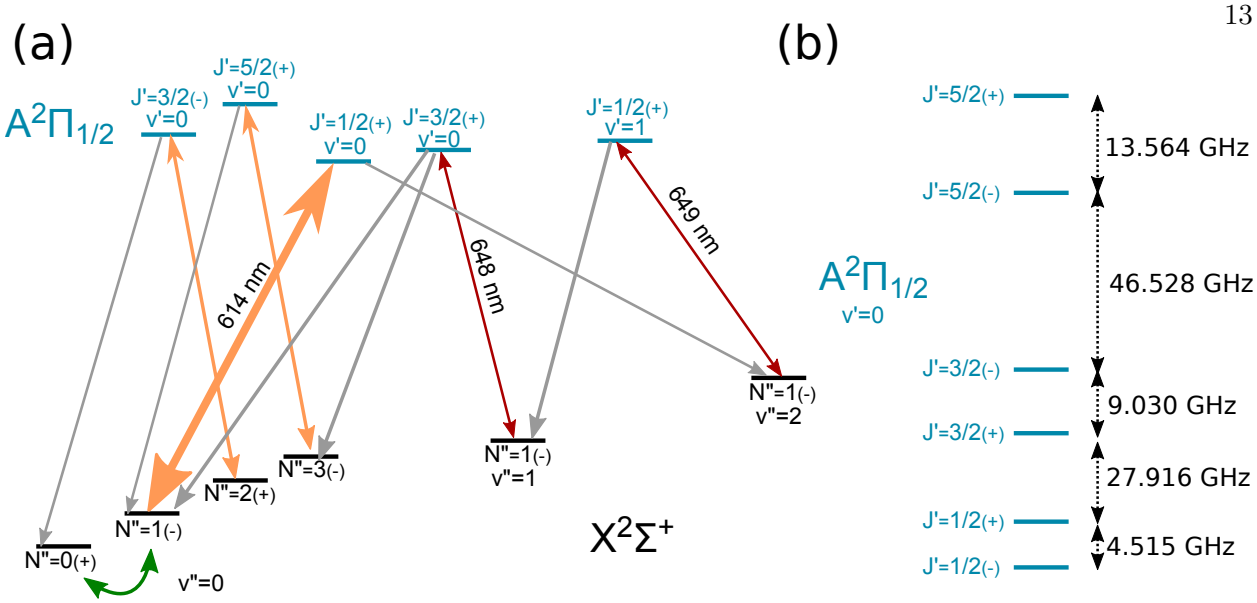

Figure 2.3: (a)Proposed repumping scheme which decouples v"=1 from the main cycling transition, allowing for a maximum photon scattering rate of $\Gamma/4$. (b) The relevant rotational and parity splittings in the $A^2\Pi_{1/2}$ state.

2.8 N"=0 optical repumping

Going even further along the path of increasing the photon scatter rate, another possibility we are considering in the near future is to remove the microwaves completely from the slowing and broad MOT implementation. In order to do this we would need to resolve the leak via the $A'^2\Delta_{3/2}$ state to the N"=0 and 2 levels in a different manner than we currently are. A possible way to achieve this, depicted in Figure 2.4, is to maintain the optical repump of N"=2 to the J'=3/2 level of the $A^2\Pi_{/2}$ state, which would then pump that population to the N"=0 level. The addition of a 690 nm laser (which will eventually be used for the narrow-line cooling) will bring the N"=0 population to the $A'^2\Delta_{3/2}$ state. Without further change, this wouldn't allow the molecules to rejoin the cycling transition. However, the parity splitting in the $A'^2\Delta_{3/2}$ state is relatively small (known to be less than the Doppler broadened linewidth inside the buffer gas cell, ~60 MHz [34]). So, an applied electric field on the order of tens of Volts per centimeter will be enough to mix the opposite parity states and allow decay from the $A'^2\Delta_{3/2}$ state to the N"=1 level and rejoin the main cycling

transition.

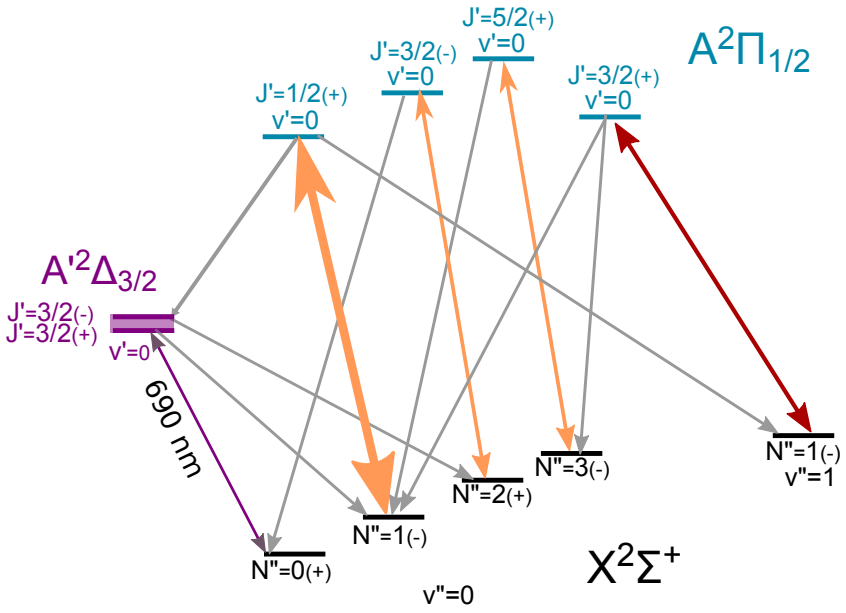

Figure 2.4: By applying an electric field to mix the parity levels in the $A'^2\Delta_{3/2}$ state and addressing the 690 nm $X^2\Sigma$ to $A'^2\Delta_{3/2}$ transition, we can pump molecules from the N"=0 level and allow them to rejoin the main cycling transition. This adaption would not require any microwave coupling of states to provide closure

It is possible that the small electric field would have other unforeseen consequences on the operation of the MOT. However, it will be straightforward to install electric field plates in the MOT region, though somewhat more difficult to install them along the entire slowing length. Another option would be to utilize microwave mixing during the slowing time, then switch off the microwaves and use the N"=0 to $A'^2\Delta_{3/2}$ state optical repumping only in the MOT region. If used without the decoupling of v"=1 discussed in the previous section, the decoupling of the N"=0 manifold will bring our maximum possible scattering rate from $\Gamma/8$ to $\Gamma/7$. If used in combination with the aforementioned decoupling, it will bring the maximum scattering rate from $\Gamma/5$ to $\Gamma/4$. As will be discussed more thoroughly in Chapter 5, since a 60 percent change in scatter rate yielded a 20 times gain in slowed molecule signal, these various cycling transition schema are exciting potential experimental directions for improving slowed and trapped molecule number.

Chapter 3

Experimental apparatus

3.1 Introduction

In this chapter I describe various components that are important parts of our experimental apparatus. An overhead diagramatic view of our vacuum chamber is shown in Figure 3.1. Molecules are produced in a single-stage cyrogenic buffer-gas cell, after which they are optically decelerated and loaded into our MOT in the octagonal chamber. I give an overview of our laser systems, our microwave system (which is used to maintain optical cycling of YO molecules), the imaging systems, the vacuum setup, the buffer gas cell, and the MOT. The cell is described in more detail in Chapter 4, and specifics of the MOT coil are given in Chapter 6.

The vacuum system is pumped out by three 300 L/s turbomolecular pumps, one on the cross directly outside the cell, one at the six inch cube along the slowing region, and one above the MOT. The MOT region turbo is an Agilent TwisTorr 304, which has a high compression ratio even for light gasses such as helium. In comparison with the non-high compression-ratio turbo we had on the chamber previously, our MOT region vacuum pressure went down by a factor of three when the He buffer gas is on. The other turbos are Varian V300s, which are not optimized for lighter gasses, though replacing them is a potential improvement that could be implemented in the future. We have two ion gauges on the system, one located at cell region and one near the slowing laser beam entrance window. With no buffer gas helium flow, our MOT region reaches a pressure of 9×10^{-10} Torr, while the cryostat region reaches 2×10^{-8} Torr.

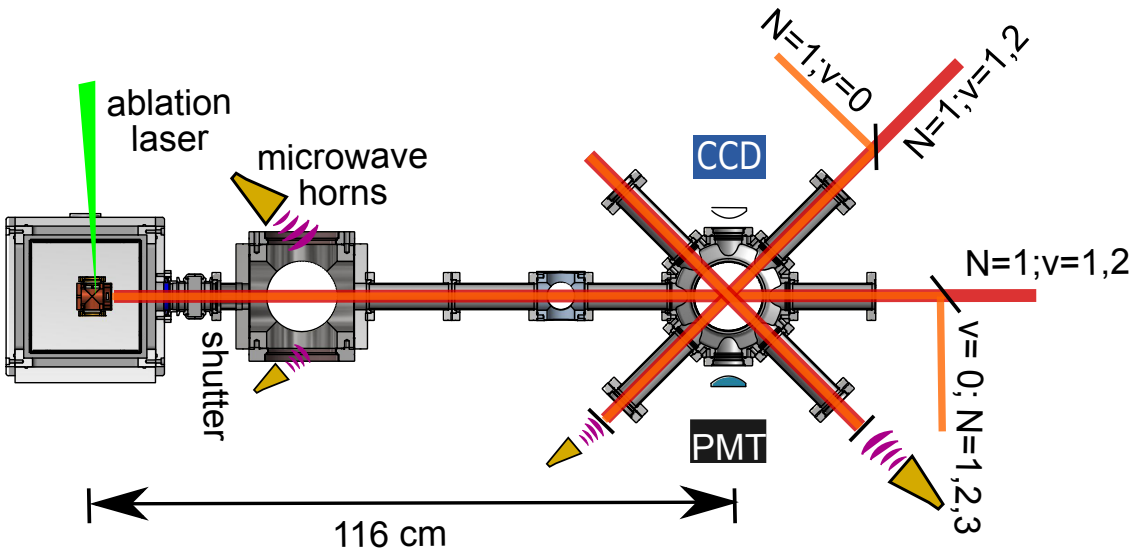

Figure 3.1: Schematic of the experimental apparatus. Molecules are produced at left via ablation of a precursor target inside the buffer gas cell. They propagate to the right while interacting with a counterpropagating slowing beam, until they reach the trapping region. The trapping region contains the coils, three sets of counterpropagating MOT beams, and can be imaged from either side by the CCD or PMT.

3.2 Laser systems

In order to address the various necessary optical transitions in the YO molecule, we have a number of laser systems. Additionally, because we frequency chirp the light for slowing and keep fixed frequency beams for the MOT, we find that having two separate 614 nm systems addressing the main cooling transition to be helpful. Currently, all of our frequency stabilization is done by locking our lasers to a home-built erbium octave-spanning frequency comb, though in the future we will need to stabilize a 690 nm diode for addressing the $X^2\Sigma$ to $A'^2\Delta_{3/2}$ narrow-line transition. Because this transition is only 13 GHz away from the 689 nm transition used by the Strontium clock experiment in our group, we will be able to use an EOM offset lock to their laser. The details of our laser frequency locking schema are described in more detail in Appendix B.

We have three systems we use for producing 614 nm light in our experiment. A Sirah Mattise dye laser produces around 400 mW of $N"=2$ optical repumper utilized for slowing. We use Rhodamine 610 dye mixed into ethylene glycol as the gain medium for the laser (at a concentration of 0.57 grams per liter). A 1228 nm seed is Raman amplified and doubled using an MPB Communications system with a home built ECDL (external cavity diode laser) as the seed to produce the slowing main cooling transition light. The doubled output can be up to 1 Watt with 25 mW fiber coupled seed power. The seed laser diode is from Innolume, part number GC-1230-TO-200. A Toptica SHG system produces $N"=1$ light for the MOT beams, yielding approximately 750 mW. After frequency manipulation and combination of beams, this yields about 100 mW of $v"=0$ light for slowing and for the MOT, and about 40 mW of $N"=2$ in the slowing beam.

We generate repump light at 648 and 649 nm with home-built ECDLs in the Littrow configuration. Since these master lasers only produce around 20 mW, we use the master lasers for $v"=1$ and 2 to each injection lock two slave diodes, one each for the $G"=0$ and 1 components. These slave diodes are not AR-coated (Thorlabs part number HL6385DG), so the cavity is the diode itself. The temperature and current have to be set appropriately for the slaves to follow the mode of the seed. To produce the $\sim$770 MHz offset between the $G"=0$ and $G"=1$ manifold, we use a single pass

AOM. Because the $G"=1$ manifold covers a range of about 15 MHz, we apply a modulation to the frequency of the AOM. The frequency modulation has a span of 15 MHz and a rate of 1 kHz in order to address the entire level manifold. In order to monitor the injection locks, we use both an optical spectrum analyzer (OSA) and a 10 MHz resolution wavemeter. In order to maintain injection lock with the hyperfine scanning, we feed-forward the current on the second slaves to facilitate their ability to stay injection locked. The output power of each slave laser is on the order of 120 mW. After combination of the $G"=0$ and 1 beams, the power is split for use in slowing or the MOT and AOMs are used to correctly place the frequencies. The light is then coupled into polarization maintaining fibers and coupled over to the experimental table. Typically at this point the power levels at the output of the fibers is 15 mW, which are then each coupled into a tapered amplifier (TA) (either Eagleyard EYP-TP-0650-00259-2007-CM502 or Sacher TPA-0650-0250). The outputs of the TAs are fiber coupled once again to maintain ease of alignment, and are combined with other slowing or MOT components. The beams then pass through the Pockel's cells which switch the incident light between orthogonal linear polarizations(Conoptics 350-160-01) at a rate of $\sim$5 MHz. In order to prevent competition between the different hyperfine frequencies seeded into the same TA, which potentially causes fluctuations of the power splitting between the modes, we are planning to modify our systems to have only a single hyperfine component per TA.

In order to have our optical frequency comb be a useful ruler to lock our laser frequencies to, we require a stable microwave source. The lab shares a Wenzl oscillator, which is locked to a 10 MHz signal that is stabilized by a cesium reference in the building. By stabilizing both the repetition rate (approximately 100 MHz) and the carrier offset frequency to these known RF frequencies, the optical frequency of all comb teeth are stabilized. In order to lock the carrier offset frequency, we need to obtain a heterodyne beat between doubled light from the 2100 nm end of the comb with frequency $2f_{co} + 2n_0 f_{rep}$ and locking it to the undoubled 1050 nm end with frequency $f_{co} + n_1 f_{rep}$. Thus, in order to self reference the comb, we require sufficient power in both ends of the broadened comb spectrum. In order to lock our other lasers to the comb, we also require power at 1228, 1296, and 1298 nm. We double the $\sim$1297 nm section of the spectrum with a periodically poled lithium

niobate crystal that has 1.5 nm of bandwidth in order to lock the 648 and 649 nm repumps. The undoubled 1228 nm comb light is used to directly lock the Raman seed laser. We use a optical bandpass filter to isolate the comb light around 1228 nm to produce a beatnote with the Raman seed. In order to allow amplification of all of the RF beatnotes, we use a 10 MHz bandpass filter around the offset lock frequency, and then use frequency-to-voltage converters to establish a voltage error signal. This error signal is the input to our loop filters, which servo the laser currents to stabilize the laser frequency. In this way, we frequency lock all the lasers needed for slowing and orange MOT operation. More extensive information on the comb and its spectrum, as well as laser locking, has been previously detailed in Mark Yeo's thesis [51].

3.3 Microwaves

As described more fully in Chapter 2, in order to maintain optical cycling, we need to recover molecules that end up in the $N"$=0 or 2 levels after decaying through the $A'^2\Delta_{3/2}$ state. We accomplish this by coupling microwaves at 23 GHz (resonant with the $N"$=0↔1 transition) or at 46 GHz (resonant with the $N"$=1↔2 transition) into the chamber. We couple the microwaves in to the chamber at several locations: into the 6 inch cube along the slowing region, and into the MOT region behind the MOT retroreflect mirrors or behind the slowing input mirror to get microwaves in the MOT region for trapping. In order to prevent attenuation of the microwaves, we use large dielectric coated mirrors and Delrin plastic holders for waveplates so as to avoid reflections from any small metallic constraints (other than limitations of the chamber itself). The microwave horns themselves are all 20 dBi gain waveguide coupled horns, where the i refers to isotropic, indicating the gain along the primary axis compared to a fully isotropic antenna radiation pattern. The part number for the 23 GHz horns is Sage Millimeter SAR-2013-42-S2, while the 46 GHz horns are SAR-2013-22-S2.

The majority of the slowing region is composed of 2-3/4" Conflat parts with an inner diameter of 1.5 inches (about 3.8 cm) and our microwave wavelengths are 1.3 cm and 0.65 cm for 23 GHz and 46 GHz. Because these lengths are on a similar scale, we have to consider whether our microwaves

can be coupled sufficiently well to the chamber or if they will likely have dead zones at the MOT location or along the slowing region. In order to achieve a Rabi frequency of about 1 MHz for our 4.5 Debye rotational transition dipole moment molecules, we require an electric field strength of approximately 60 Volts/meter, or 1 mW/cm^2 intensity of our microwaves. Using COMSOL, our setup of microwave horns, 2-3/4" nipple, and open MOT region can be simulated (though the entire MOT region chamber is not used). Doing so for the MOT region for 23 and 46 GHz yields the results seen in Figure 3.2. From this simulation, we find that for both 23 and 46 GHz microwaves, but particularly for 23 GHz there is a "dead" zone at the MOT region due to spreading of the wavefronts after the 2-3/4" conflat nipple. This simulation led us to install 2 Watt microwave amplifiers for the MOT region, rather than using the 50 mW output we previously had.

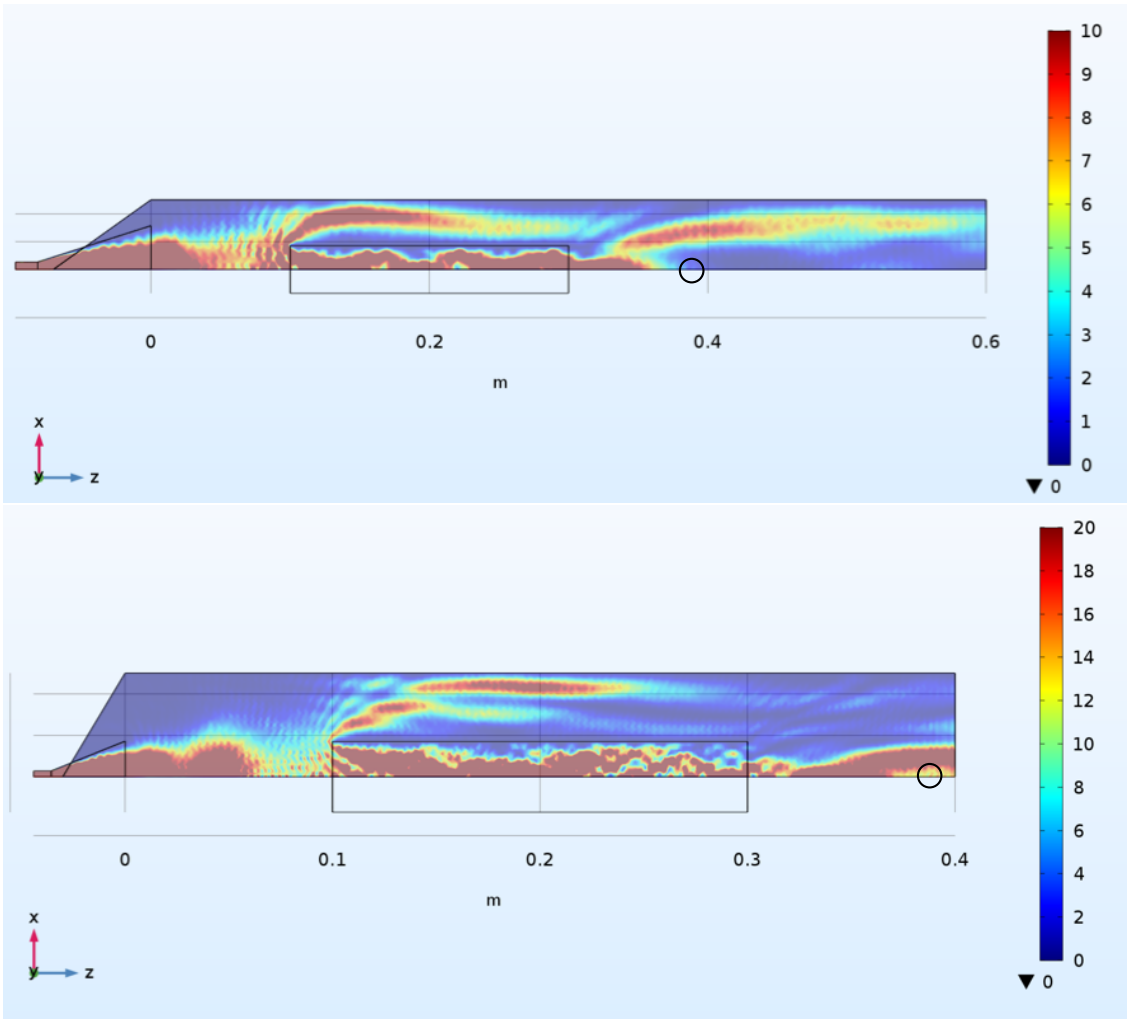

Figure 3.2: Simulation of microwave intensity for 50 mW input power at horns in MOT region (circular region .38 meters along axis) for 23 GHz (upper) and 46 GHz (lower) microwaves. Color scale has units of mW/cm^2. Black rectangles indicate the volume witin the hollow conductive cylinder of the Conflat nipples of the chamber.

As mentioned in Chapter 2, there is a potential for polarization dark states to form when relying on larger $N"_{\text{start}}$ to smaller $N"_{\text{goal}}$ microwave repumping. We have the ability to rapidly switch between two horns in the MOT region for 46 GHz, which can be aligned to different polarizations to break up polarization dark states. While we have not yet determined if this capability is necessary, it could resolve an issue when doing narrow line cooling as described in Chapter 8, due to the different planned microwave mixing scheme.

The circuit schematic for our microwave system is laid out in Figure 3.3. In order to switch between microwave remixing of v"=0 rotational states or v"=1 rotational states, we utilize an Analog Devices 9959 evaluation board to produce the appropriate sideband frequency, which is then mixed with the 12 GHz unmodulated signal. In order to only have the appropriate (first lower) sideband address the experiment, we utilize a bandpass filter spanning from 11.375 to 11.725 GHz (Miteq FLT-105449). The signal is amplified with an Avatek AWT-18057 42 dB gain amplifier, and then doubled to 23 GHz with a Marki Microwave D95190 doubler. All of the remaining amplifiers at 23 GHz are New Millenium AMT-05-25-23 with 13 dB gain, with the exception of a 2 Watt output amplifier directly before the MOT region horn (Fairview microwave SPA-265-33-01-K). The four-way power dividers are Krytar 7020265 matched-line directional dividers, which have only 2.3 dB total insertion loss and good power matching between the different outputs. In order to mix the v"=1 N"=1,2 manifolds at 46 GHz, as the v"=0, N"=2 repumping is done optically, we use two synchronized switches to simultaneously switch between v"=1 and v"=0 sideband frequencies from the DDS while directing what will be the 46 GHz signal to a terminator or to the horns. We usually perform this switching at 1 MHz. Because the isolation of these switches is only 20 dB, we have a second higher isolation (40 dB), but slower, switch to ensure that no 46 GHz resonant with the v"=0, N"=1$\leftrightarrow$2 transition is entering the chamber. For example, we will regularly have no 46 GHz radiation during the slowing but then turn it on during the MOT to remix v"=1 N"=2 population that may have accumulated as decay from the $A'^2\Delta_{3/2}$ state. The last stage is doubling to 46 GHz with a set of Marki Microwave ADA-2050 CMV active doublers, before coupling to the chamber. In order to prevent polarization dark states, we have the capability of switching at 100 kHz between a low-power and high-power MOT region horn which are aligned to the chamber with orthogonal polarizations.

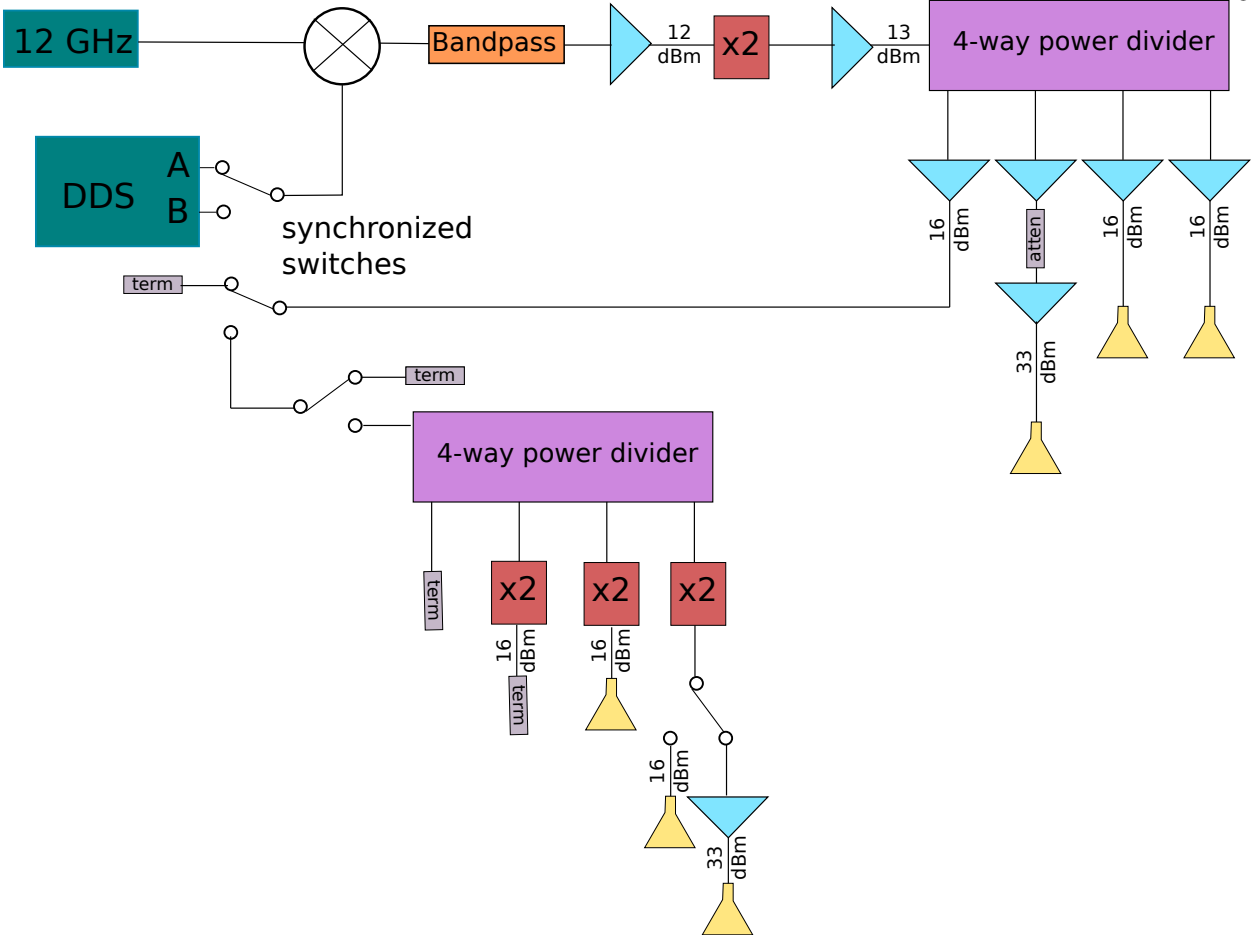

Figure 3.3: Electronics schematic for microwave system. This setup allows mixing of v"=0 and 1, N"=0,1,2 in a variety of arrangements.

3.4 In-vacuum shutter

In order to reduce the effect of collisions from helium on the YO molecules during slowing and MOT operation and to lower the MOT region vacuum pressure despite having a continuuous flow of helium buffer gas, we have a shutter installed in the vacuum chamber along the slowing region. It is installed 28 cm downstream of the buffer gas cell directly after the 2-3/4" Conflat cross on which the cell region turbo is mounted. It is located before the gate valve so the shutter can be modified or replaced without breaking the MOT region side of the vacuum chamber. Unfortunately, after a couple months of use, the in-vacuum shutter starts to stick and will not open or close fully, and so

needs replacement. The shutter is installed upstream of our gate valve so that we do not have to rebake the MOT region of the chamber every time the shutter is replaced.

The shutter itself is a Vincent Associates Uniblitz shutter. This company offers a vacuum compatible version of their shutters where the drive coil is potted in epoxy. The shutter is mounted within two Conflat 2-3/4" to 6" adapters. The wires for the shutter drive and a thermistor connection go through a feedthrough mounted on the preceding 2-3/4" cross. In order to prevent overheating of the shutter, the drive coil is heat sunk to the mount with copper blocks. This allows running of the shutter full-time while reaching only 40 degrees Celsius. Without this heatsinking, the experiment would have to be run at a lower repetition rate in order to prevent overheating of the shutter.

As will be referred to in greater detail in Chapter 5, we find that the reduction in helium pressure also helps reduce loss of slowed molecules due to background helium collisions.

3.5 Buffer gas cell overview

Further detail of the buffer gas cell we use to produce YO is given in Chapter 4, though here I give a cursory overview. As shown in Figure 3.4, the cell consists of a copper block anchored to the "4 K" level of a two-stage pulse tube cryocooler (Cryomech PT410). The "40 K" stage of the pulse tube has radiation shielding anchored to it in order to reduce the heat load on the "4 K" stage. In actuality, these stages reach temperatures of approximately 3.5 Kelvin and 30 Kelvin after cooldown. The system takes approximately four hours to cool down from room temperature to its lowest level, with the chamber already pumped out. The radiation shields at 3.5 Kelvin are covered with coconut charcoal that is epoxied to the copper with Stycast 2850FT, an epoxy that is thermally expansion matched to copper from cryogenic to room temperatures. This charcoal allows for effective cryopumping of the helium buffer gas, which would otherwise build up and adversely affect the vacuum and cold molecule production. The buffer gas cell has a window on one side through which the ablation laser enters. The helium inlet is made of 1/8" copper tubing, and enters the back of the buffer gas cell, where the helium then passes through a diffuser plate. There is

a helium "bobbin" to precool helium before entering the cell so that it does not enter the cell at room temperatuere. We find that leaks in the gas manifold manifest as ice plugs in the helium inlet line, which cause pressure buildup after the mass flow controller (Alicat MG-20sccm-D15M, 5IN,Gas:He) and cessation of molecule production. Since Swagelok only has so many reconnect cycles while remaining vacuum tight, it is important to carefully check for leaks after changes to the gas manifold. We typically use helium flow rates in the range of 0.5-5 sccm (standard cubic centimeters per minute). When the helium reaches the cell, it thermalizes to 3.5 Kelvin. Ablated molecules from the Y_2O_3 target then thermalize translationally, vibrationally, and rotationally with the cold helium before exiting the cell as a molecular beam.

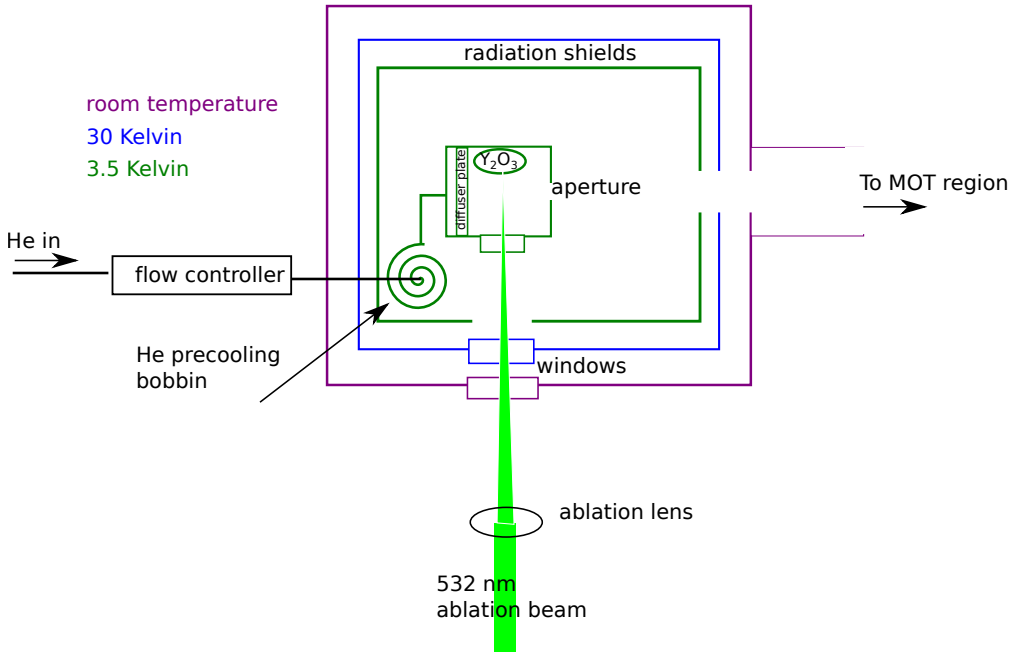

Figure 3.4: A schematic of our cryostat as viewed from above. Different colors indicate temperature of the constituent parts: all external vacuum/room boundaries are at room temperature (purple), while a set of radiation shields are held at 30 Kelvin (blue) and the cell itself along with the charcoal cryosorb are anchored to the 4 Kelvin stage(green). Helium is precooled to 4 K before entering the cell by going through a length off copper tubing soldered to a heat sink that is anchored to the 4 K stage. YO is produced via ablation of a Y_2O_3 ceramic target with a 532 nm 8 mJ pulse. Rastering the ablation beam allows efficient use of the whole surface area of the target.

We found that a completely sealed 40 K shield (except for the molecule beam exit aperture) did not allow helium gas to be efficiently pumped out from between the shields. By punching holes in the 40 K shield to increase the pumping efficiency, we improved molecule production by about 50 percent, despite an increased temperature of the cell due to less effective radiation shielding. These two extra holes (1" diameter each) dramatically improved pump out speed at room temperature as well, reducing our down time due to ablation target changes, etc. In the future, modifying the radiation shield (perhaps by doing a chevron design) will improve conductance without increasing blackbody radiation impinging on 4 K stage and allow a lower cell temperature.

Since it is not clear if we have the maximum possible production of YO molecules, time spent improving the local gas pressure directly outside of the cell may be worthwhile.

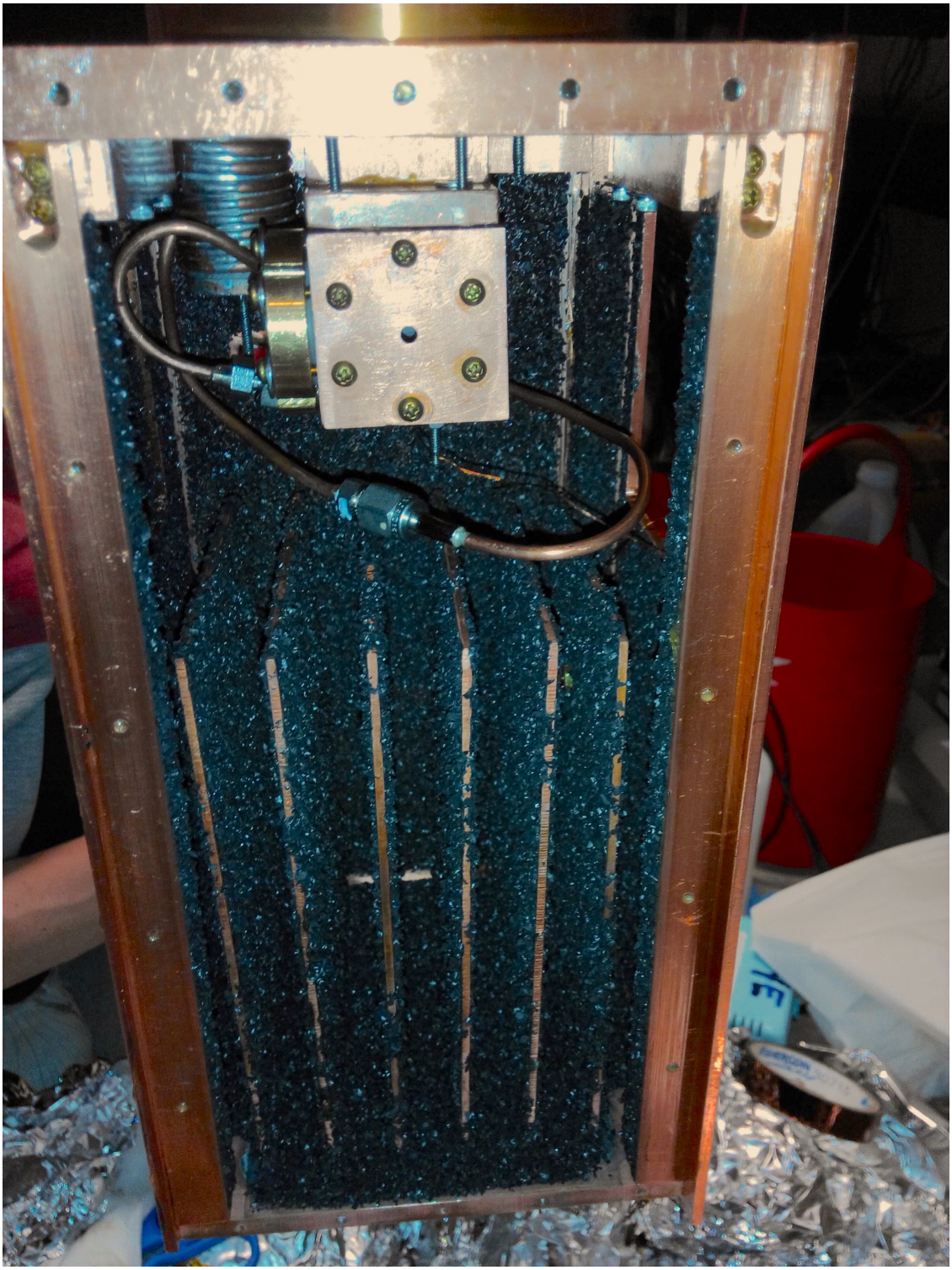

Figure 3.5: Image of cryostat chamber and cell from the front with the front copper radiation shields removed. The helium precooling bobbin is visible in the upper left. On the left side of the cell the brass ablation window mount is visible.

We can measure the dependence of molecule production on temperature, as shown in Figure 3.6, by turning on and off the pulse tube while still acquiring data. The temperature of the cell is read out from a Lakeshore temperature diode installed directly underneath the cell. Molecule production increases strongly with lower temperature, with the effect being more steep with respect to temperature for 2.5 sccm as opposed to 5 sccm. At some point in the future, it could be interesting to try further cooling the cell with a 1 K pot as in Reference [52] in order to see how the trend continues. However, since we are using microwaves to mix N"=0 and 1, if the only change is shifting the produced rotational distribution lower, we will not see a further improvement in molecule number. On the other hand, if the molecule number increase is due to improved thermalization of the YO molecules with the helium buffer gas, we may see an improvement at even lower temperatures.

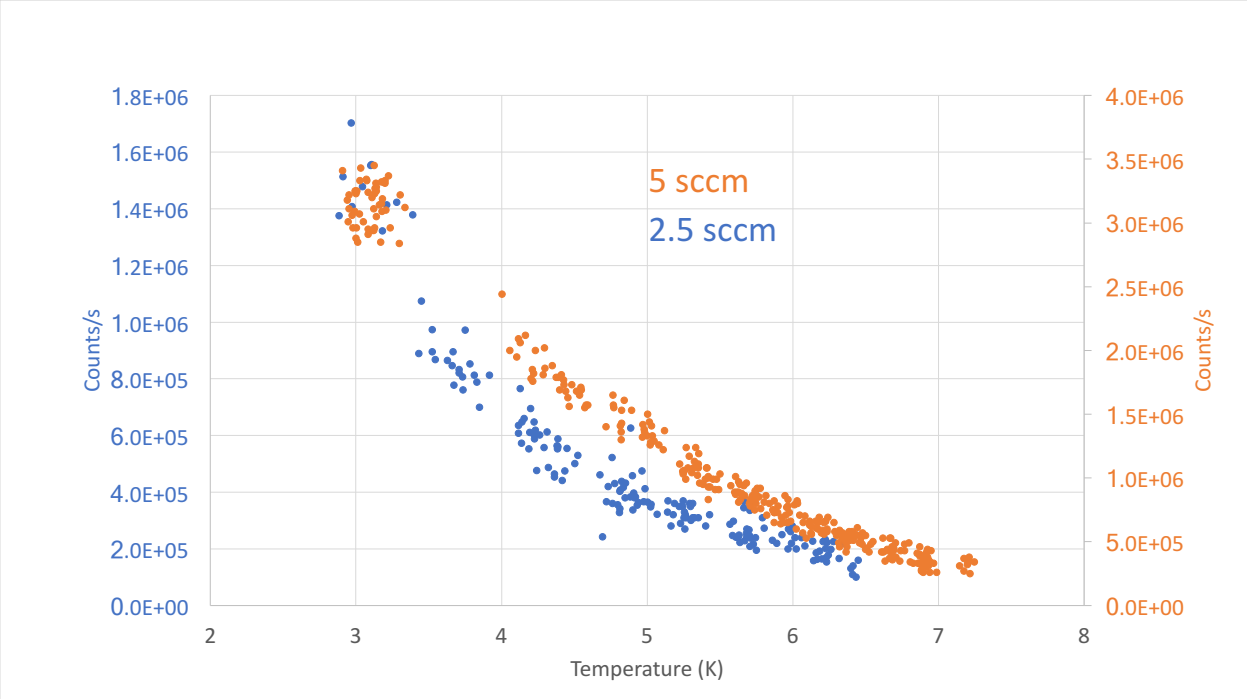

Figure 3.6: Peak YO molecule production for different temperatures and flow rates . Temperature variation was induced by shutting off the pulse tube while still producing molecules.

We find that the ablation window of the cell becomes blackened with extended use. This

effect is due to deposition of various ablation products on the window followed by localized heating as the ablation laser passes through the window. A used window showing this effect is pictured in Figure 3.7. Our replacement schedule of the window is dependent on buffer gas flow rate, but needs to be quite frequent (about once a week) when running at less than or equal to 1 sccm . The procedure to replace the ablation side window and Y_2O_3 targets is described in Appendix E

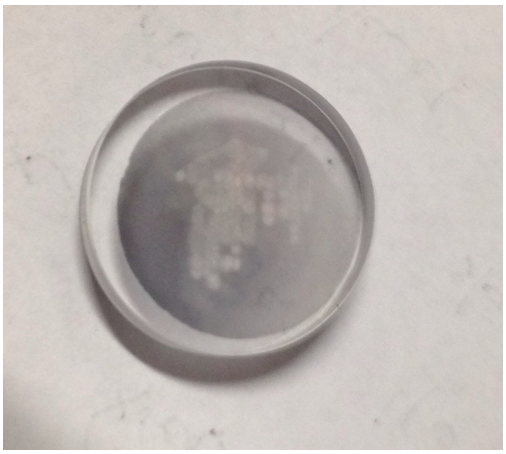

Figure 3.7: Image of ablation window after having been in use for ∼2 weeks for helium flow rates around 1 sccm. The most transparent locations suffer ∼25 percent attenuation, with darker areas being even higher. This results in a reduction of YO molecules produced over time.

We have tried using a "snorkel" to move the ablation beam window further from the ablation plume. This seemed to reduce the rate of blackening of the window, but also reduces our ability to raster the YAG laser to ablate different parts of the Y_2O_3 targets.

3.6 Detection systems

In order to detect the laser induced fluorescence of the YO molecules in the trap region, we have two separate imaging systems. For spatially resolved detection of our molecules, we use the data from a charge coupled device (CCD) camera offloaded directly to a desktop computer. Our CCD is an Apogee Alta U47, which has a quantum efficiency of 93% at our detection wavelength of 614 nm. The camera has a 1024×1024 pixel array, each of which has a 13×13 μm area. While the

CCD can offload all pixels individually, it can also bin pixels on chip before offloading. We typically use this capability to bin 6×6 pixels on chip in order to improve readout times.

For time resolved light detection, we use a red-enhanced photomultiplier tube (PMT) (Hamamatsu R10699). The PMT current spikes go through a transimpedance amplifier and are counted with a SRS430 multichannel scaler (MCS). We find that saturation of current spikes in the time domain occurs at 1.7×10^7 counts per second (limited by the transimpedance amplifier). At this photon count rate there is a high probability of succesive pulses overlapping each other, and so being under-counted by the MCS. To avoid the saturation regime of the PMT/MCS system we use careful alignment of the MOT and slowing laser beams and copper blackening in the chamber, but could potentially switch to current accumulation mode if the light scatter were too high. However, in order to reduce photon shot noise it is in our interest to keep the light background as low as possible. The characterization of the PMT transimpedance amplifier is discussed further in Appendix C.

In our system, both the PMT and CCD imaging systems are similar, and located on opposite sides of the MOT chamber orthogonal to the molecular beam. The lens setup is depicted in Figure 3.8. The color filter (Edmund Optics 84-118) is a fluorescence filter centered at 607 nm with 32 nm bandwidth.

While our vacuum chamber is open to air, we align our MOT coils with respect to our chamber by placing a threaded rod in the center of the MOT coils, with a notch at the center between the two boards. By shining our horizontal MOT beams while centered through the chamber windows, we can confirm that they are well aligned to the threaded rod and thus the MOT coils.

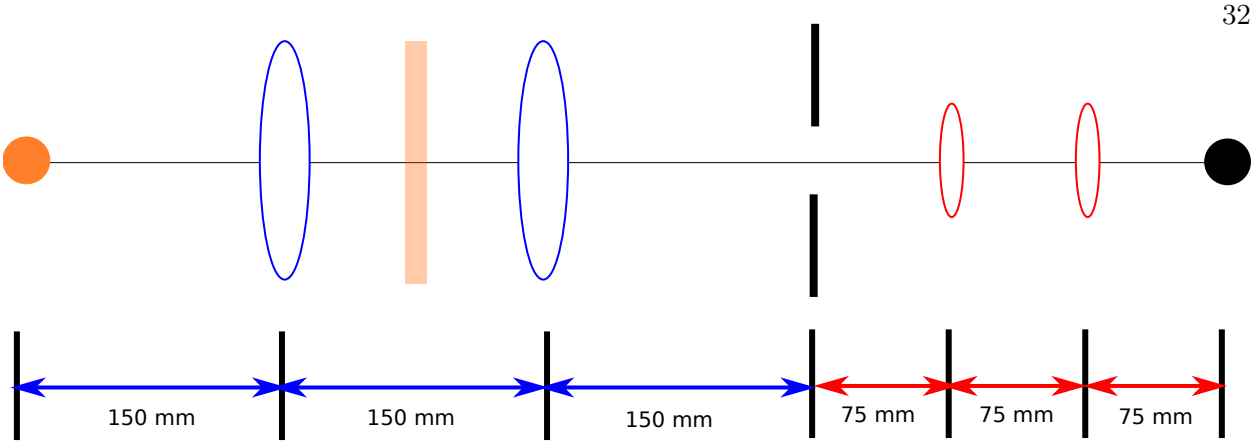

Figure 3.8: PMT and CCD Imaging systems. Blue lenses are 2 inch diameter 150 mm focal length lenses, while red are 1 inch diameter 75 mm lenses. The orange box indicates a color filter used to remove all ∼650 nm scattered light from our vibrational repump lasers. There is an image plane between the lens sets where the iris is placed for spatial filtering. All lenses are installed outside the vacuum chamber. The achromatic lens part numbers are Newport PAC086AR.14 for the two inch lenses and PAC046AR.14 for the 1 inch lenses.

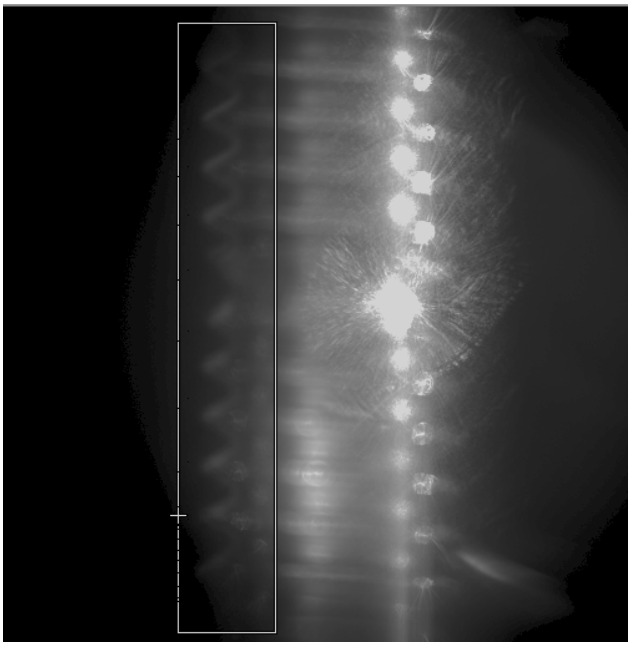

Figure 3.9: CCD alignment confirmation: by placing a notched threaded rod in the MOT region and imaging it with the CCD, we can confirm the CCD is imaging the desired region

We utilize this illuminated threaded rod to confirm our imaging system alignments as well. Additionally, by imaging the 8-32 rod with the CCD, we can determine where the MOT region is

on the CCD and determine the absolute magnification. Figure 3.9 shows the resulting CCD image, confirming that the CCD is properly aligned to the MOT region. By averaging horizontally across the white box region in Figure 3.9, we calibrate the thread distance to pixel size, as shown in Figure 3.10. Since the threaded rod is 32 threads per inch, we determine that our imaging is 102.6 pixels per mm, corresponding to a total image area of 1 cm by 1 cm, and a system magnification of 1.3.

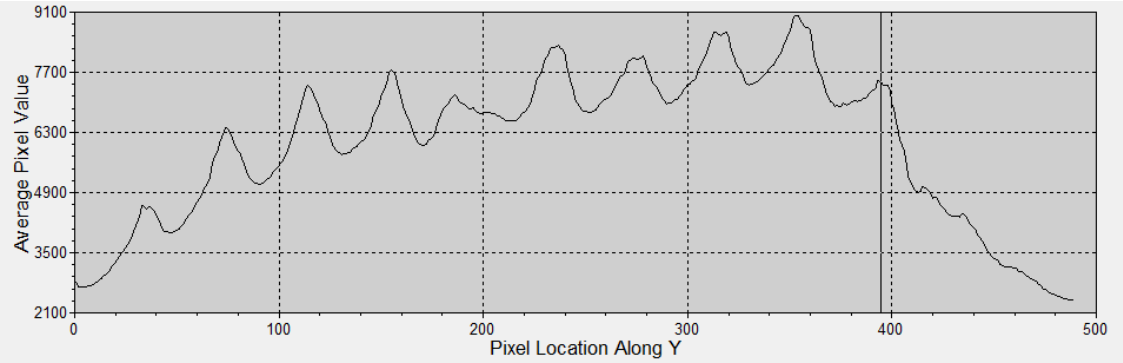

Figure 3.10: CCD magnification calibration: the cross sectional average counts vs pixel value along the edge of the 8-32 screw indicates the magnification of our imaging system. This label refers to 2 $\times$2 binned pixels.

As a final calibration check to confirm the positioning of our MOT beams, we can also utilize the MOT beams and the CCD to image the unslowed molecular packet. The results of this test are depicted in Figure 3.11. For this measurement, the desired beam was left on the whole time, and the CCD was exposed from 5 to 15 ms after ablation fire, thus containing the majority of the molecular packet. In panel (a) the transverse beam was used and so the laser detuning was set to 0 m/s. Panels (b) and (c) use the MOT beams that are at 45 degrees with respect to the molecules, and so the laser beam detuning was set to be resonant with 110 m/s molecules. In these images, the molecules are traveling from right to left, and gravity points downward. As a note, these images are not from the most recent alignment, and so should not necessarily line up with the screw imaged in Figure 3.9.

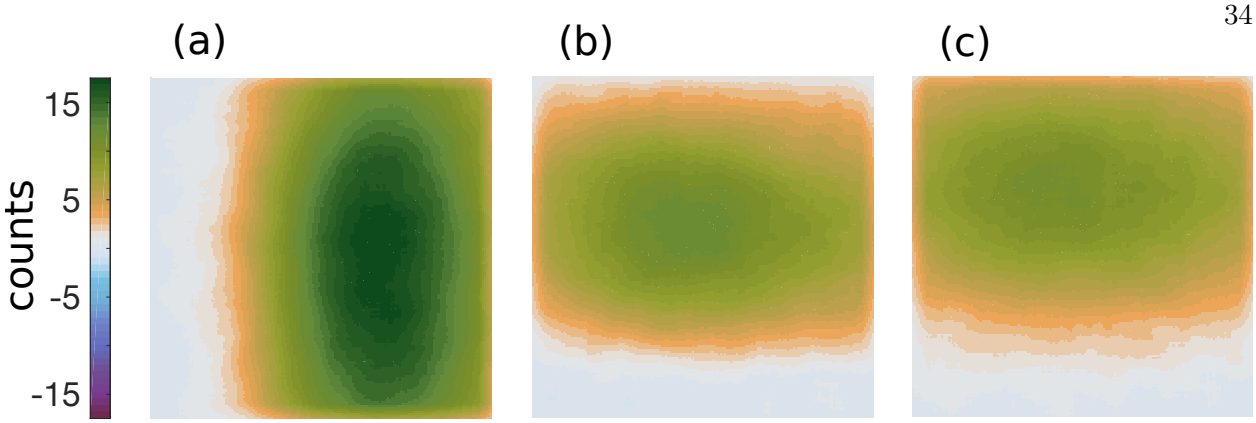

Figure 3.11: Imaging the unslowed molecule packet from 5-15 ms after ablation fire. Color axis indicates average CCD counts per 6×6 binned pixel, with 1 mm×1 mm square smoothing filter. (a) The vertical (transverse) MOT beam. (b)The NE/SW beam. (c)The NW/SE beam.

3.7 Light scatter reduction

Because we want to minimize the amount of light scatter at 614 nm detected by both our CCD and our PMT, we take steps to reduce light scatter in the chamber. In order to make vacuum compatible light baffles, we use the copper oxide blackening method described in Reference [53], which gives copper sheet metal a matte black finish. We have blackened cylinders in all the MOT beam vacuum nipples (which are themselves used to move the windows further away from the MOT region to prevent excess scatter), as well as modified 6 inch copper gaskets for the top and bottom of the 6-inch main octagonal chamber. We also have a blackened copper octagon to prevent scatter within the MOT chamber itself. As shown in Chapter 6, we also use the copper oxide blackening on the MOT coil traces to further reduce light scatter.

The MOT windows are anti-reflection (AR) coated to prevent scattering of our main cooling transition (614 nm) light. Because the 648 and 649 nm scattered light is blocked out by the band-pass color filter in the detection system, we do not have to worry about the scatter due to the repump beams. Light is coupled in and out of the chamber using homemade window vacuum ports, constructed by epoxying (Epotek 353ND) N-BK7 AR coated windows to KF to CF adapters.. We experimented also with fused silica windows, which have better birefringence properties, but they

ended up introducing a lot of light scatter. We determined the cause was that after a bake the AR coating shifted so that the amount of reflection at 614 nm was quite significant. Because N-BK7 is more closely expansion matched to the stainless steel of the vacuum chamber, it also means that the windows are less prone to cracking under the thermal cycling of bakes.

As a final step to reduce scatter, we also use irises for all of our MOT beams (typically set to about 13 mm diameter) on both the input and the retroreflected beam paths.

3.8 Coils and beams

In order to preserve as much laser power as possible, we rely on a combination of long-pass dichroics (Thorlabs DMLP638) which transmit repump light and reflect v"=0 light, and polarizing beam combiners for both the slowing and the MOT beams, as depicted in Figure 3.12. This necessitates that in the MOT region, our G"=0 and G"=1 components of v"=0 have opposite polarizations. For MOT operation, this is not an issue, as all the MOT force comes from the G"=1 manifold, with G"=0 acting as a repump.

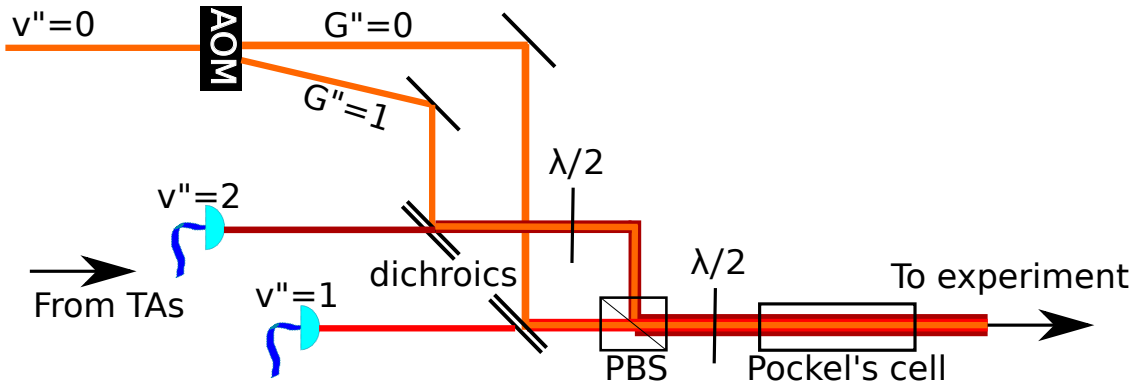

Figure 3.12: Scheme for combining v"=0,1, and 2 components for both MOT and slowing beams.

Looking forward, we can use a similar method for introducing 690 nm light to our chamber for narrow-line cooling, by using another dichroic mirror which passes 690 nm and reflects 648 or 649 nm light. With this dichroic mirror, the 690 nm light can be combined with a vibrational repump, and then combined with the other components in the same way.

After combination of all components and passing through the Pockel's cell, light for the MOT then goes through quarter and half wave plates in order to circularly polarize the light before going into the chamber. In correspondence with the magnetic field gradient being of the opposite sign for the axial compared to the radial direction, the vertical laser beams have orthogonal (opposite handedness) polarization to the two horizontal beams. The MOT beams are aligned to the center of the vacuum chamber. The slowing beam is gently focused with a 100 cm focal length lens in order to have better spatial overlap with the molecular beam exiting the buffer gas cell. Focusing of the slowing beam also made the slowing beam alignment more robust in our experiment. Since we need $N"=2$ repumping for both slowing and the MOT, $N"=2$ is always repumped through the slowing beam, so as not to need yet another 614 nm laser system.

Our magnetic field gradients for MOT operation are produced with an in-vacuum set of AC anti-Helmholtz MOT coils, which are resonant at 4.75 MHz, and are capable of producing a 20 G/cm field gradient with 50 Watts drive. Further description of the MOT coil design and construction is in Chapter 6. In addition to the main MOT coils, we also have external (DC) magnetic field cancellation coils positioned outside of the vacuum chamber. The currents of these Helmholtz coils are set to zero out the earth's magnetic field and residual magnetization of the chamber. However, we have not yet found the external field cancellation coils to improve the MOT operation.

Chapter 4

(Mis)Adventures in buffer gas cell design and ablation chemistry

4.1 Introduction

As ever in experimental physics, we would love to have a higher number and density of our species of interest. Molecular sources produce lower yields than the ovens that are found in alkali atom experiments [54, 9], which in combination with the lower photon scattering rates available makes the goal of trapping a large number of molecules more difficult. So, we asked ourselves why not produce more molecules? Those working with fluorides, such as CaF, have found an improvement in molecule yield by ablating a metallic target in the presence of SF_6 [55, 31]. Researchers at the Imperial College, London have a specially designed cell that helped improve molecule production and reduced the width of the molecular packet in the time domain [56]. Some understanding and guiding principles to the mechanisms of buffer gas cells are understood [9], but the parameter space is large and far from fully characterized, especially with regards to production of varying kinds of molecules and in-cell chemical reactions. So, we spent some effort attempting to improve upon our initial molecular distribution and yield from our buffer gas cell implementation. Overall, we found that adding various oxidizers to our buffer gas cell did not improve the production of YO, and neither did using a metallic Yttrium precursor (with or without oxidizers). We did, however, learn a helpful trick in our system regarding the powdering of our cell with a Y_2O_3 nanopowder, which resulted in a significant gain in the number of YO molecules. We also performed some characterizations on how different aspects of the cell geometry affected molecule production.

4.2 Magic dust

Perhaps due to collisions with helium after the YO exits the cell, we have regularly found improved slowing with lower buffer gas flow rates, in spite of larger molecule yields at similar velocities for higher helium flow rates. So, we endeavoured to produce more molecules for these low helium flows (less than 2 sccm). We found that a coating on the inside of the buffer gas cell of Y_2O_3 nanopowder helped improve yield at low buffer gas flow rates. However, we also found that too much nanopowder coating is also detrimental. The cell is coated by mixing the nanopowder, which has particulate size less than 50 nm (Sigma Aldrich 544892), with isopropanol and then brushing onto the intrior cell surfaces. After drying, the coating stays adhered to the copper, though is easily rubbed off with contact. Images of the coated and overcoated cell are shown in Figure 4.1. We found no adverse effect on vacuum pressure due to the coating of the cell. Since the ablation laser itself only hits the Y_2O_3 target, and not the dust, it is possible that some other kind of nanopowder would also suffice to yield this improvement or perhaps be even more influential.

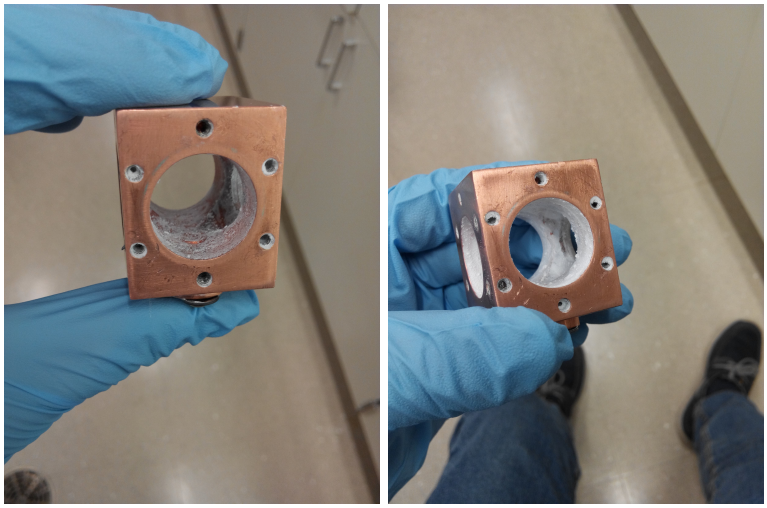

Figure 4.1: Left: Buffer gas cell well-coated with Y_2O_3 nanopowder. Right: Cell with too much nanopowder coating.

The variation of the peak signal size for different helium rates for the powdered and unpowdered cell is shown in Figure 4.2. From this, we find that the nanopowder in the cell not only

increases the molecule number, but also allows for the system to be run at a lower helium flow rate. This is a win on both accounts for us.

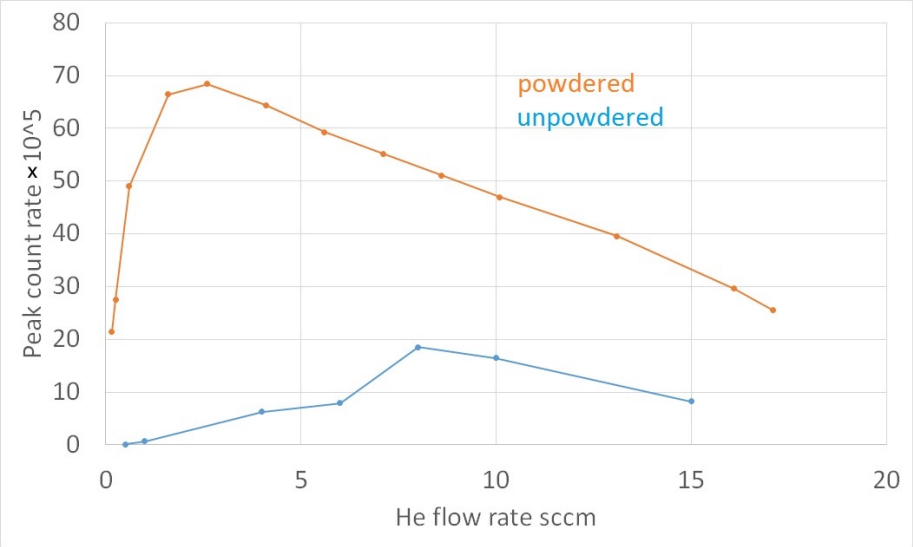

Figure 4.2: Comparing the peak molecule number produced vs flow rate for the unpowdered and powdered cell shows that the powder improves molecule number as well as allowing operation at lower helium flow rates.

The other thing that needs to be verified is that the molecules are not arriving too quickly using the powdered cell, the results of which are shown in Figure 4.3. We find that for a given flow rate, the cell with nanopowder produces molecules that arrive in the detection region in about half the time of the unpowdered cell. However, when running at a lower flow rate such as 1 sccm, the molecules' velocity is similar to the 5 to 10 sccm range we had been using for the unpowdered cell, and so the velocity is not a concern. We find in both cases that the peak time for molecules exiting the cell is 2-2.5 ms.

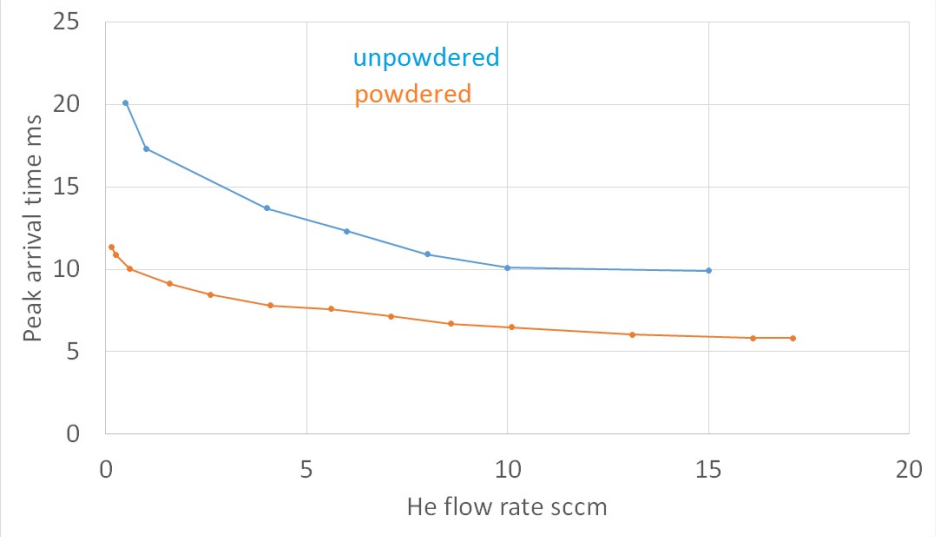

Figure 4.3: For a given flow rate, the YO produced is faster for the powdered cell than the unpowdered cell. However, the velocity of the powdered cell at low flow rates is commensurate with the velocity of the unpowdered cell at higher flow rates.

We did not discover the usefulness of the nanopowder coating until after the oxidizer tests described in the remainder of this chapter, so it could be nice to go back and repeat with the dust coating and see if we achieve different results with different molecule production methods. Additionally, this implies that the absolute number for the following studies is low because we were using a clean cell instead of a coated one for the tests.

4.3 Cell modifications

One of the largest modifications made since our most recent published work [20] is the transition from using a two-stage buffer gas cell to a single-stage cell. This made the molecules we produced faster, but we produced many more of them, as shown in Figure 4.4. However, we have never experimented with different mesh sizes, different spacings of the second stage from the first, and so on. This suggests that there is a possibility of a modified two-stage cell still being effective for us, but with the much larger number produced with our single-stage compared to our two-stage we moved forward with the single-stage buffer gas cell.

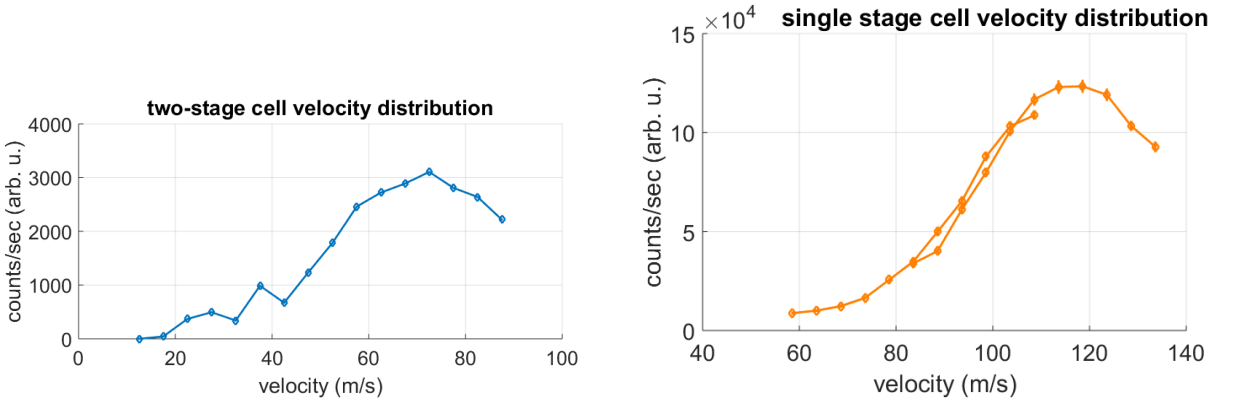

Figure 4.4: Velocity distribution for molecules produced from the old two-stage cell (left) and the single stage cell (right). The two-stage cell data was taken at a helium flow of 5.5 sccm, while the single stage data was with a helium flow of 3 sccm. Velocity sensitive detection is performed via LIF from a low-power probe beam at 45 degrees with respect to the molecular beam axis with detuning chosen to detect a specific velocity class.

While in the past we used a repetition rate of 10 Hz in our experiment for fast data acquisition, we find that the buffer gas cell does not behave similarly across different YAG laser repetition rates. As shown in Figure 4.5, the distribution of molecule arrival times of the unslowed beam varies both in timing and in beam brightness. While the total number increases by a factor of 6 with the reduced repetition rate of 1.4 Hz, the peak time-of-arrival also shifts earlier. This time shift corresponds to a peak velocity produced by the cell of 120 m/s instead of the 105 m/s produced by a 10 Hz rate.

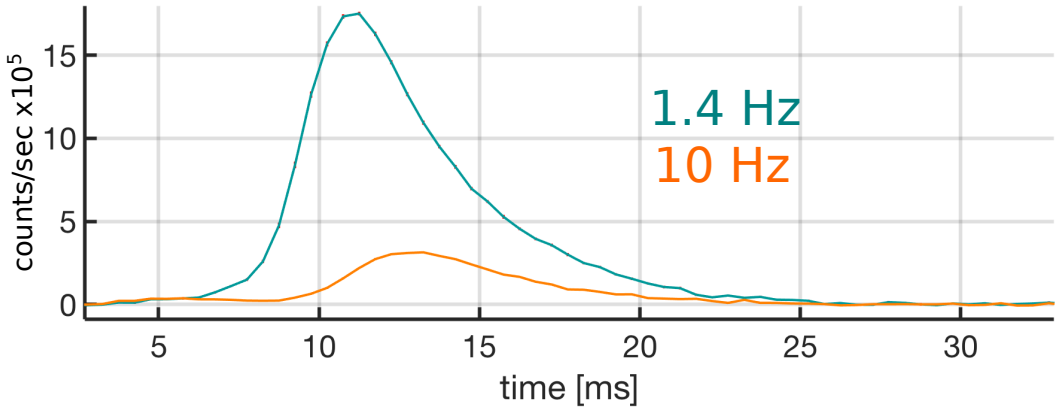

Figure 4.5: Comparison of different YAG laser repetition rates. The signal detected is LIF by unslowed molecules transiting the MOT region. The detection beam is 10 mW and orthogonal to the molecular trajectory with zero detuning.

We have also experimented with a couple of different cell main bore sizes– 22 mm diameter and 27 mm diameter, as shown in Figure 4.6. The number is significantly (about a factor of 2) improved for the smaller bore cell, despite the slightly faster molecules that are produced. So, we now have the smaller bore size cell installed, though we have not yet tried even smaller bore sizes due to the slow experimental turn-around of trying various cell geometries. It would definitely be interesting to try even smaller bores if time permits to see if the trend of more molecules with decreasing interior cell size continues.

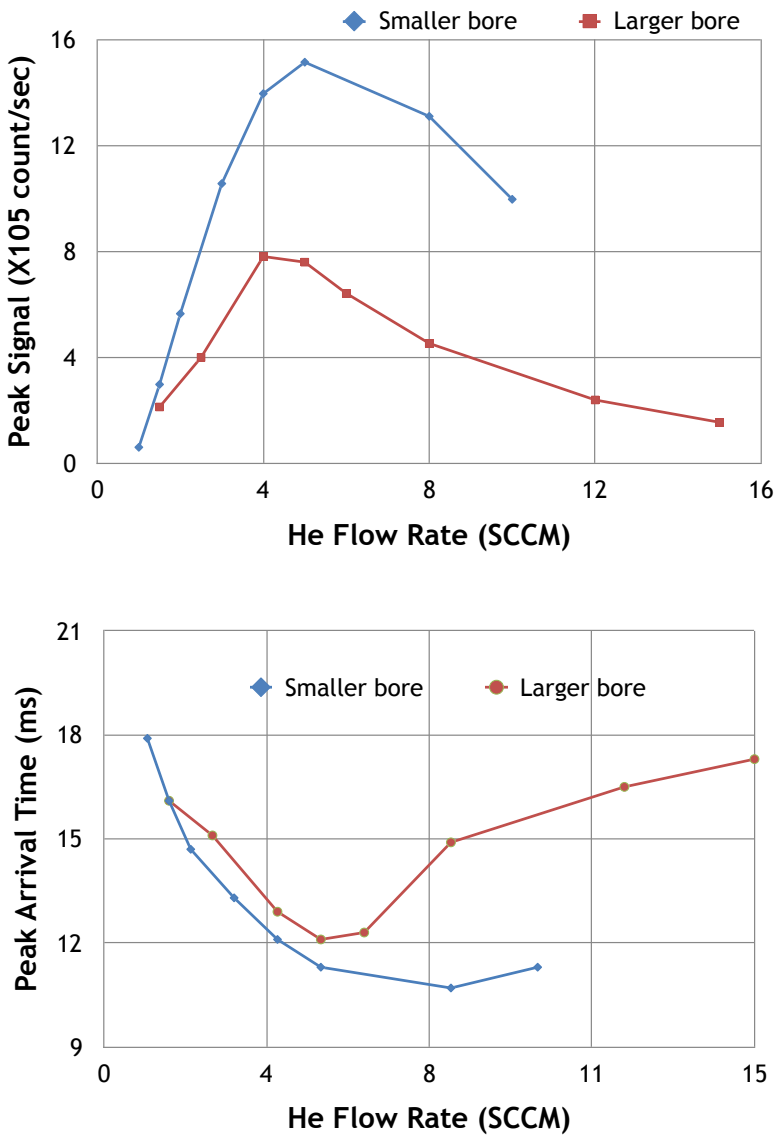

Figure 4.6: Peak molecule signal (top) or peak time of arrival (bottom) for different flow rates with the smaller bore (22 mm, blue trace) or larger bore (27 mm, red trace) cell.

As shown in Figure 4.7, varying the size of the front aperture of the cell does not increase the number of total molecules that can be produced, but improved the number at a given flow rate, allowing for running of the cell with a smaller helium load. The average initial velocity of the molecules is also modestly increased for a given helium flow rate. We have not yet attempted even smaller front apertures, though it is possible it would continue to improve molecule production at

low helium flow rates.

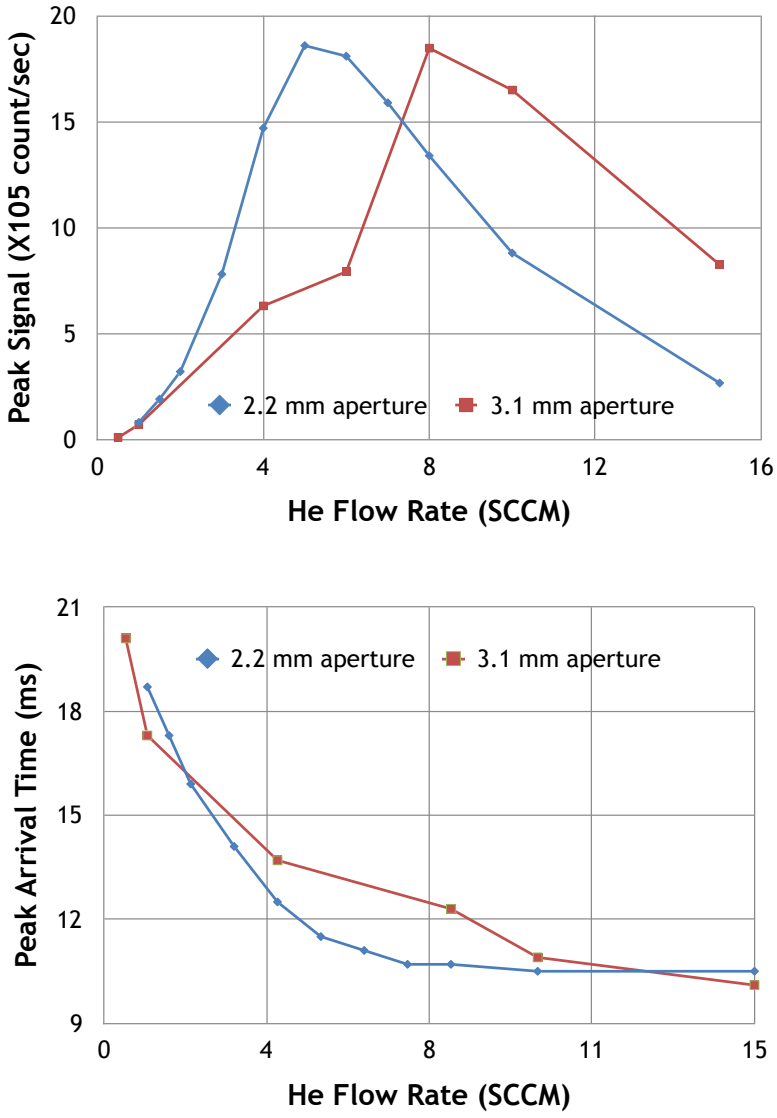

Figure 4.7: Peak molecule signal (top) or peak time of arrival (bottom) for different flow rates with a 2.1 mm front aperture (blue) or 3.1 mm aperture (red).

Following the lead of the Doyle group at Harvard [57], we also installed a diffusion plate at the rear of our buffer gas cell. This plate prevents helium from directly entering the cell from the fill line by requiring a few collisions with the plate and the back of the cell before entering the main volume. Interestingly, the number of slowed molecules improved with the diffuser, as shown in

Figure 4.8, while the initial number was relatively unchanged. This is possibly because the diffuser plate prevents helium from directly leaving the cell and colliding with the molecules during the slowing time, or that it improves thermalization of the helium with the cell.

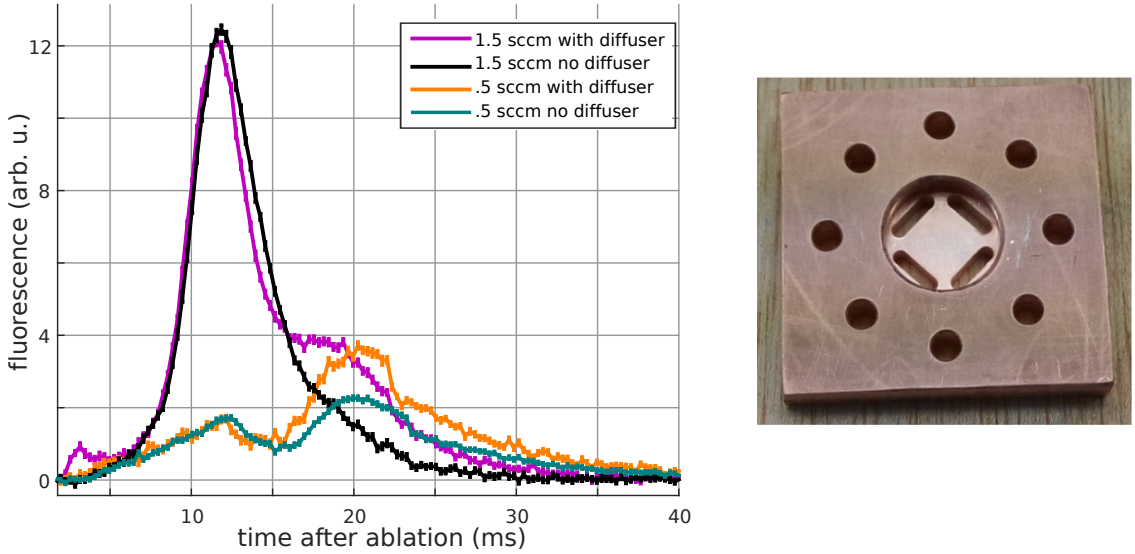

Figure 4.8: Comparison of behavior with same attempted MOT and slowing sequence with and without the diffuser installed in the cell for 0.5 and 1.5 sccm. On the right is a picture of the diffuser plate which is placed between the He inlet and the rest of the buffer gas cell.

4.4 Oxidizers

At room temperatures, it has been shown that production of YO via ablation of a Y_2O_3 target is increased by the presence of oxygen [58]. In order to test the theory in our system that adding an oxidizing gas along with the helium in the buffer gas cell would improve production of YO, it was necessary to modify the cell to accomodate an extra gas fill line. We modified the back plate of the cell to hold another fill line that punched through the diffuser plate. We utilized an Ultem spacer between the line and the cell to prevent icing, as well as attaching a resistive heater to the supplemental gas line to prevent clogging due to gas freezing in the line. We then flowed (controlled by another mass flow controller) in various flow rates of oxygen into the cell to see how it affected

YO production, as shown in Figure 4.9

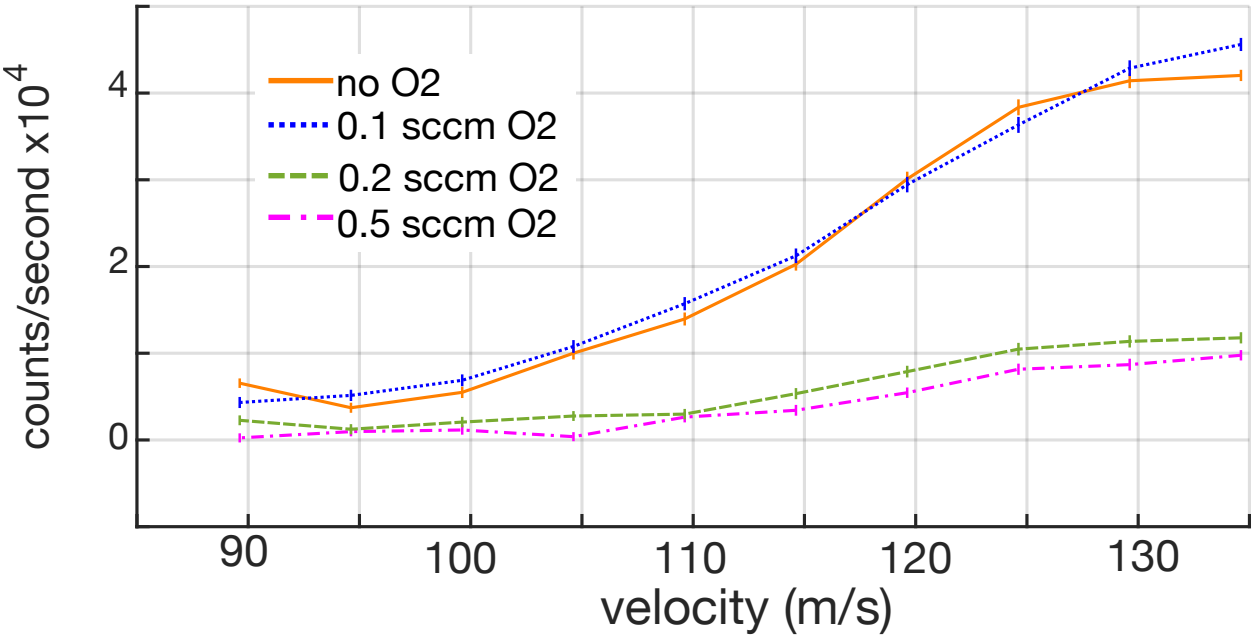

Figure 4.9: Resulting number and velocity distributions of YO produced with 10 sccm of helium buffer gas and varying levels of oxygen gas flowed into the cell. Counts are average counts over a 10 ms window in which the vast majority of molecules reached the detection region.

Small amounts of oxygen (less than 0.1 sccm) do not adversely affect the production of YO, but also do not improve the molecule production. For larger oxygen flow, we find that the production of YO is actually greatly diminished.

Similarly, we used an ozone generator to turn the oxygen into a oxygen/ozone mixture before flowing it into the cell with results as shown in Figure 4.10. The generator when running at maximum ozone production could convert 6 percent by weight of the gas to ozone.

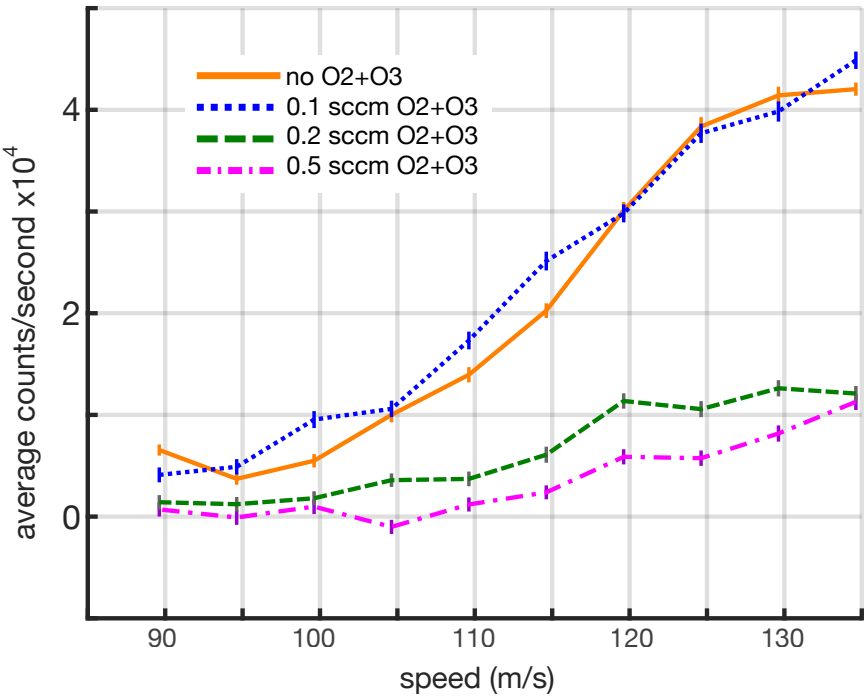

Figure 4.10: Resulting number and velocity distributions of YO produced with 10 sccm of helium buffer gas and varying flow levels of a 94% oxygen and 6% ozone gas mixture flowed into the cell. Counts are average counts over a 10 ms window in which the vast majority of molecules reached the detection region.

To our frustration, ozone also did not improve the number of YO that we were producing. We repeated these experiments for a range of helium buffer gas flows, from around 1.5 to 15 sccm, and saw similar trends throughout: added oxidizers only decreased the production of YO. This trend also held when using N_2O as the supplemental gas.

4.5 Yttrium metal

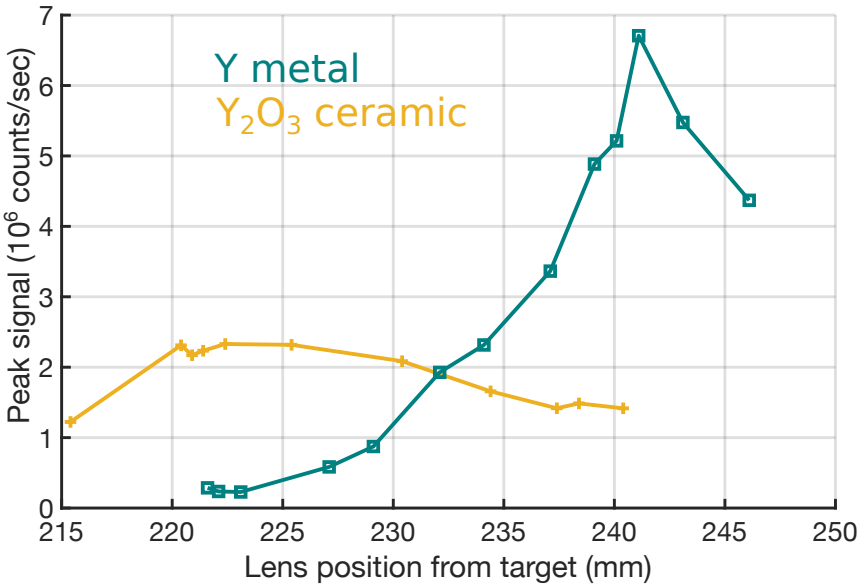

Figure 4.11: Dependence on ablation lens position for Y metal and Y_2O_3 targets.

By placing both a Y_2O_3 and a Y metal target into the cell, we also compared the production of YO. We ensured that the different targets had their faces at the same distance from the albation lens. For this comparison, we used 5 sccm of He for both cases, with an additional 0.25 sccm of O_2 gas for the metal ablation. We used a 7 mJ, 532 nm ablation pulse with a collimated beam width of 4.7 mm. The beam was then focused with a 300 mm focal length lens onto the target. In order to characterize the different targets, we scanned out the peak YO molecular signal by adjusting the ablation lens distance from the chamber, yielding the traces shown in Figure 4.11. Here we find that the dependence on ablation lens position is more sensitive for Y metal ablation as opposed to Y_2O_3 ceramic ablation. Additionally, the optimal distance of the lens with respect to the cell is farther for metallic targets than ceramic. Unfortunately, we do not know where the absolute focus of the laser was at this time with respect to the ablation lens.

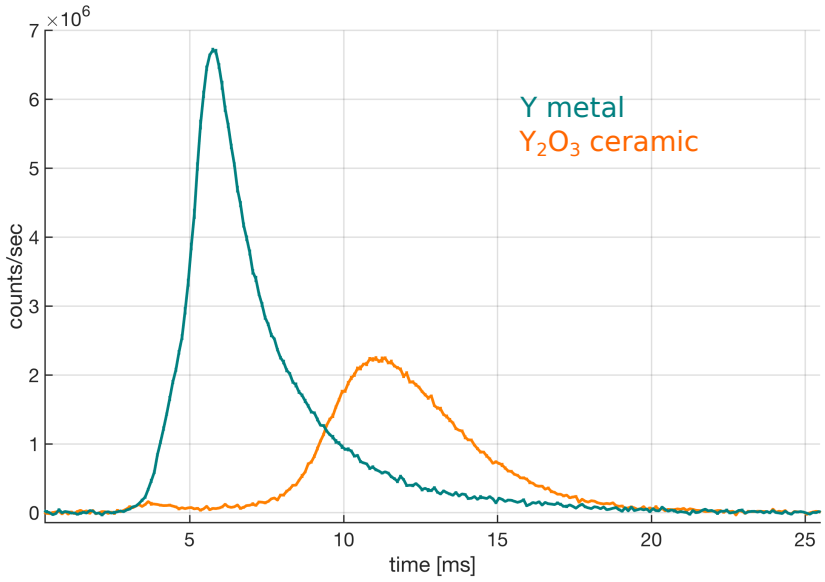

Figure 4.12: Comparison of Y metal + O_2 with Y_2O_3 ablation.

By placing the ablation lens at the distance with the peak molecular yield for the respective target, we find the results as seen in Figure 4.12. Though the total integrated signal is approximately 1.8 times higher for the Y metal ablation, we find that the arrival time is much earlier as well. This arrival time corresponds to a YO beam of 300 m/s for Y metal ablation, compared to the more typical 120 m/s we find from Y_2O_3 ceramic ablation. So, while ablation of yttrium metal allows for more total molecules to be produced, extending the chamber and our lasers' chirp range in order to slow molecules to rest from 300 m/s would be technically challenging. Additionally, because of transverse divergence and the longer time needed to slow from higher velocity, it is likely that the total number of slowed molecules could not be improved by switching to metallic targets. In order to determine whether the velocity difference between the targets is intrinsic to the different materials involved or due to the change in lens position, we also performed a cross check of peak molecule velocity with respect to ablation lens position for the two targets, as shown in Figure 4.13. For this measurement, we extrapolated the velocity from the known cell-to-detection region distance and assumed a constant cell exit time of 2.5 ms, which we find does not tend to vary greatly. Here we find that for ablation lens distances less than$\sim$235 mm to the target, there is a not a large change

in peak beam velocity upon changing target materials. For larger lens-target distances, the peak speed created by the Y metal target is larger than that for the ceramic target.

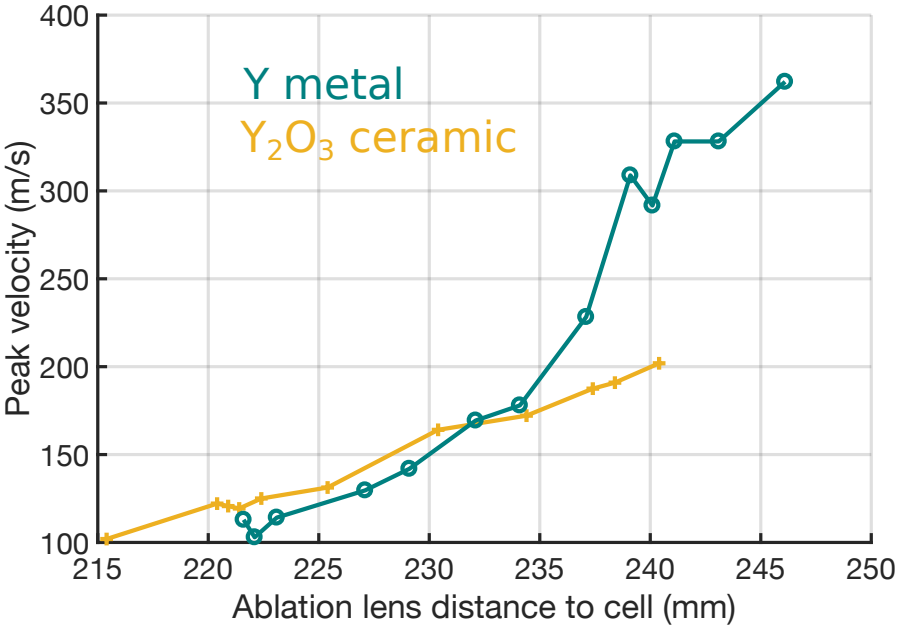

Figure 4.13: Peak velocity of YO beam vs ablation lens position.

4.6 Conclusion

While we found that adding oxidizers to our buffer gas cell in hopes of improving YO production was fruitless, we did gain some insight into cell modifications that were helpful. By removing the second stage from our buffer gas cell we greatly increased the number of YO produced from our cell, though with the tradeoff that the mean velocity was increased to ∼120 m/s. We found that a smaller bore size of the buffer gas cell improved the number of molecules produced. A smaller front aperture of the cell did not improve maximum number, but it did allow for running the system at lower helium flow rates, which will help keep vacuum pressures down. A diffuser plate installed at the rear of the cell between the helium line entry and the main volume of the cell improved our ability to slow molecules (though did not change initial numbers). Lastly, we found that coating the buffer gas cell with Y_2O_3 nanopowder improved the production of molecules, particularly for

low buffer gas flow rates.

Chapter 5

Slowing molecules to trappable velocities

5.1 Introduction

In order to improve our signal to noise ratio when looking for a MOT signal, as well as to produce a larger MOT, we invested time in improving our slowed molecule signal above our first proof-of-principle demonstration [20]. In 2014 when we first realized the slowing of molecules to below 10 m/s, we wanted a molecular source that produced molecules as slow as possible, to minimize the technical difficulty of the slowing process itself. At that time, the original unslowed packet contained approximately 7000 molecules reaching the detection region [51], of which 0.1 percent could be slowed to velocities less than 10 m/s [20]. While this signal was large enough to definitively confirm that our slowing was succesful, the number was not large enough to be encouraging for loading into a MOT. The laser system was set up such that the slowing lasers addressing the molecules could have their frequency chirped from resonance with 65 m/s molecules to 35 m/s (a frequency chirp range of 48 MHz for the main cooling transition), and relied on white light sidebands applied by EOMs and the Pockel's cell to interact with molecules beyond that range.

5.2 Large cell modifications

While for our initial demonstration of slowing we wanted to start with as slow of a molecular source as possible, for advancing our system we wanted to increase the total number of molecules. Because of this, we switched from a two-stage buffer gas cell as in References [20, 52] to a single stage cell. The second stage of the buffer gas cell is 'leaky' and so has a lower helium density, allowing

the molecules to have a couple more collisions with cold helium and reducing the forward boosting seen with a higher density of molecules. This reduces the velocity spread and initial velocity of the beam of molecules produced at the expense of molecule number. In our case, we found that the tradeoff was more favorable to have an increased amount of slowing necessary but to start with more molecules, as mentioned in Chapter 4. Removal of the second stage increased the peak molecular velocity from around 70 m/s to 120 m/s, while also increasing the velocity dependence on helium flow rate, allowing for more optimization options for slowing and trapping. This effect is shown in Figure 5.1. The removal of the second stage also increased the initial molecular number of YO by about a factor of 400.

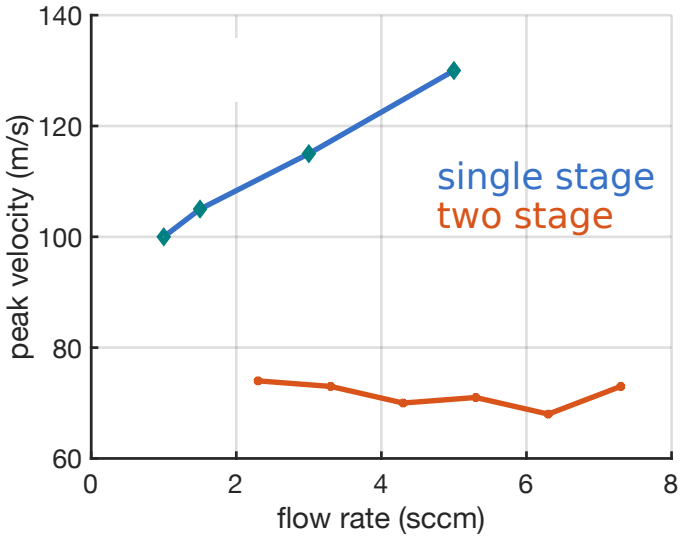

Figure 5.1: Dependence on helium buffer gas flow rate of peak YO velocity produced from single and two stage cells.

In order to slow molecules with the increased initial velocity, it was necessary to modify our laser system to have an extended frequency chirp range. In the process, we also changed our frequency locking scheme. While in the past we chirped the entire frequency comb to pull the main slowing and repump lasers, and then compensated the detection laser to stay fixed, we have transitioned to a method where the comb stays fixed. Since the MOT beams need to be fixed in

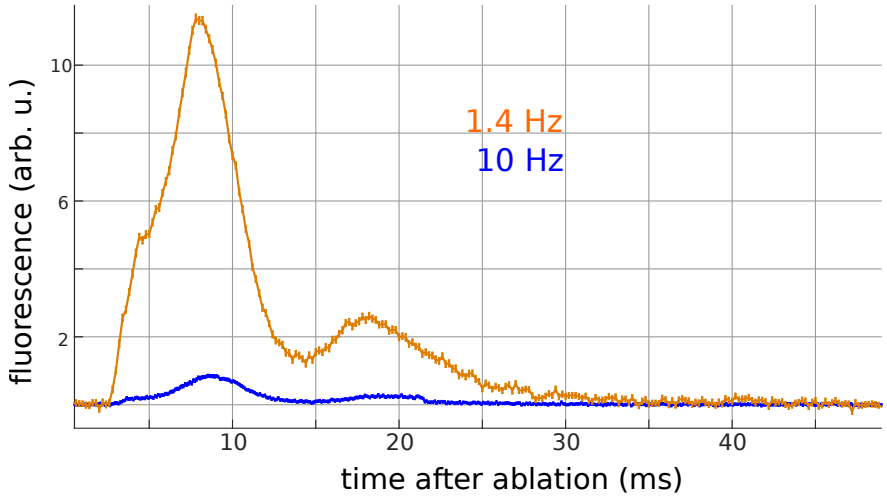

Figure 5.2: Molecule LIF during and after the slowing sequence (slowing ends at 21.5 ms) for different repetition rates of the ablation laser.

frequency, this relegated all frequency chirping to AOMs associated with the slowing lasers, instead of putting strain on the laser frequency locks by having all master laser frequencies chirping. More details of the current frequency locking scheme are detailed in Appendix B. Our expanded chirp capability now lets lasers continually address molecules from 120 m/s to 5 m/s in the slowing beam while providing enough power to properly seed the tapered amplifiers for the repumps and to seed the Raman laser for the main slowing transition.

Another straightforward but critical improvement in our system was to reduce the experimental (YAG fire) repetition rate from 10 Hz to around 1 Hz. With the slowing beam on, this change shows an even larger increase of molecular signal than the unslowed improvement described in Chapter 4. The slowing beam itself adds a few hundred mW of heat load onto the cell during operation, perhaps increasing the importance of cell rethermalization between YAG pulses. This also points to a potential further improvement by reducing the temperature of the cell or increasing the cooling of the cell after an ablation pulse. Being able to increase the experimental repetition rate, even without an increase in molecular signal, would still improve averaging time.

5.3 White light

In the past we had electro-optic modulators (EOMs) installed in the slowing beam to apply sidebands at 10 MHz to the main slowing transition and to the repumps. Currently, however, we find we have improved slowing without the white-light modulation and instead more finely optimizing the rate at which we chirp the frequency of the slowing lasers. Even without the EOMs, we do still have sidebands due to the Pockels cell polarization switching (5 MHz) and the hyperfine components in the slowing beam (14 MHz). There is a larger hyperfine splitting that is also adressed, but at 760 MHz detuning, these components are too far away to affect one another. We have varied the slowing Pockel's cell chopping rate between 1.5 and 5 MHz, and have not seen a degradation in slow molecule signal within this frequency range. Of course, no Pockels cell polarization switching whatsoever is deleterious to the slowing.

5.4 Optimizations

To produce a large enough flux of slowed molecules to work towards implementing our MOT, we underwent a number of optimizations to our slowing vacuum system, lasers, and timing sequences.

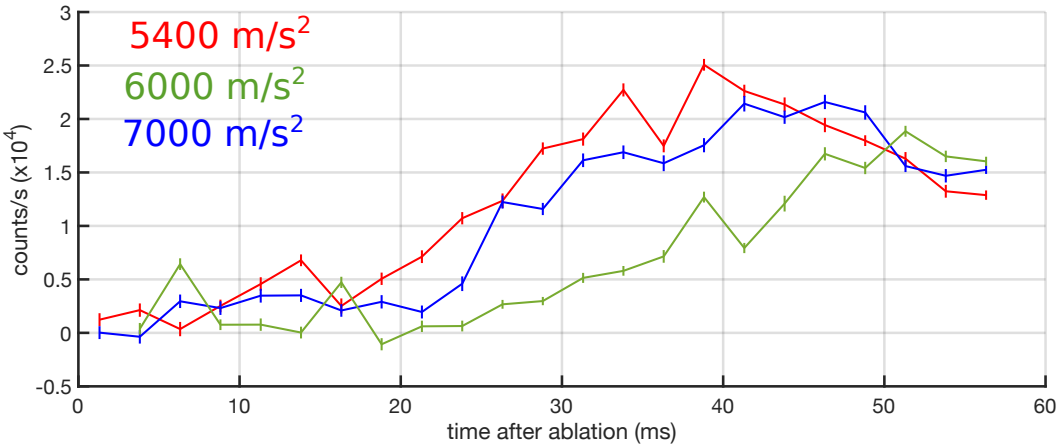

Figure 5.3: By varying the assumed deceleration for slowing sequences designed to slow molecules from 110 to 30 m/s (lasers chirped from resonance frequencies of 100 to 40 m/s) we can determine our actual deceleration rate. These sequences used microwave remixing of N''=2 levels.

To ensure that we had enough power in all the appropriate lasers and microwaves to effect our best slowing, we tried varying the powers in different components. The most critical is the v''=0 laser, yet we still found no reduction in slow molecule signal for an intermediate slowing sequence (slowing to 50 m/s) up to a reduction of 50% in power. The v''=1 repump laser power could be reduced by a factor of 3 before showing any change. The v''=2 repump required a drop in power of a factor of 5 before it began to lose efficacy. The microwave power being delivered to the horns had to be reduced by 30 dB before the molecules produced by this intermediate slowing sequence degraded.

5.5 Helium flow rate dependence

Before installing an in-vacuum shutter we found that slowing to low velocities could better be accomplished with low helium buffer gas flow rates, despite lesser initial molecule number at low flow rates. As shown in Figure 5.4, although 1.5 sccm starts with many more molecules at 100 m/s, for slowing to or below 35 m/s we found that 0.5 sccm produced a greater flux of slow molecules.

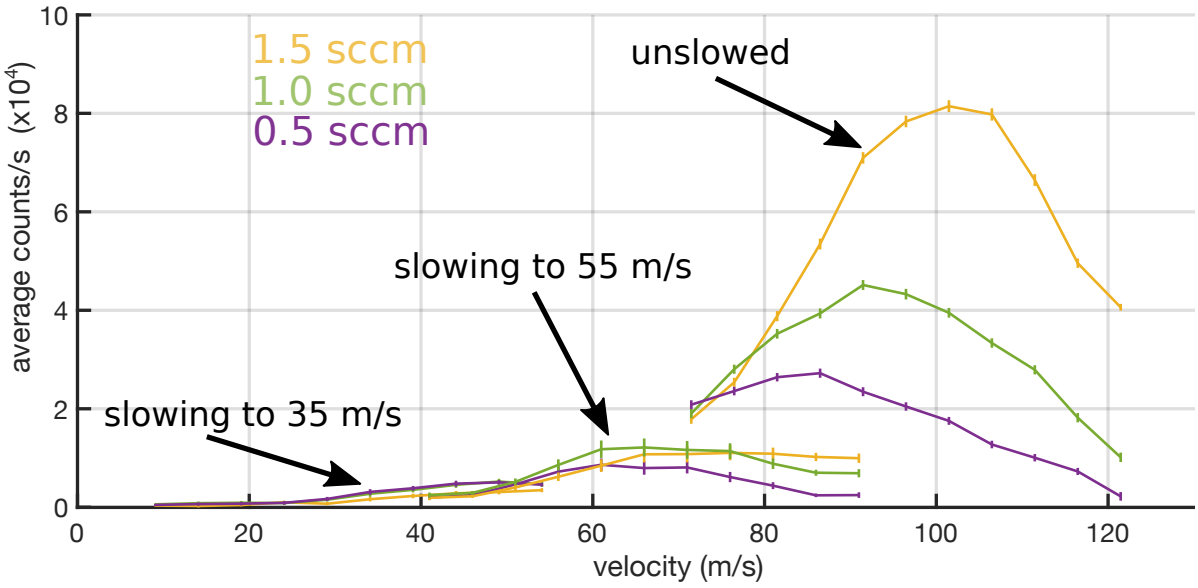

Figure 5.4: Average counts/second over a 12 ms time window occuring after slowing for slowing sequences to 35 or 55 m/s (vs unslowed) for different flow rates (purple: 0.5 sccm, green: 1.0 sccm, and orange: 1.5 sccm). These data were taken before the implementation of the in vacuum shutter.

A possible explanation for this phenomenon is that the vacuum pressure in the slowing region due to the constant helium flow being supplied to the cell is too high. We note that the space in the slowing region is fairly constrained directly outside the cell, and so allowing for larger expansion volume or more cryopumping could help. In addition to reducing the vacuum pressure after the shutter, we find that the shutter also prevents unnecessary heating of the cell, which itself decreases molecule production, as mentioned in Chapter 4. Finally, the shutter should prevent line-of-sight helium from chasing down the slow YO molecules and interfering with the MOT. As will be discussed in Chapter 7, we find that the now installed in-vacuum shutter allows for similar sized MOTs to be loaded for different flow rates, instead of falling off swiftly with increased helium buffer gas flow.

5.6 Optical repumping of N"=2

As discussed in Chapter 2, we have a variety of options for plugging leaks in our molecules' cycling transition. One of the changes implemented that had a large effect on our ability to slow

molecules from production speeds to trappable velocities was to modify the way we repumped molecules that fell into the $X^2\Sigma$ state N''=2, v''=0 level. Following this change, it was necessary to reoptimize our slowing timing sequences. The new optimized deceleration (frequency chirp) rate was congruent with the 60 percent change in number of states coupled /scattering rate for the new optical cycling transition. The optimal deceleration rate for our slowing timing sequences changed from 5500 m/s^2 to 8000 m/s^2, an increase of 60 percent. This implies a photon scattering rate increase from approximately 9.2×10^5 per second to 1.3×10^6 per second. The photon recoil velocity of YO on the 614 nm cooling transition is 6 mm/s.

By integrating the slowed molecule LIF signal for the optical versus the microwave repumping of the N''=2 level, we find that the optical repumping yields a 19× larger flux of slowed molecules. This is a larger effect than we would assume based on the reduced divergence of the molecular beam. The mechanism by which the improvement is so great is not yet determined, but may be due to 'dead' spots along the slowing region for microwaves, whereas the N''=2 optical beam can be very well overlapped with the laser slowing beam. The other possibility, as mentioned in Chapter 2, is the difficulty of using microwaves to pump states with larger F to smaller F, as the potential for polarization dark states arises. While we have done some experimenting with rapid switching between microwave horns at different polarizations to see if that improves the utility of microwave repumping of N''=2, the results have been inconclusive.

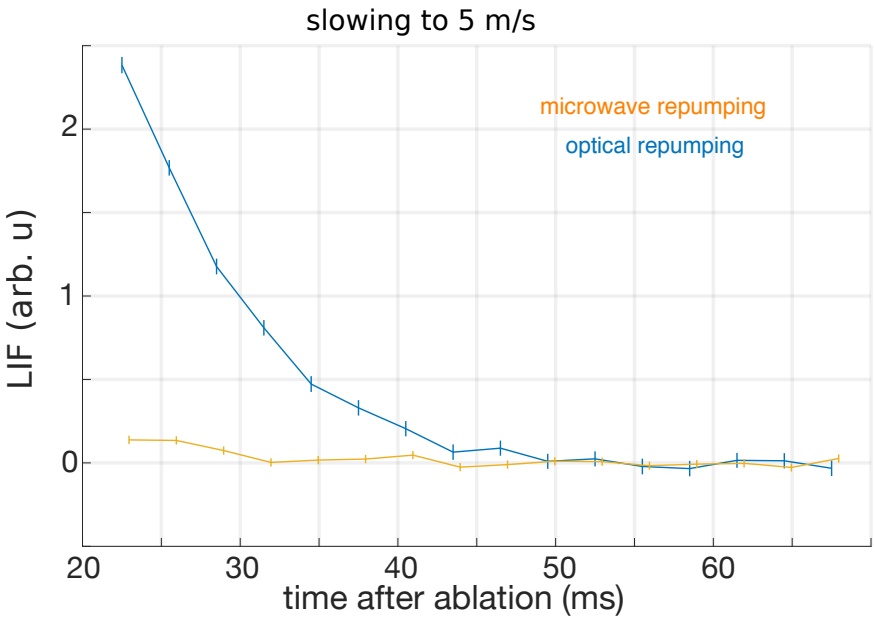

Figure 5.5: Comparison of the effect of N"=2 optical or microwave repumping in slowing on the production of slowed molecules. The same length of vacuum chamber and appropriately optimized frequency chirp rates of the slowing lasers were used.

By choosing different frequency chirp endpoints and slowing timings, we can slow our molecules to our choice of velocity, as shown in Figure 5.6. Timing sequences are determined by using the known propagation distance from the cell to the detection region, assuming a deceleration rate (typically around 6000-8000 m/s^2) and frequency chirping the lasers from the initial frequency minus 10 m/s to the goal frequency plus 10 m/s. Since multiple hyperfine components are addresssed and the Pockel's cell adds sidebands at 5 MHz, the slowing lasers can interact with molecules in a range around their resonance frequency. Timings are designed such that the peak of the desired slow molecules arrive in the detection region immediately after the slowing shuts off, to minimize the effects of transverse divergence.

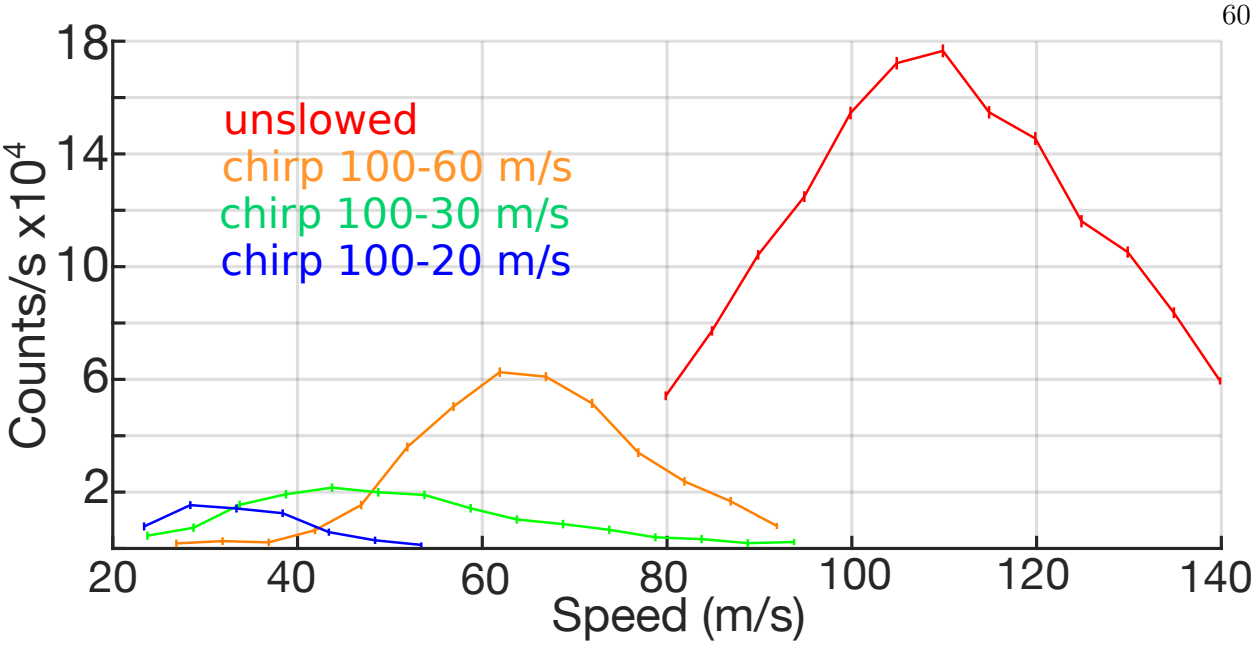

Figure 5.6: Different chirp parameters yield different velocities of slowed molecules. The vertical axis is the average count rate over a 17 ms window ending after slowing detected with a low power Doppler sensitive detection beam. These slowing sequences all utilized optical repumping of N''=2.

5.7 Detection efficiency estimates

In order to turn the fluorescence collected by our PMT or CCD into a total molecule number, we have to determine the total detection efficiency of our imaging systems. The only thing differing between our CCD and PMT systems is the quantum efficiencies of the sensors themselves, which are 93 percent for the CCD and 20 percent for our PMT at our detection wavelength of 614 nm. The part numbers and details of the collection system are discussed more thoroughly in Chapter 3. The collection systems both have a color filter which has 97 percent transmission for 614 nm light, and four anti-reflection coated lenses which each have a transmission of 99.8 percent. The vacuum windows are uncoated, and so have a transmission of 96 percent per interface. We have a geometric solid angle efficiency determined by the size of the first lens and its distance from the MOT region, which for a 2 inch lens 6 inches away is a factor of 1/144. Finally, there is likely an imperfectness factor for the solid angle estimation (not all photons that hit the first lens will

make it to the detector, which is probably of order unity. As a conservative estimate, I will here assume that it is one, giving a worst case molecule number. All these factors multiplied together appropriately yield a photon detection efficiency of 0.58 and 0.12 percent for the CCD and PMT respectively.

For determining the number of molecules transiting through the detection region with the unslowed beam, we use a full power zero detuned orthogonal beam, and assume that our photon scattering rate is 1×10^6 per second (previously determined by shutting off the v"=1 repump and measuring the time constant of loss into v"=1). The transit time through the detection beam for a unslowed molecule moving at 120 m/s is 83 μs, meaning each photon has time to scatter 83 photons. Integrating the counts registered on the CCD or those measured by the PMT gave very similar number estimates after applying the appropriate correction factor, 1.2×10^6 or 1.3×10^6 unslowed molecules transiting the detection region respectively for the CCD and PMT.

For detecting slowed molecules we use a low power probe beam at 45 degrees with respect to the molecular propagation direction. In order to avoid velocity confusion, we shut off the 760 MHz component in the laser beam, so as to avoid attributing faster molecules to the slow molecule signal. Because of the number of states involved, each time a photon is cycled, there is then a 1/12 chance of falling into the unaddressed state. So, each molecule can scatter on average 12 photons before going dark. The transit time through the detection region for a slow molecule is more than 1 ms, which is plenty of time to scatter all 12 photons. By integrating the PMT signal after slowing and assuming 12 photons are scattered by each molecule, we estimate that 5.3×10^4 molecules are slowed to approximately 5 m/s.

5.8 Total gains realized

For production of 5 m/s molecules in the MOT region, we have realized a total change in signal of a factor of 7500 (53000 molecules slowed vs 7). If we define a slowing efficiency as the number of slowed molecules divided by the number of initial unslowed molecules detected in the trap region, we can also compare this metric of our current system to that in 2014. From the

unslowed molecular signal, we estimate a flux of approximately 1.3×10^6 molecules transiting the detection region for a typical molecular pulse on a good day. This indicates a slowing efficiency of 4 percent for our current system taking molecules from 120 m/s to 5 m/s. In contrast, with our old slowing we realized an efficiency of 0.1 percent [20] from 70 m/s to less than 10 m/s. This level of improvement is significant, and was critical for being able to detect and improve our MOT signal, which is detailed in Chapter 7.

While there are likely still further gains to be made in the system, especially in molecule production, the level of slowing actualized here is sufficient for us to load our MOT with several hundred molecules, as will be more comprehensively described in Chapter 7. The largest improvements found were by switching from a repetition rate of 10 Hz to 1 Hz (11×), changing from a 2-stage buffer gas cell to a single stage cell (400×, though at a faster velocity and so requiring more slowing), and switching from microwave to optical repumping of the $N"=2$ manifold (19×). All other improvements to the slowing were of order unity.

Chapter 6

3D MOT coil design

6.1 Introduction

MOT trapping force calculations [21] indicate that we need a magnetic field gradient of about 10 Gauss per cm in the trapping region (approximately 1.5 cm large) in order to effectively load molecules into our MOT. Additionally, in order to not decrease our photon scattering rate due to magnetic sublevel dark states in the ground state, we need to be switching the magnetic fields on the order of the scattering rate (a few MHz). The current and voltage requirements for out of vacuum coils would be enormous do to their required size, and so we have designed and constructed vacuum compatible MOT coils that can yield the required fields and field switching. The current set of in-vacuum coils (before they were blackened to reduce light scatter) are shown in Figure 6.1.

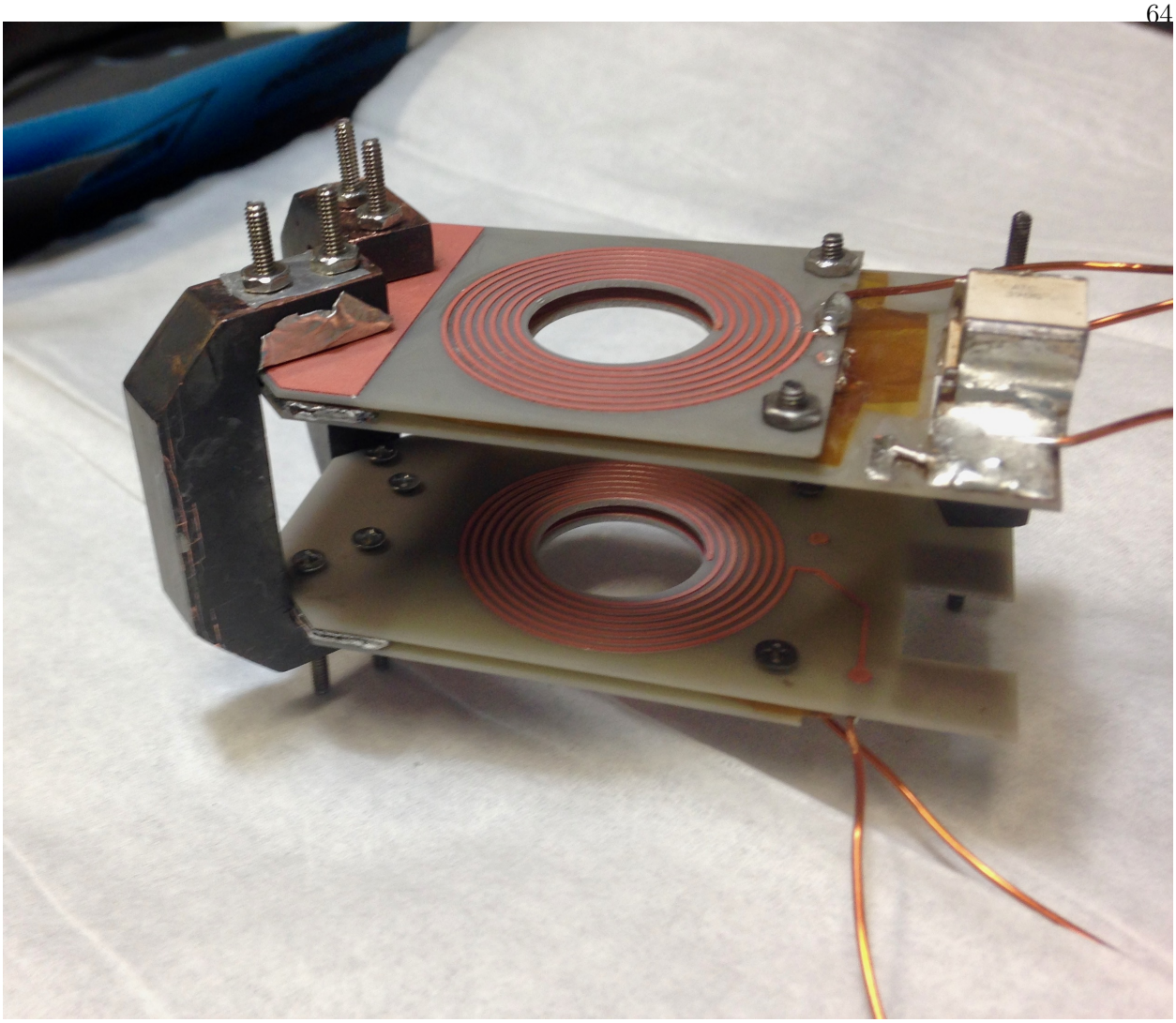

Figure 6.1: The AC magnetic-field producing coils that provide the trapping gradients for our MOT. The blackened copper C-clamps on the left provide the heat dissipation and structural support for the bottom boards. Each board has coil traces on each side, allowing for 4×7 windings on each half of the coils. The white blocks on the top right are the high Q capacitors that tune the frequency of the resonant circuit.

While we initially made MOT coils out of copper coated alumina that could be machined in house, the current MOT coils are on an amorphous aluminum nitride substrate, as the aluminum nitride has a higher thermal conductivity (170 Watts/(meter×Kelvin)) as opposed to alumina (25 Watts/(meter×Kelvin)). In addition, the thicker copper should result in less effect due

to skin depth, more surface area due to thicker traces, as well as reduction of rough edges due to the difficulty of cutting the thin copper. However, the thicker copper also necessitates more spacing between traces, as smaller cutting tools cannot manage the process. Wider gaps between traces also mean we must make the inner diameter somewhat smaller to accomplish the same fields. Additionally, AlN is much harder than alumina, so the cutting must be done with diamond tools, making the fabrication of the coils more difficult. The magnetic field coils currently installed in the chamber were fabricated by REMTEC. The PADs layout schematic of the coils are displayed and explained in Appendix A

There are a number of design considerations that went into the making of the coils. To make a large AC field at 5 MHz, we decided to go with a LC resonant tank circuit, as that is an efficient way to produce reasonably large AC currents. These resonant circuits also build up a large voltage, and so the components need to be high voltage compatible. Because the coil is in a vacuum chamber, we both want to avoid dissipating more power in them than necessary (and so wanting a low loss circuit) as well to have good thermal connection to the outside to prevent overheating. As the coils are close to the MOT beams, we also have to consider ways in which to minimize the scattered light off of them, which is detrimental to our signal-to-noise. Within this chapter I detail some of the considerations regarding impedance matching, the expected magnetic field gradients, the assembly, and the circuitry for making sure the coils are always being driven on resonance.

6.2 Change to parallel configuration of the MOT coils

Up until September 2015, we were running the coils in a series configuration, as shown in Figure 6.2.

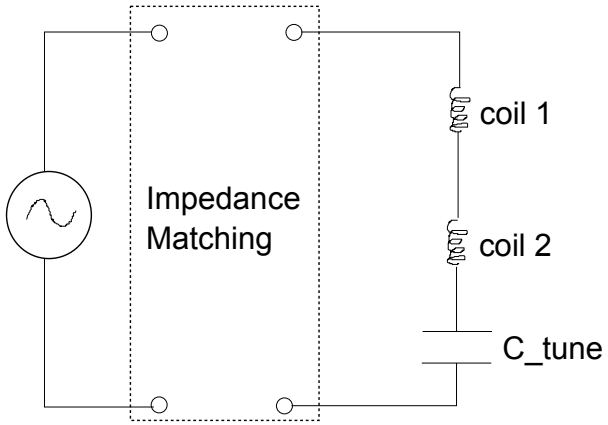

Figure 6.2: Series MOT coil configuration.

While this configuration has the benefit of knowing that the same current is necessarily going through both coils, due to the resonant buildup of voltage between the capacitor and inductors, and dropping half of that voltage over each coil, we were applying an electric field of approximately 450 V/cm between the two halves of the trap. While this would eventually cause problems due to mixing of levels in the $A^2\Pi$ state, thus causing leakage into N"=0 and 2 in the v"=1 state, the more pressing issue is actually the shifting of the N"=0,1,2 levels in the v"=0 state with respect to each other. The shift of the transition in the quadratic regime between two states of opposite parity is given by:

$$\Delta U = \sqrt{(\mu \times E)^2 + (\text{energy}_{\text{field-free}})^2} - \text{energy}_{\text{field-free}} \tag{6.1}$$

The electric dipole moment of YO in the Σ state is 4.5 Debye. With our applied electric field, we were then causing a frequency shift of $\sim$880 MHz on the N"=0$\leftrightarrow$N"=1 transition. Given that our Rabi rate is about 25 MHz [20], this means we are unable to bring our molecules back to N"=1 to continue optical cycling (except during the small amount of time during the 5 MHz switching that we are applying the microwaves at resonance).

In order to address this issue, we rewired the coils in a parallel configuration, as depicted in Figure 6.3.

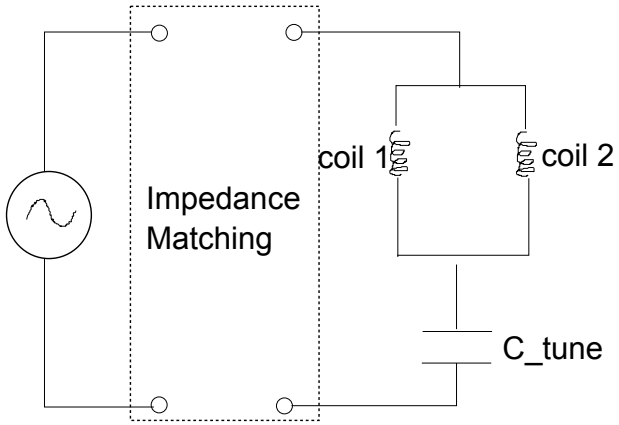

Figure 6.3: Parallel MOT coil configuration.

This design should greatly reduce the electric field we are applying across the coils. With this design, the apparent resistance at resonance for the un-impedance matched circuit (given by the Smith chart function of the network analyzer) is 6 ohms, which is consistent with the 24 ohms we saw in the series configuration. In order to get the 2 Amps necessary to produce our desired magnetic fields, we will still need to drive the circuit at ∼24 Watts. Impedance matching was again achievable with a toroidal transformer, and yielded a -45 dB dip in reflection at resonance. The loaded quality factor Q is 39, again consistent with the impedance of 6 Ohms, the reduction in apparent L of a factor of 4 from the change from the series to parallel configuration, and the factor of 2 between loaded and unloaded Q.

6.3 Impedance matching

The RF amplifier used to drive our coils has a source impedance of 50 ohms, so for maximal power transfer it is necessary to impedance match the coils to appear as if they were 50 ohms to the generator. There are a few different methods to try and accomplish this. What we used for the 2D MOT was a wound toroidal transformer, adjusted to maximize the dip in reflection at the resonant frequency. For the current coils, I was also able to achieve good impedance matching with a toroidal transformer in our set up with very careful winding. The Smith chart from the network analyzer of the impedance matched circuit read 50 ohms at resonance and we achieved a -45 dB dip

in reflection for the impedance matched circuit, indicating very good power transfer.

While we currently use the wrapped toroidal transformer, there are other methods of matching the impedance. It is possible to match the load (purely resistive for our LC tank circuit at resonance) to the source using a matching network designed to operate at the resonance frequency. The simplest network possible is an L network made of two elements, with three elements there are Π and T networks. In Figure 6.4 are depicted the two possible L network configurations, as a low pass or a high pass LC filter.

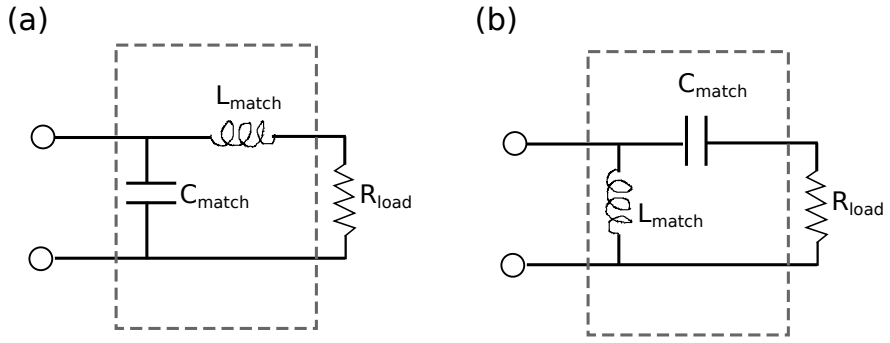

Figure 6.4: Low pass(a) and high pass (b) L-network configurations.

For both configurations, the values of the elements required are straightforward to calculate. The design "$\mathcal{Q}$" (not the same as the quality factor) is given by

$$\mathcal{Q} = \sqrt{R_{source}/R_{load} - 1} \tag{6.2}$$

Then, the reactance of the series leg is given by:

$$X_{series} = \mathcal{Q} \times R_{source} \tag{6.3}$$

While the reactance of the parallel leg is:

$$X_{parallel} = R_{load}/\mathcal{Q} \tag{6.4}$$

For the series configuration board, from the network analyzer we find that our impedance at resonance is 23 ohms. So, our design $\mathcal{Q}$ is 1.08. For an L-network configuration, this means we

can use a low pass configuration with 1300 pF and 1700 nH, or use a high pass configuration with 600 pF and 780 nH. I found that either configuration worked in approximately the same way, so choosing whichever components are easier should be fine. I decided on the low pass configuration, and wound the inductor by hand using an appropriate toroidal core, as none of the bulk ones in stock in that size range allowed for ∼1 Amp of current. With this form of impedance matching, we have a -13 dB dip in reflection, meaning 95 percent of the power is coupled into the MOT coils. The MOT coils were tested in this configuration with high RF power input, and were able to run with 30 Watts of power, and the board temperature rose to 85 °C in air. By using the L-matching network, the perceived loaded quality factor Q will necessarily be smaller than the Q of the tank circuit alone, a.k.a. the unloaded Q which we know to be

$$Q_{unloaded} = \omega \times L/R \ , \tag{6.5}$$

while the loaded Q is

$$Q_{loaded} = Q_{unloaded}/(1+\kappa) = Q_{unloaded}/2 \ , \tag{6.6}$$

where κ is the coupling parameter. For critical coupling (maximal power transfer) κ is equal to 1 and $Q_{loaded} = Q_{unloaded}/2$ [59].

Other options for impedance matching include 3 element matching networks, called Π or T networks, again according to their shape. These are depicted in figure 6.5. In each case, X_1 and X_3 will be one type (inductor or capacitor) while X_2 will be the other type. Both Π and T networks are configured by choosing a virtual resistance in the middle that is larger (T network) or smaller (Π network) than both the source and the load. Then, you make two L type networks, one matching the source to the virtual resistance, the other matching the load, and combine the two. This seemed to frequently require difficult values of circuit components, at least for the parameters of our coils.

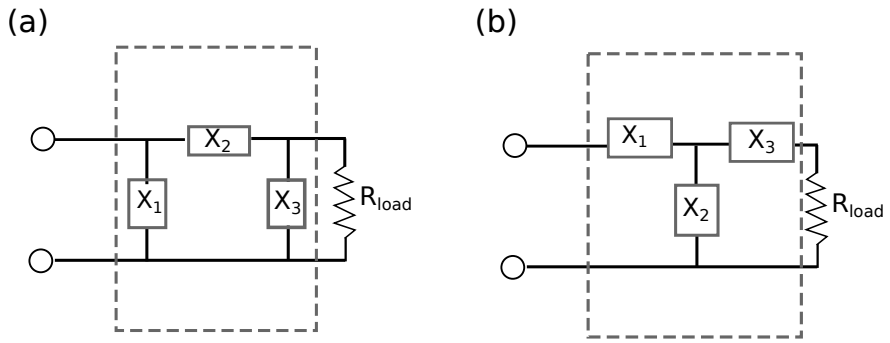

Figure 6.5: Π (a) and T (b) matching networks.

6.4 Magnetic fields

In order to design the coils, we calculate the expected magnetic field due to a set of coils. The boards we use are double sided PCBs. The design we currently have requires 4 layers of coils (two boards) 7 traces wide for each side of the MOT. The coils are 1.2 mm away from each other radially, with an inner diameter of 1.9 cm, z spacing of 1.5 mm, and the large z spacing between halves of the MOT of 2.3 cm. The inner radius and the z spacing between halves are large in an attempt to reduce light scatter from the MOT beams, while the 1.2 mm trace to trace spacing is as small as can be efficiently cut for our PCB material. The small z spacing is determined by the thickness of the boards from which we cut the coils. The current coils are clad in .008" copper (ie 205 μm thick) on an aluminum nitride substrate. The skin depth of copper at 5 MHz is approximately 35 μm, so we should not be limited by the cladding thickness for the resistance of the coils.

In Figure 6.6 are plotted the anticipated magnetic fields and gradients in both axial and radial directions due to the coils, assuming that 1 Amp of current is supplied through each coil. The values are calculated numerically using the Biot-Savart law, and assuming that each spiral was a single circle, with Matlab.

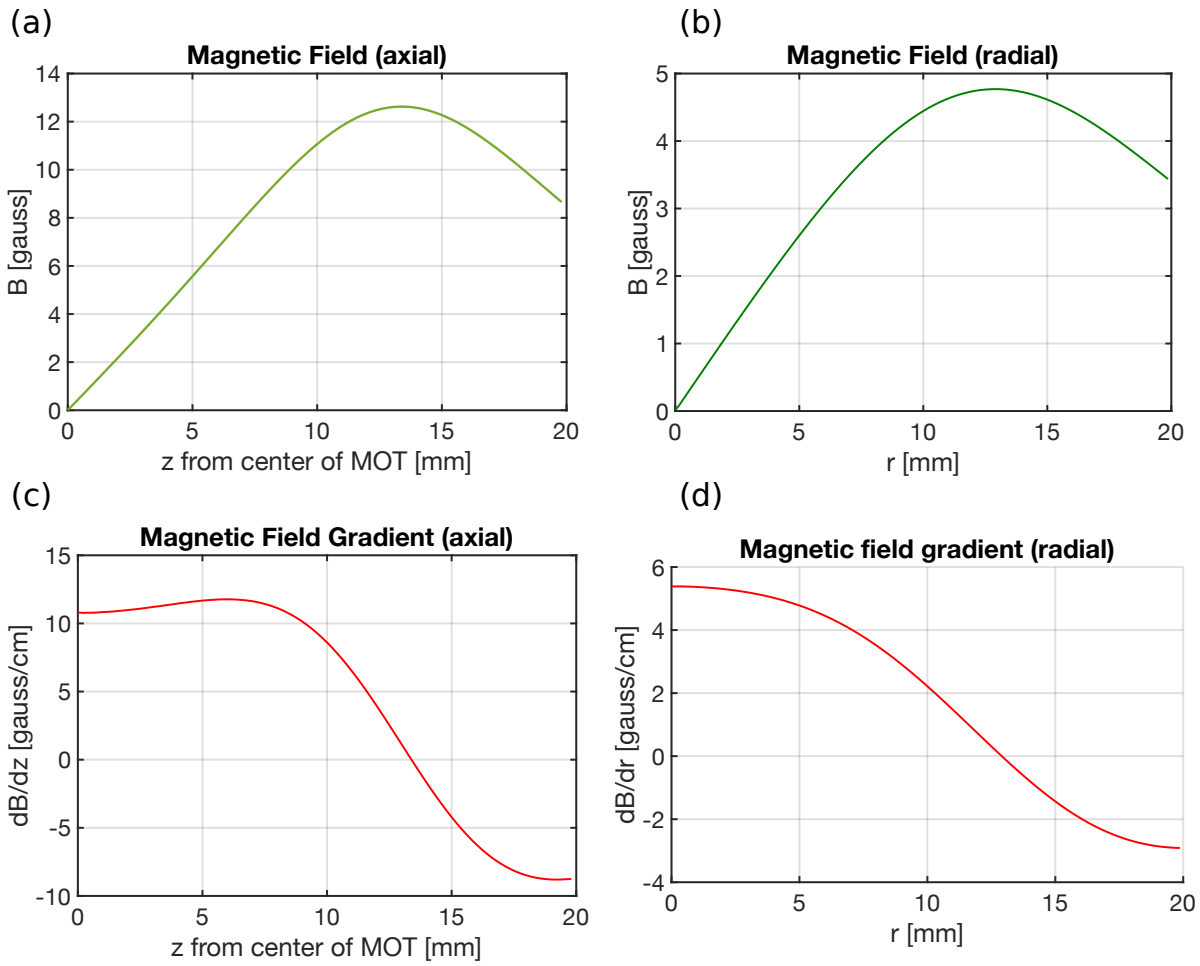

Figure 6.6: Predicted fields (green) and gradients (red) in the axial (left) and radial (right) dimenstions. Fields and gradients are calculated for 1 Amp drive through each coil and scale up linearly with amperage.

6.5 Coil characterization

By driving the coils with a network analyzer on resonance and moving a small pick up coil with a micrometer, we can trace out the magnitude of the magnetic field energy density. The square root of the power ratio picked up then yields a value proportional to the magnetic field strength as a function of position, as can be seen for the axial direction in Figure 6.7.

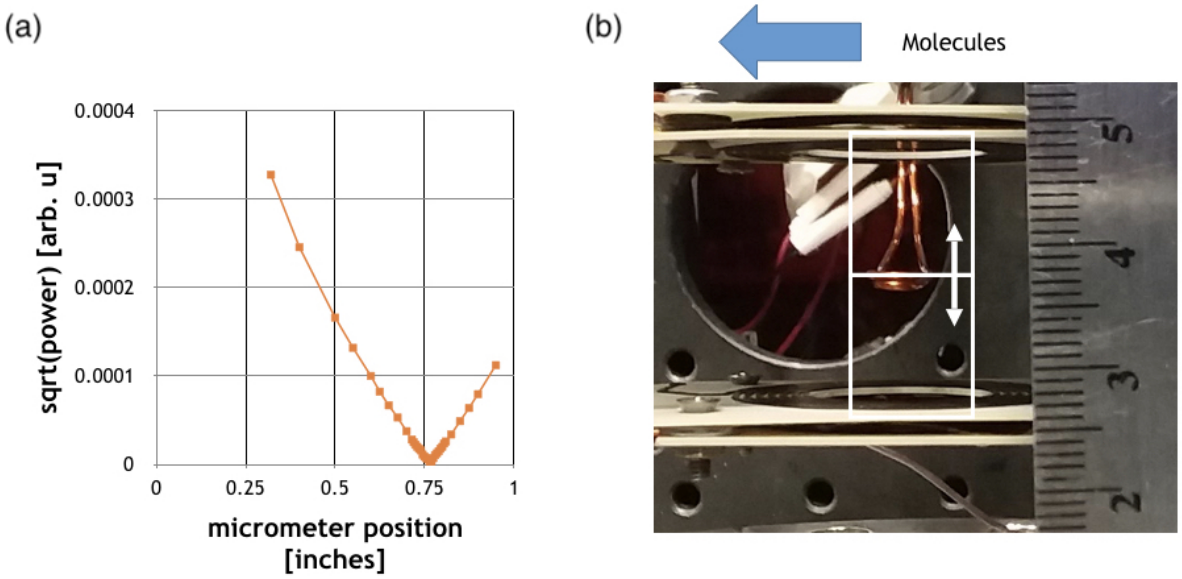

Figure 6.7: (a) Sqrt(ratio of power picked up to drive power) vs position in the axial direction. A quadrupole field should show two linear lines with a cusp at the magnetic field zero. (b) The white horizontal line indicates the expected magnetic field zero location in this dimension with the magnetic pickup coil at the measured zero. The double-headed arrow indicates the direction of the motion of the micrometer.

Similarly, we can perform the same measurement in both radial directions, that parallel to the molecular beam as shown in Figure 6.8 and transverse to the molecular beam as shown in Figure 6.9.

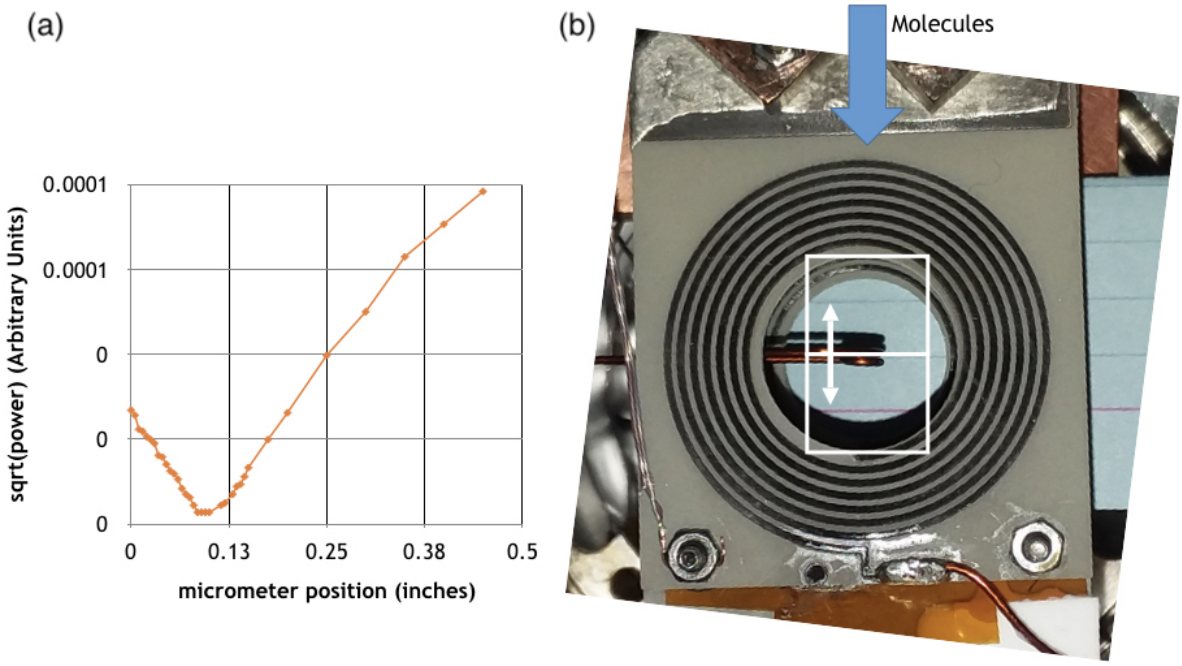

Figure 6.8: (a) Sqrt(ratio of power picked up to drive power) vs position in the radial direction along the molecule propagation direction. A quadrupole field should show two linear lines with a cusp at the magnetic field zero. (b) The white horizontal line indicates the expected magnetic field zero location in this dimension with the magnetic pickup coil at the measured zero. The double-headed arrow indicates the direction of the motion of the micrometer.

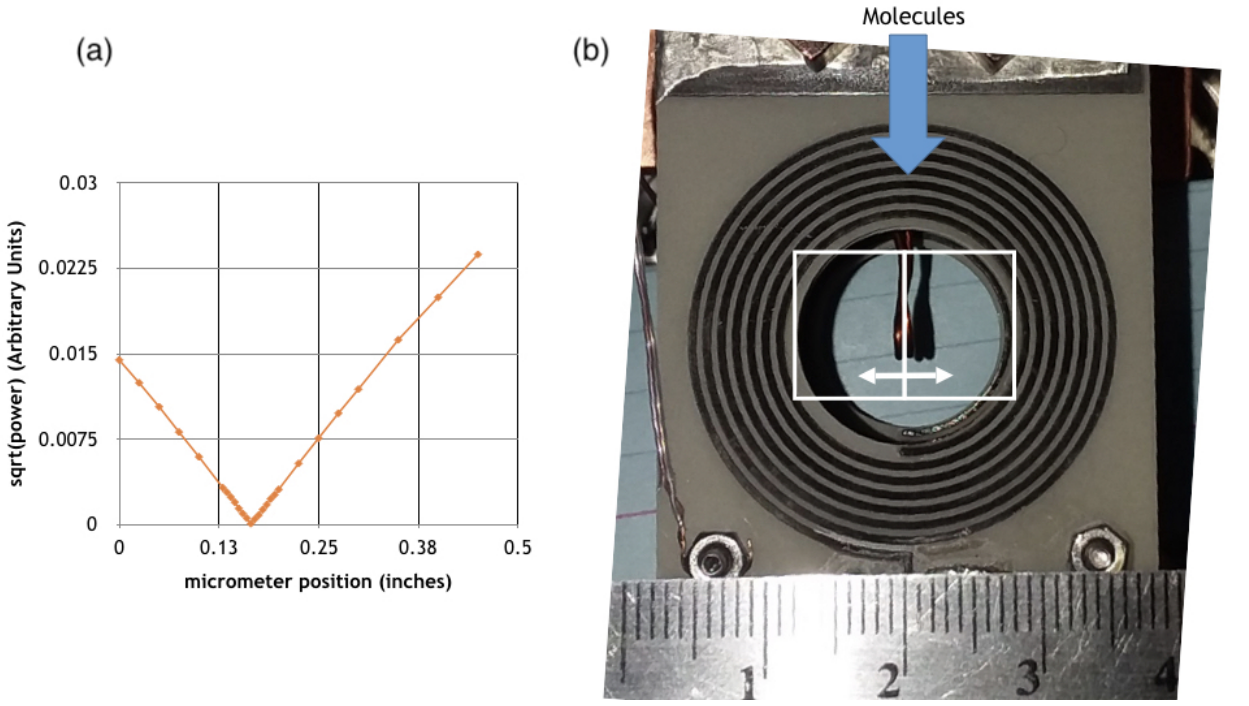

Figure 6.9: (a) Sqrt(ratio of power picked up to drive power) vs position in the radial direction orthogonal to the molecule propagation direction. A quadrupole field should show two linear lines with a cusp at the magnetic field zero. (b) The white horizontal line indicates the expected magnetic field zero location in this dimension with the magnetic pickup coil at the measured zero. The double-headed arrow indicates the direction of the motion of the micrometer.

Together, these AC pickup measurements confirm the uniformity of the magnetic field gradient near the trap center and that the coil is behaving as needed.

6.6 Blackening methods

Because of the laser light in the MOT region from the slowing laser beam and the MOT beams themselves, we wish to have the coils be blackened in some way to reduce light scatter. Because we use fluorescence detection on the same transition as our main cooling transition, we cannot completely avoid signal contamination by light scatter, though an orange color filter does block out the light from the repumps. The components of the board, the substrate and the copper traces themselves present different issues with regards to blackening. Initially we attempted blackening the

coils with the black paint made by Ball Aerospace known as Ball Black or Vac Cote. While it gives a very nice matte black coating, we found that Ball Black is not high voltage compatible (causing arcing between different parts of the board), probably due to a small amount of conductivity of the paint. Confirming this hypothesis is the fact that the measured quality factor Q of the circuit dropped after painting.

In contrast to the failed Ball Black coating, the copper oxide blackening method layed out in appendix G.2 of John Barry's thesis ([53]) achieves blackness of the copper without impinging on the electrical qualities of the circuit. The method involves bringing a sodium hydroxide and sodium chlorite solution to boiling and immersing the copper to be blackened for a couple of minutes to achieve a copper(II) oxide coating on all exposed copper surfaces. This procedure yields a very matte black surface on copper, but does not affect the color of other surfaces. This means that while we can blacken the copper, we do not as yet have a method to blacken the ceramic substrate. However, we anticipate that the copper would be the biggest issue as far as light scatter is concerned.

6.7 Heat link and mounting construction

In order to not have water cooling inside our vacuum chamber, we have a large solid copper heatlink that connects to a high voltage, high amperage, copper vacuum feed-through (Lesker EFT0313753). The outside vacuum end we attach to a chilled water pipe to allow heat transfer. The mounting and in vacuum section of the heatlink is shown in Figure 6.10. The design leaves room for all MOT beams, the longitudinal slowing beam, and side access for PMT and CCD viewing.

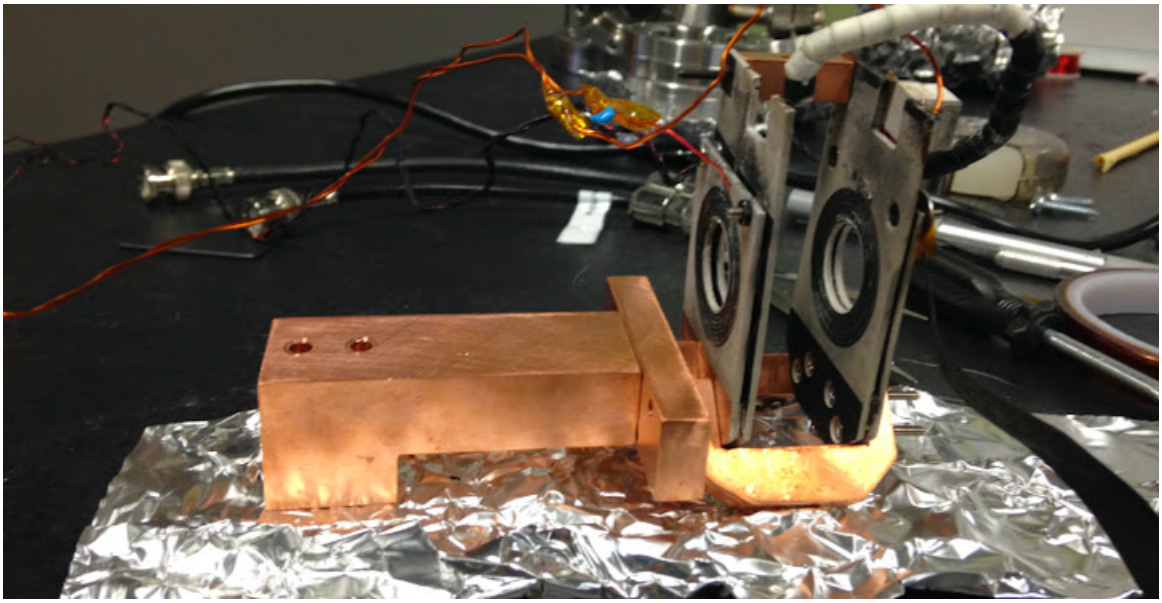

Figure 6.10: Copper heatlink and coil mounts.

In September 2015, we modified the copper electric feedthrough that is our heatlink out of vacuum. Hans bored out the center for us to accommodate a water line going in through the middle and out along the edges and out through a tee in order to get chilled water closer to the coils. Additionally, by cutting some distance off of the feedthrough, the cooling power delivered to the coils was improved. By using a combination of water and ethylene glycol in a chiller, we can run the chiller at -30 degrees C. This then allows the coil to be run at 100 percent duty cycle with 50 Watts input power, with the boards reaching a temperature of 55 degrees C in vacuum. We also can modulate the power of the coils such that they are at low power while waiting for the next experimental cycle, and then full power for loading and trapping. In this way, we can maintain the temperature of the coils at room temperature.The pH of the water/glycol mixture needs to be monitored, as the inhibitor used to prevent corrosion stop being effective after 6 months or so.

Further notes on the assembly of the coils are given in Appendix A.

6.8 Pound locking to resonance of coils

Because the resonance frequency of the coils can drift with variation of temperature, we are currently locking the drive signal to the center of the resonance using the Pound technique [60]. How we achieve this is depicted in the diagram in Figure 6.11.

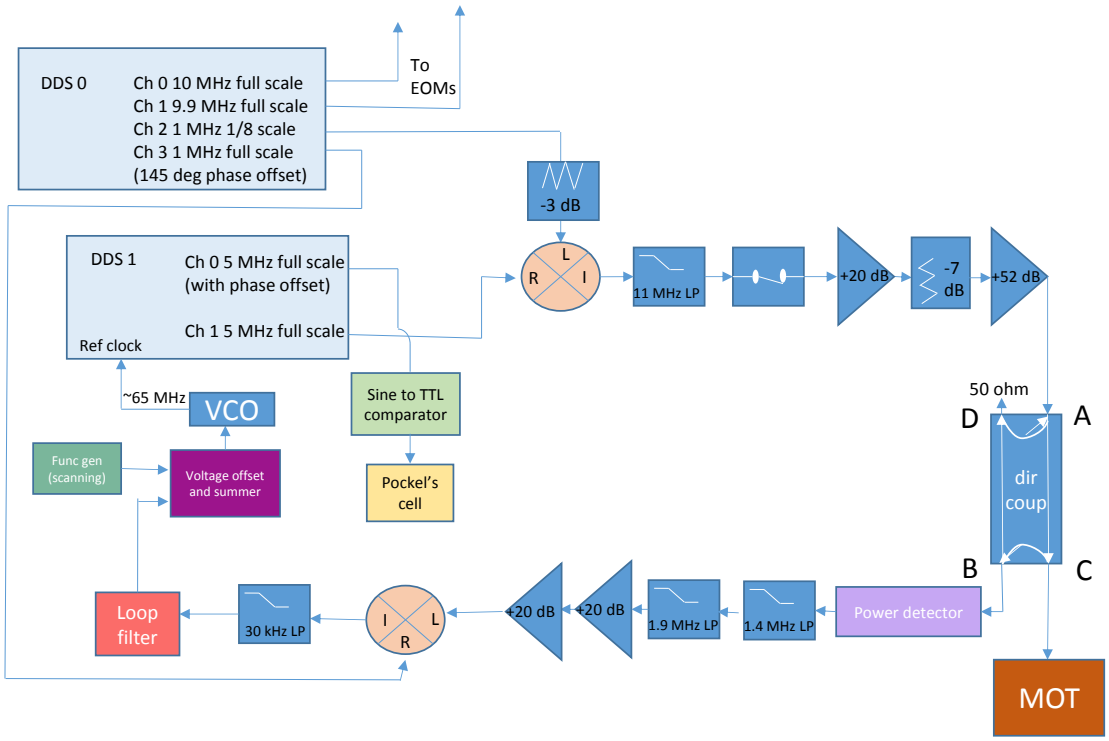

Figure 6.11: Schematic diagram of MOT coil frequency lock. We maintain the drive of our coils on resonance by using a Pound lock. Sidebands to the drive are applied to the coil 1 MHz away, and the signal reflected from the coil is demodulated to DC, giving an error signal we can feed into the loop filter.

By scanning the drive frequency over resonance, we trace out the error signal as shown in Figure 6.12. The center downward crossing is the resonance of the coils at 5 MHz, while the two

upwards crossings are the plus and minus 1 MHz points. One trace is the voltage being applied by the scan, while the other is the lock error signal (while unlocked).

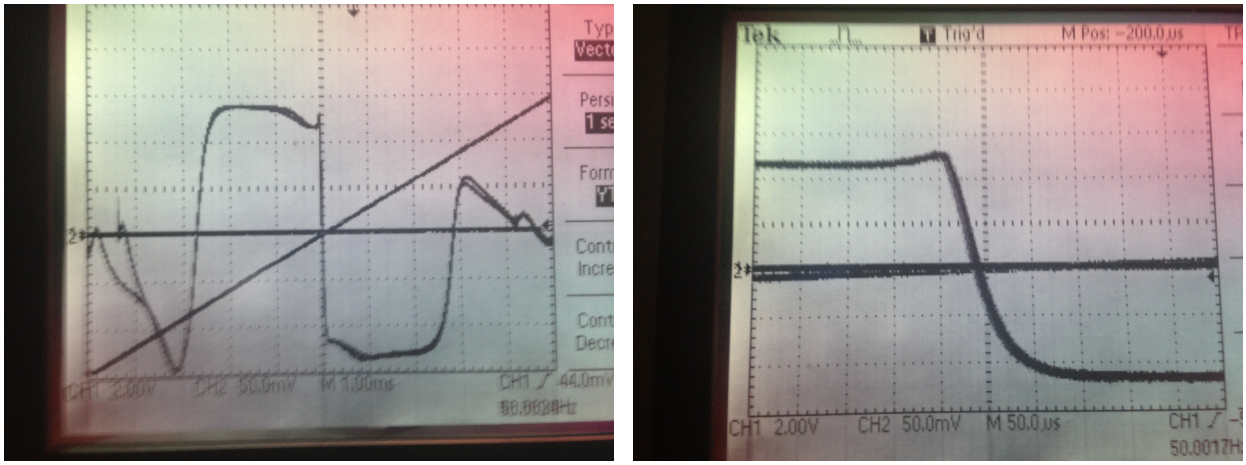

(a) full scale

(b) zoom in

Figure 6.12: Frequency scanning MOT Pound lock error signal.

The VCO driving the clock of DDS 1 is a minicircuits ZX95-100, which has a tuning of 3.6 MHz/V, so we determine that this scan is sweeping out 4.3 MHz/ms for the VCO and .33MHz/ms for the MOT drive frequency. Zooming in on the resonance zero crossing and extracting a slope, we find that the conversion from error signal to MOT frequency error is 0.1 kHz/mV.

Finally, when the servo loop is closed, the error signal tells us our maximum frequency excursion and so phase error. We found that the error signal had maximum excursions of ± 5 mV, which corresponds to frequency excursions of $\sim$0.5 kHz. From the calculated transfer function and the Q for these coils of 70, this indicates that we have a maximum phase error of .02 rads, which should be well below our needed stability.

With the specifics of the MOT coil design and installation discussed, I can proceed to cover the experimental implementation of our MOT in Chapter 7.

Chapter 7

A three-dimensional molecular MOT of YO

7.1 Overview

In this chapter I will discuss some of the considerations that go in place for implementing a molecular MOT on a type II cooling transition. Finally, I present our implementation of the MOT in three-dimensions along with some preliminary analysis of our system.

7.2 Fundamentals of molecular MOTing

As described in Chapter 2, the first step towards laser cooling is a sufficiently closed and rapidlycycling addressable transition in the molecule. While Doppler laser cooling can produce slowing of molecules, in order to actually trap them we require a location-dependent force, in addition to the velocity-dependent force given by the laser cooling. This is achievable by applying a magnetic field gradient and using a transition with a differential magnetic g-factor between the ground and excited state, such that the detuning of the transition with respect to the laser beams has a position dependence. In this case, the center of the trap will be where the magnetic field is zero. The mechanism of this is diagramatically depicted in Figure 7.1.

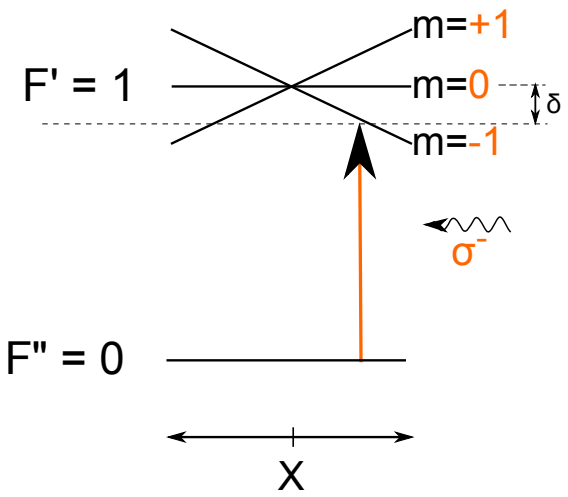

Figure 7.1: Fundamentals of MOT operation: by driving with the correct polarization of light on a transition with a differential magnetic moment between the lower and excited states, a magnetic field gradient in combination with red-detuned (δ) laser beams can provide a restoring force to the magnetic field zero of the trap. Because the magnetic fields produced by two anti-Helmholtz coils are a spherical quadrupole, the helicity of the axial laser beams must be the opposite of that of the radial laser beams.

Because of the strategy used to maintain rotational closure by exciting from a higher to a lower rotational level, the transitions used for molecular MOTing end up being from a larger F'' to a smaller F', complicating the simple picture in Figure 7.1 somewhat [16]. While most atomic MOTs are conducted on a transition like the one in Figure 7.2 (a), where F'' is smaller than F', a few others [46] and molecular MOTs are conducted on transitions as shown in part (b). It is clear to see that while the Type I MOTs allow the atom or molecule to return to a laser-addressable state upon decay to the ground state, we find that there is the possiblity in type II MOTs to decay to states that are only addressable by the anti-trapping MOT beam, which is detrimental to the cooling process.

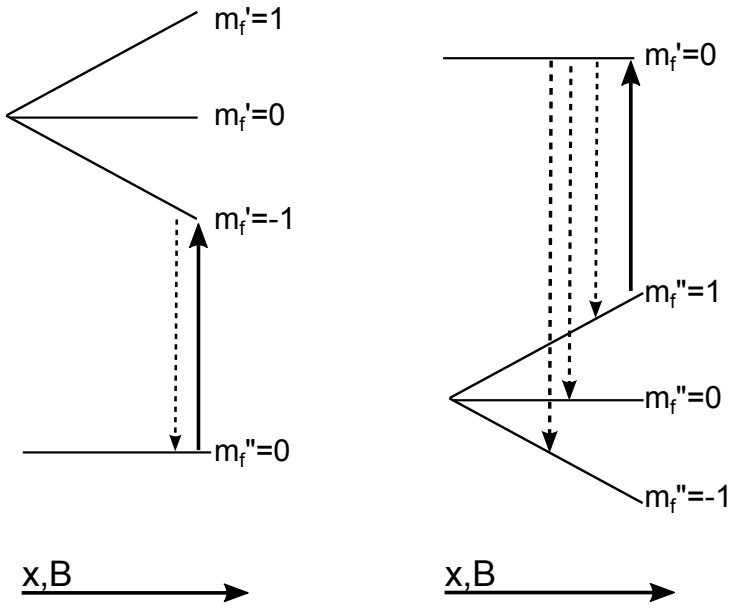

Figure 7.2: MOT types are described based on whether the trapping transition is from a lower F'' to a higher F' (type I, left) or a higher F'' to a lower F' (type II, right).

In order to avoid pumping light into these polarization dark states from which they are either unaddressable or only addressable by the wrong laser beam, we choose to rapidly switch the polarization of our MOT beams with a fast voltage-variable waveplate, or Pockels cell. Of course, if we do only that, we find that we are switching between a trapping configuration of the MOT and a fully anti-trapping one. To resolve this, we simultaneously switch the magnetic field gradient with the in-vacuum magnetic field coils discussed in Chapter 6, allowing for resolving the polarization dark states while always maintaining a trapping configuration. This means that we have a certain phase ambiguity that must be determine in the experiment in the relative drive between the switching signal that goes to the Pockel's cell and the AC magnetic field that is applied, as shown in Figure 7.3. While the appropriate delay is theoretically determinable to within 180 degrees in advance, because of cable length and electrical delays, we find it more straightforward to determine the appropriate phase offset experimentally.

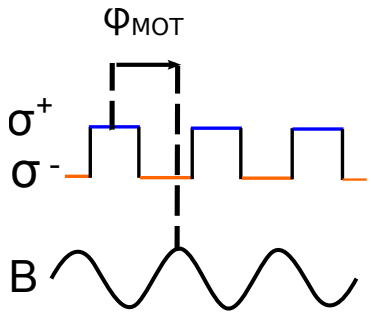

Figure 7.3: Phase for the Type II MOT operation refers to the delay between the polarization switching of the MOT beams and the magnetic field oscillation of the MOT coils.

Our group previously implemented a MOT in one and two dimensions utilizing a baseball coil allowing for a 2D quadrupole magnetic field spanning about 10 cm, which resonated at 2 MHz. This allowed us to demonstrate Doppler cooling and MOT action in the directions transverse to the molecular beam [21]. This gave us the knowledge that the type II MOT was suitable for use in our molecule, and gave confidence when moving towards the 3D implementation described here.

7.3 1D MOT reconfirmation

In an alternative method to our group's one and two-dimensional MOT implementations with a baseball field coil [21], we can use the anti-Helmholtz 3D magnetic field coils and apply only the MOT laser beam in the axial (perpendicular to molecular beam) direction. This allowed for optimization of the correct phase offset between the field coils and the polarization chopping in our current system, with a larger signal than initially achieved when searching for our 3D MOT, as shown in Figure 7.4. The phase offset for the 1D MOT is of course the same one that optimizes the 3D MOT.

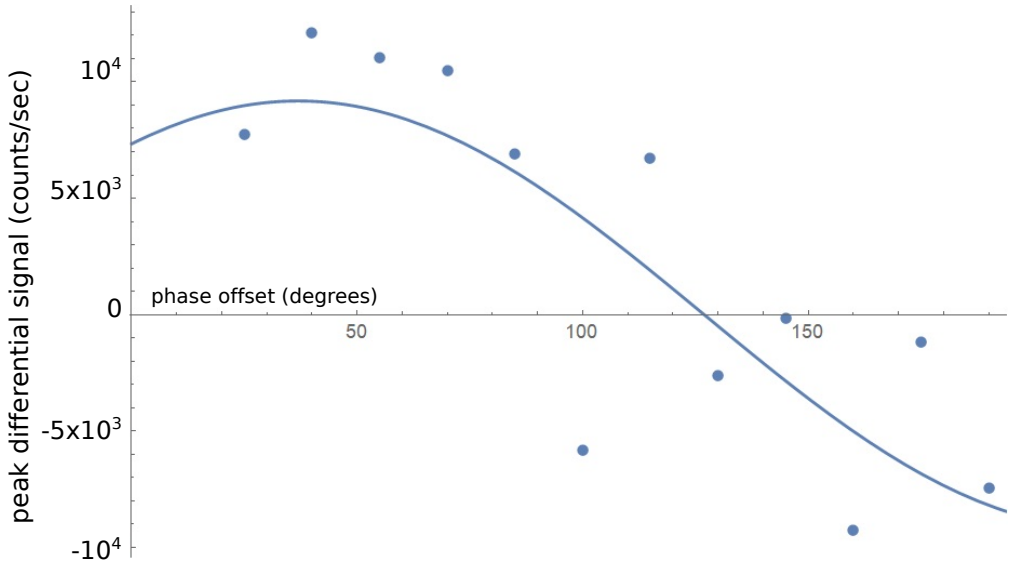

Figure 7.4: Differential signal (in phase minus 180 degrees out of phase) peak 1D MOT signal. Horizontal axis is the DDS supplied offset phase between the MOT coil drive and the Pockels cell drive.

When operating at the optimal phase, we observe the molecular beam as it is compressed or anticompressed into the field of view of the PMT, as shown in Figure 7.5. The 1D MOT signal size is approximately 1 percent of the unperturbed signal. While this 1D MOT implementation is not a step forward scientifically, as we had demonstrated the 1D MOT previously, it confirmed that our 3D MOT coils were working and gave us confidence while working on trapping of the molecular beam. We do not consider it surprising that the 1D MOT effect is assymetric with regards to detuning, as we have previously noted that the detuning dependence is quite complicated due to the closely spaced hyperfine levels in YO [21].

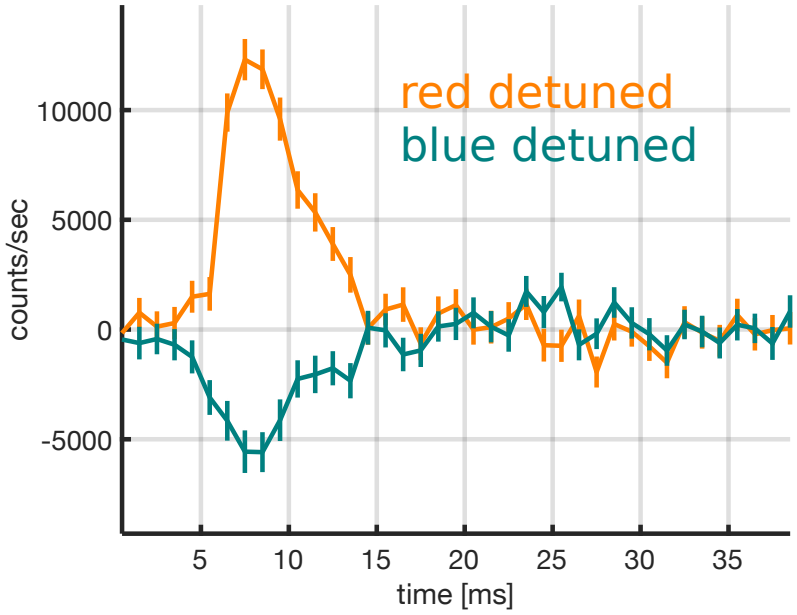

Figure 7.5: Differential (in phase minus out of phase) signal of 1D MOT operation on unslowed beam, for red detuning and blue detuning of all hyperfine components by 5 MHz.

7.4 3D MOT

The timing sequence used to load the MOT is shown in Figure 7.6. A slowing sequence is performed that creates a large flux of 5 m/s molecules, and then the slowing beam is held on for a longer period of time. As will be mentioned later on in the chapter, this allows molecules to be slowed to ∼0 m/s. Since the frequency is no longer chirped during this last 12 ms, the slowing lasers remain relatively far detuned from at rest molecules (32 MHz) and so only weakly interact with the molecules during this time. The in-vacuum shutter shuts after the molecules pass, in order to prevent line-of-sight helium collisions from the cell (the buffer gas flow is continuous) and to prevent heating of the buffer gas cell due to the various lasers in the slowing beam.

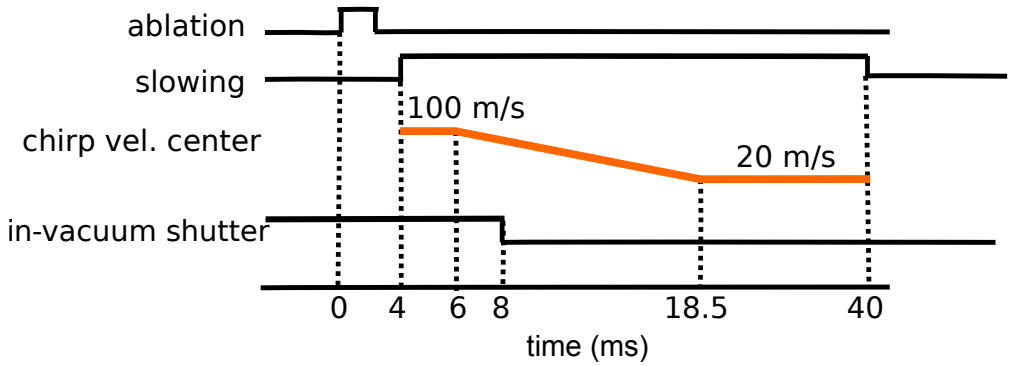

Figure 7.6: timing diagram used for loading MOT

The signal obtained from loading the MOT is shown in Figure 7.7. In order to improve clarity and prevent confusion due to slow but untrapped molecules transiting the detection region, the MOT data is shown as a correct phase signal minus a 180 degrees out of phase signal.

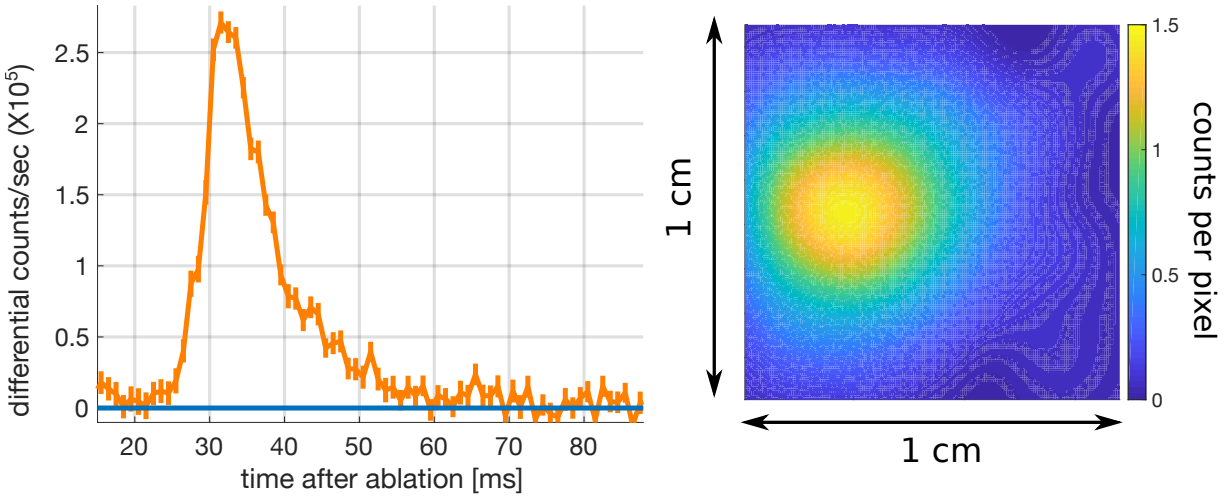

Figure 7.7: Differential (in phase minus out of phase) detection of MOT loaded at 20 G/cm RMS magnetic field gradient via PMT (left) or CCD (right). The CCD is exposed from 30 to 50 ms after ablation fire, and processed with a Gaussian smoothing function with sigma = 1 mm.

We estimate that the photon scattering rate of moleules in the MOT by assuming a saturation parameter of 1 and our known detuning. This yields an estimated photon scattering rate of 650×10^3 per second. We plan to measure the scattering rate in the near future, but this estimate and the

imaging system efficiencies discussed in Chapter 5 indicate that our peak molecule number loaded in the MOT is ∼2000 molecules. As mentioned in Chapter 5, this is a conservative estimate assuming that there are no inefficiencies in collection of photons within our lens' solid angle.

We have also implemented optical repumping of N''=3 via the $J' = 5/2$ level of the $A^2\Pi_{3/2}$, which can then decay only back to N''=1 to rejoin the cycling transition or directly back to N''=3 due to angular momentum selection rules. We put this laser component (with an applied 770 MHz splitting) in the slowing beam and then kept it on during the MOT. Its effect on the MOT signal is shown in Figure 7.8. We see that the total signal is increased by about 30 percent, but with no significant effect on lifetime. We believe then that this repump is not so much plugging a large leak channel, but rather incorporating molecules that exited the buffer gas cell in the N''=3 state and bringing them into the main cycling transition.

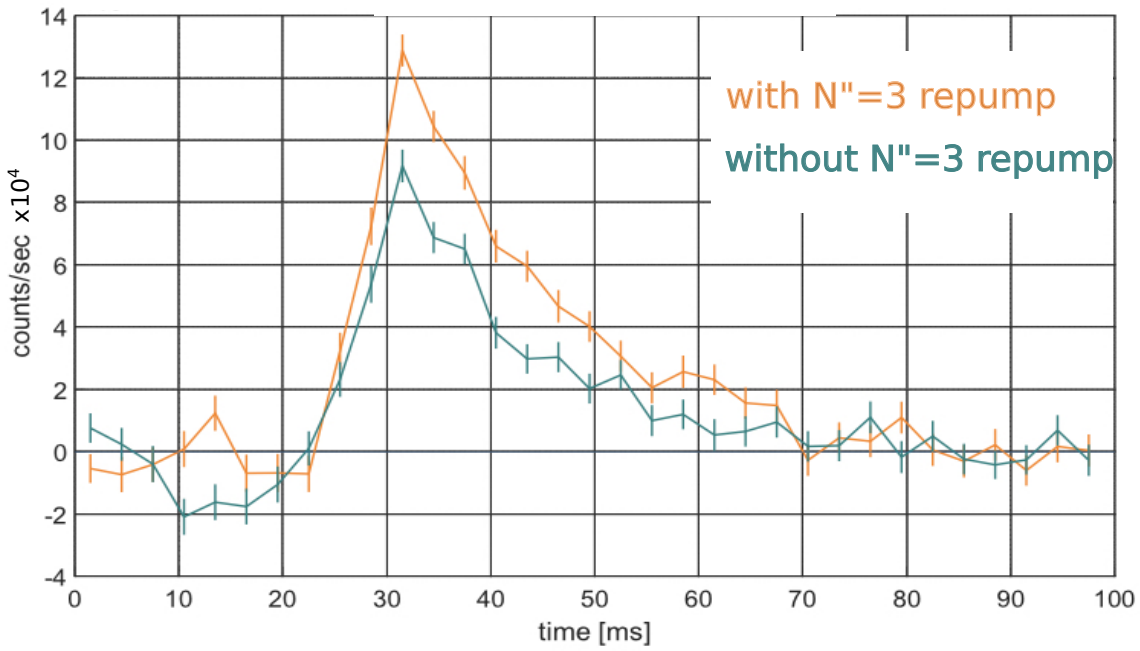

Figure 7.8: Differential (in phase-out of phase) PMT trace of MOT signal when using N''=3 optical repump in slowing (orange trace) and MOT or when not (green trace).

7.5 Characterization

We can vary the detuning of the cooling lasers in the MOT beams and observe the effect on the MOT, as shown in Figure 7.9. All traces use the same slowing sequence and magnetic field gradient of 20 G/cm RMS. Under these circumstances, we find that the best loading occurs for 9 MHz red detuning of all hyperfine sideband of the v''=0, N''=1 laser from their respective resonance. We have not yet experimented substantially with controlling the detuning of the different hyperfine components seperately from each other. We note that the range of detunings over which some MOT effect is visible is actually fairly large, greater than 20 MHz. Blue detunings do not allow loading of the MOT, however.

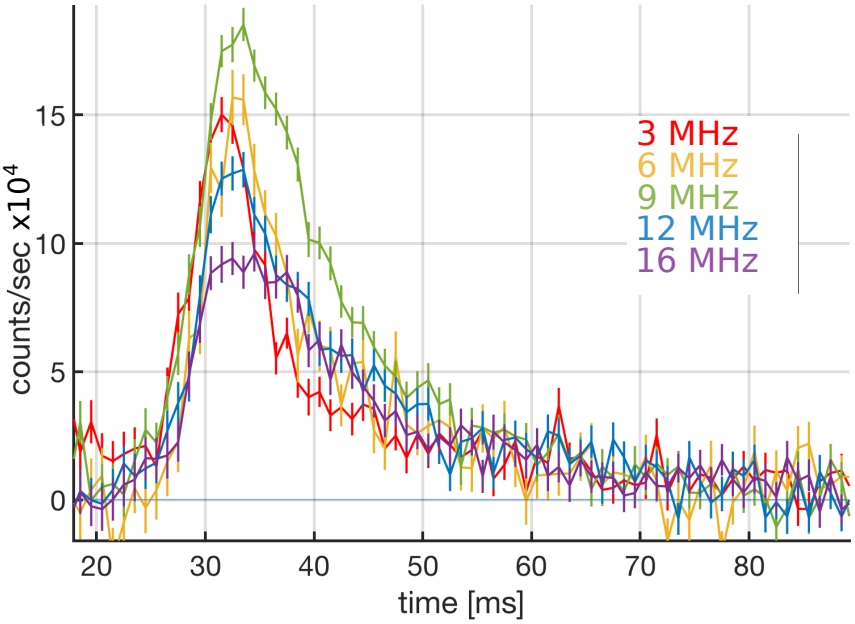

Figure 7.9: Dependence on the main cooling-laser components' detuning for the MOT operating with 20 G/cm field gradient. Maximal loading is found at 9 MHz red detuning of all hyperfine components in the laser addressing the v"=0, N"=1 level.

By varying the magnetic field gradient applied to the trapping coils, we find different efficiencies of loading of the MOT, though not a clear change in trap lifetime. A comparison of the differential (in phase - out of phase) MOT signal observed by the PMT at these varying RMS magnetic field gradients is shown in Figure 7.10. This comparison was taken with a MOT laser red-detuning of 6.2 MHz for all hyperfine components, and 25 mW of v''=0 laser light per MOT beam. Here we can see that the number loaded into the MOT improves for RMS field gradients up to about 18.5 G/cm, after which the improvement levels off.

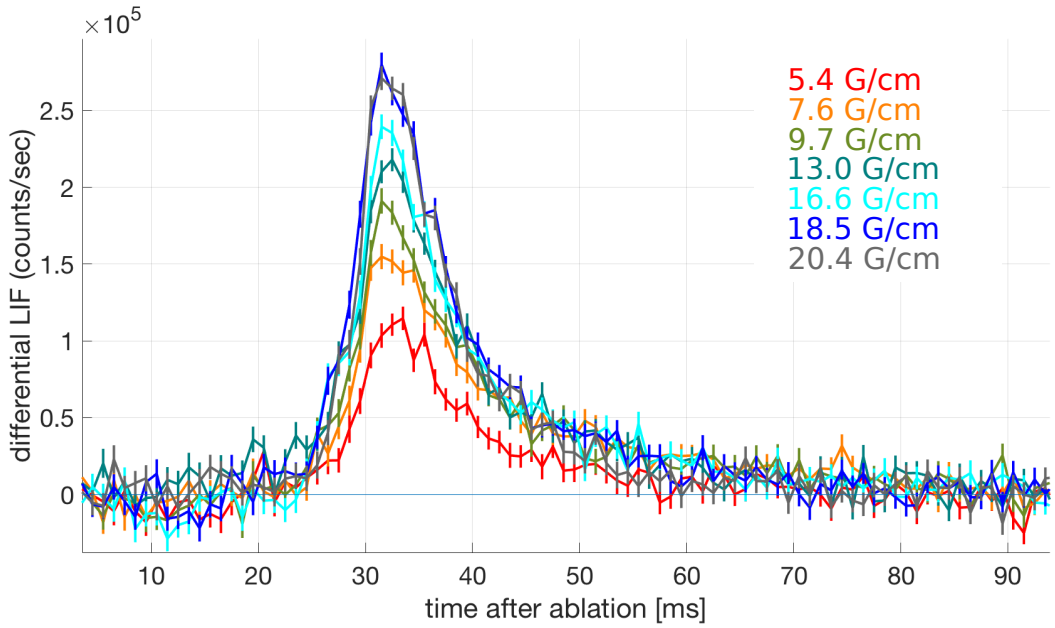

Figure 7.10: Differential LIF of MOT signal using the same slowing sequence but with varying magnetic field gradients.

Similarly, we can observe the spatial distribution of the molecules in the MOT for these different field gradients as well, as shown in Figure 7.11. These images were taken with the CCD exposing from 30 to 50 ms after the ablation fire.

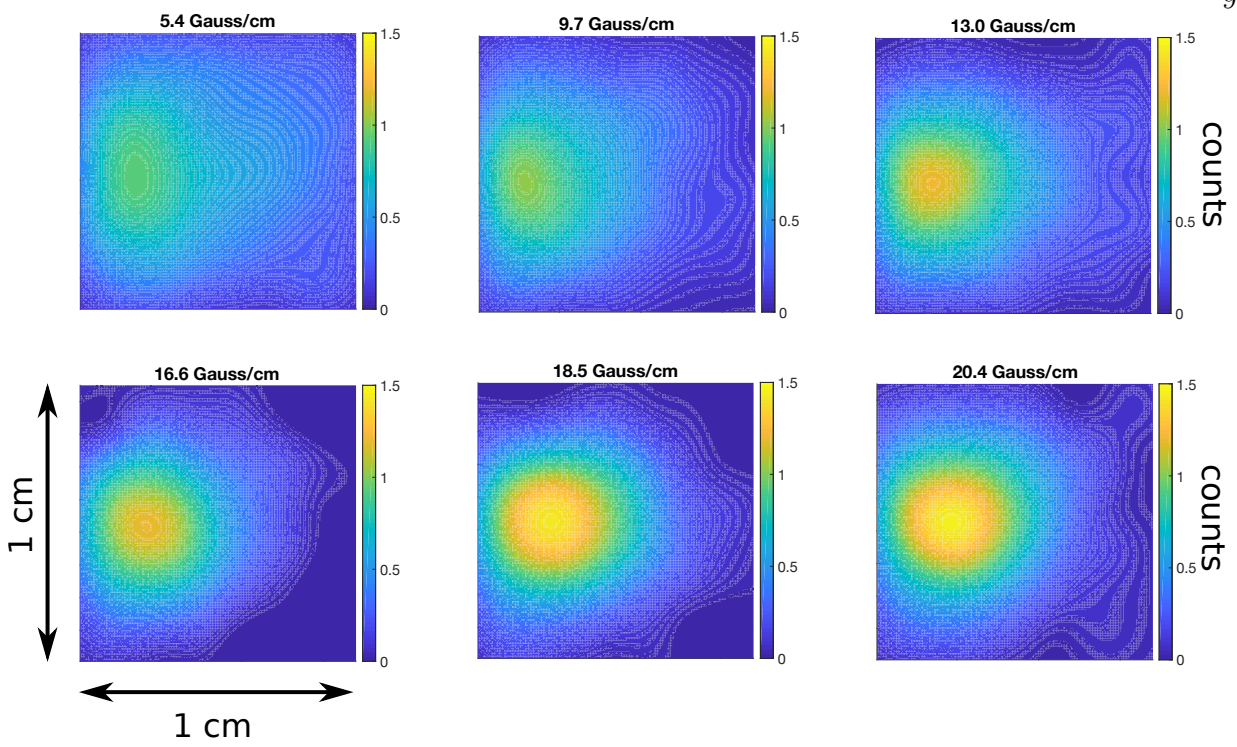

Figure 7.11: Differential LIF of MOT signal using the same slowing sequence (timing, detuning of slowing beams) and same mot beam detuning for each but with varying magnetic field gradients. Images are smoothed with a gaussian filter with sigma = 1 mm. Color scales are the same between images, with units of photon counts registered by the CCD. Each image represents 80 experimental cycles of averaging, 40 at the correct phase and 40 out of phase which are then subtracted. The vertical axis is the axial direction of the trap.

While some compression is visibly by eye from the CCD images, we can also be more quantitative. By performing a gaussian fit to the unsmoothed data, we determine the size in the radial (left/right) and axial (up/down) dimensions of the trap, as shown in Figure 7.12. We can see that the ratio between the radial and axial size is approximately a factor of two as expected for field gradients less than 10 G/cm, but oddly for higher gradients the ratio settles to a ratio of approximately 1.2. The fitted trap size does not get smaller for field gradients above 12 G/cm, though as noted previously the total number loaded is still larger for higher field gradients. We also find that the overall size is quite high, suggesting that we are suffering from heating of some kind.

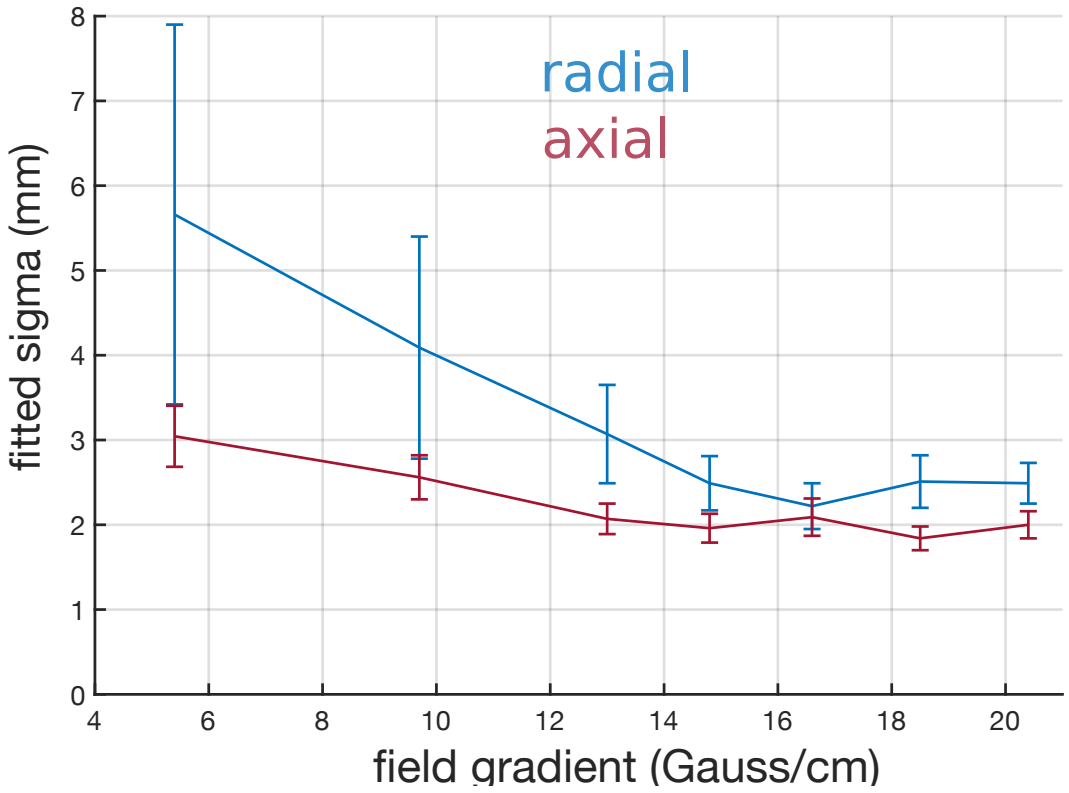

Figure 7.12: Fitted gaussian standard deviations vs applied magnetic field gradient in the MOT for both radial (blue) and axial (red) dimensions. Error bars indicate 95 percent confidence interval of fit.

Before we tried increasing the magnetic field gradient above 13 G/cm, we did attempt a preliminary temperature measurement at 13 G/cm via release and reimage as shown in Figure 7.13. By plotting the expansion time squared and the width squared of the reimaged trap against each other, we are able to extract a temperature of 11 mK (0–33 mK), which is indeed quite high compared to the temperature we would expect of $\sim$1 mK. We will revisit the temperature measurement after implementing some further changes to the trap.

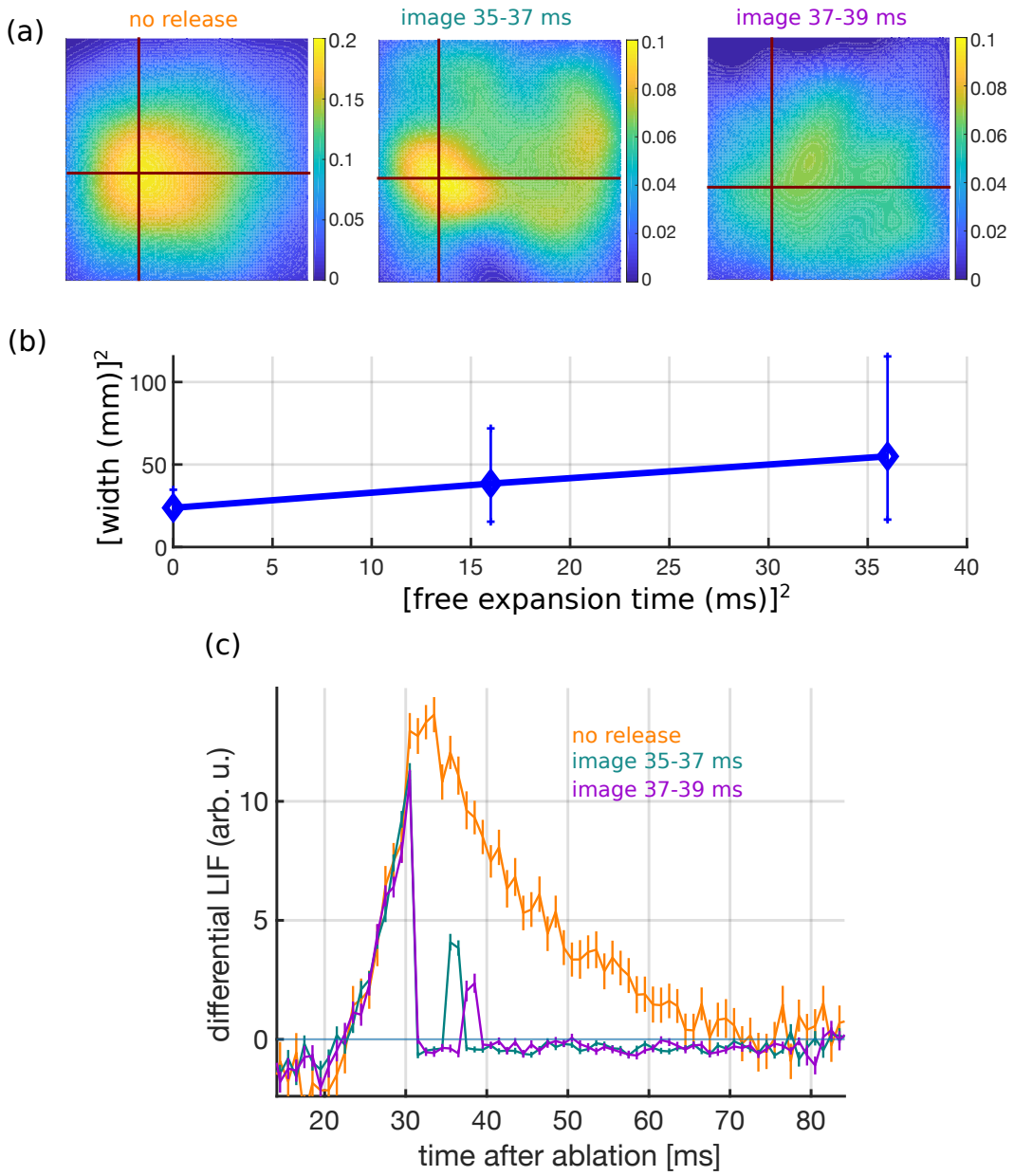

Figure 7.13: MOT temperature characterization: Imaging the MOT cloud after some period of free expansion (a) and then measuring the gaussian width of the cloud in the axial direction of the molecular cloud after allowing some amount of time of free flight, the temperature of the cloud can be extracted (b). The CCD exposure time is 2 ms for each image. Color scale (total counts registered per pixel on the CCD) of the expanded clouds is scaled up by a factor of 2 for greater visibility. Error bars represent 95 percent confidence interval of the gaussian fits. (c) Depicts the LIF recorded by the PMT for the same scenarios in (a).

At this time, there are a number of things that could be contributing to heating of the molecules. The first is that we are possibly switching the magnetic fields and polarization of the MOT too quickly, such that the (unavoidable) sidebands from the Pockels cell are heating some hyperfine components while cooling others, due to the small (14 MHz) zero-field hyperfine splitting within the G''=1 manifold. In order to bring the sidebands further in (while still switching rapidly enough to avoid polarization dark states) we are currently adapting the coils to have better heat sinking and lower resonance frequency, perhaps around 1.5-2 MHz. During the adaptation, we will also increase the inner radius of the magnetic field coils and the spacing between coils in order to further reduce scattering of laser light in the chamber. Another possible source of heating is if the resistances of the two different halves of the MOT coil are slightly different, then the magnetic field zero (trap center) will be switching back and forth between two different positions at the rate of the coil switching. With our current electrical configuration this uncertainty is unavoidable, but in the future the two coil halves could be driven by two different phase locked sources and the current going into each can be confirmed to be equal, preventing any heating from the oscillation of the magnetic field zero.

From the temperature and the initial size of the MOT before expansion, we can also estimate the trapping frequency. Using the equipartition theorem in only the axial direction, we achieve an estimate of 30 Hz, which while not fast is within a factor of 2 of that realized by the Doyle group at Harvard for their initial implementation of a CaF RF MOT [24], though clearly the error bars on our data need to be improved before any firm conclusions may be drawn.

7.6 Intensity dependence

While endeavouring to load more molecules into our MOT, we found an interesting interrelation between the power of the main cooling beams and the lifetime of the MOT. These results are shown in Figure 7.14.

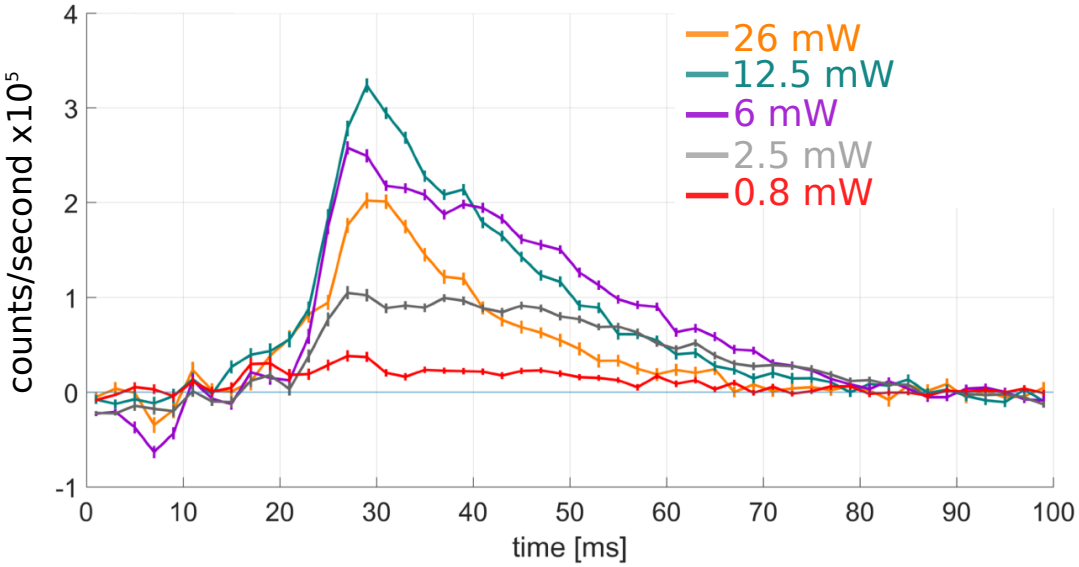

Figure 7.14: Using different powers for the main cooling transition in the MOT beams changes the number of molecules loaded but also affects the lifetime of the MOT. Powers stated are powers per MOT beam for N'' =1, v'' =0 light.

Not only is there a optimum power for loading of ∼12.5 mW per beam, we can also quantify the effect of the MOT beam power on the lifetime. We perform this characterization by fitting the MOT signal after 30 ms to an exponential decay. The results of these fits are outlined in Table 7.1.

Table 7.1: Fitted MOT lifetime for different MOT beam main cooling laser powers per beam

Power (mW)	Lifetime (ms)	95% fit confidence interval (ms)
26	11.1	9.3-13.6
12.5	12.3	11.4-13.4
6	14.9	13.9-16.0
2.5	17.8	16.2-19.8
0.8	13.8	10.8-18.8

The general trend of increased lifetime with lower MOT beam power may be providing a clue as to the short lifetime of our MOT. It suggests that the lifetime is dependent on the photon scattering rate. This would normally suggest a leak to a dark state, though we have already investigated the possibility of loss into N'' =3 and v'' =3, and believe that they are not the limiting factor. Additionally, we hypothesize that the lower MOT beam powers may be yielding a lower temperature of the trap, which we plan to investigate experimentally in the near future. Because the loaded molecule signal is highest for 12.5 mW per beam, we usually operate at that power for other characterizations in order to reduce data acquisition time.

7.7 Overslowing for loading the MOT

While working on optimizing the MOT signal, we found that the slowing sequence which maximizes the flux of molecules at 5 m/s is not in fact the one that maximizes loading of molecules into the MOT, despite our initial expectation that trappable velocities should be ± 5-10 m/s. In fact, adding 12 ms of slowing light without frequency chirping to the end of the optimal 5 m/s slowing timing sequence is the best sequence we have found for MOT loading. In order to better understand this, we performed a low powered Doppler sensitive detection of the molecules after various slowing sequences, as shown in Figure 7.15. This measurement occurs for 10 ms after the end of the slowing, and represents the average counts/sec for different velocities within this time interval.

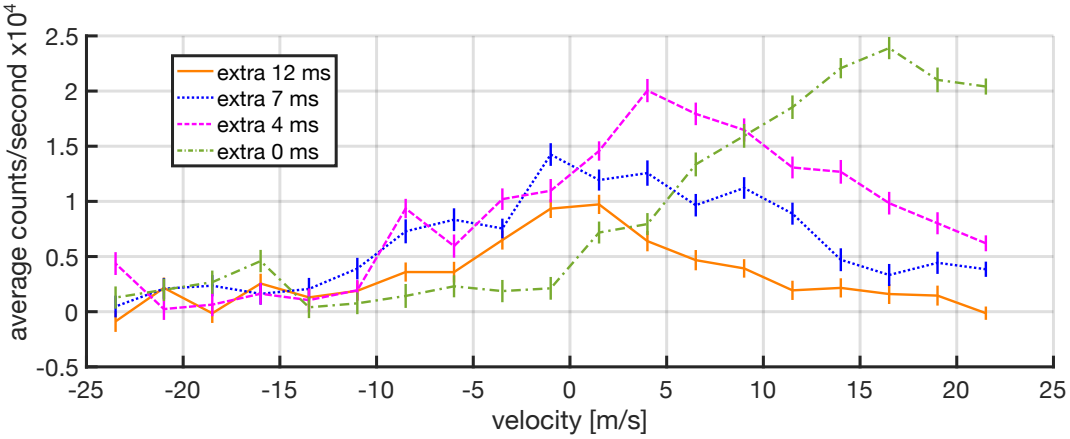

Figure 7.15: Different amounts of slowing time and their effect on the slowed molecule distribution. The sequence used for 5 m/s slowing is typically 0 extra added time (green), while we find maximal MOT loading for the +12 ms (orange) slowing sequence.

Ideally we would have a large flux of molecules slowed to zero velocity at the center of the trap when the slowing shuts off, so it is sensible that the largest MOT signal comes from a slowing sequence that yields molecules at rest in the MOT region at the shut-off of slowing. It is however somewhat surprising that the 5 m/s slowing sequence plus an extra 10 ms wasn't even better for MOT loading as the molecular distribution is seemingly higher for all slow velocities for an extra 7 ms of slowing than for an extra 12 ms. We are still working to improve our understanding of the efficacy of this timing sequence for loading molecules into the MOT.

While there are clearly improvements to be made to our MOT, we also feel that current number and lifetime are sufficient to make forward progress. The next step on the horizon experimentally is implementing further cooling on the narrow-line transition in our molecule. Narrow-line cooling will yield colder temperatures and is in some ways experimentally more straightforward to implement, as will be discussed in Chapter 8.

Chapter 8

690 nm Narrow-line transition: prospects for secondary cooling

8.1 Spectroscopy of the $A'^2\Delta_{3/2}$ state

In order to characterize the properties of a second stage red MOT on the $X^2\Sigma$ to $A'^2\Delta_{3/2}$ transition, we first need an estimate of the linewidth of the transition. We acquire this estimate by comparing the absorption strength of the red transition to that of the known orange transition. To that end, we have identified the N"=0,1,2:G"=1 to $A'^2\Delta_{3/2}$ transitions using absorption spectroscopy in our cryogenic buffer gas cell, as shown in Table 8.1, in agreement with previous work [61].

Table 8.1: Identification of $X^2\Sigma$ to $A'^2\Delta_{3/2}$ transitions

Transition	Frequency (THz)
N"=0, G"=1 $\rightarrow A'^2\Delta_{3/2}$(-)	434.70310
N"=1, G"=1 $\rightarrow A'^2\Delta_{3/2}$(+)	434.67989
N"=2, G"=1 $\rightarrow A'^2\Delta_{3/2}$(-)	434.63333

The energy splitting between N"=0$\rightarrow A'^2\Delta_{3/2}$ and N"=2 $\rightarrow A'^2\Delta_{3/2}$ is $N"(N"+1)B$, with $N" = 2$, where B is the rotational constant for the $X^2\Sigma$ state. Evaluating this yields $B = 11.6$ GHz, which agrees with the known rotational splitting [44]. By comparison of the absorption on the N"=1 $\rightarrow A'^2\Delta_{3/2}$ transition with the N"=1 $\rightarrow A^2\Pi_{1/2}$ transition and the known lifetime of the $A^2\Pi_{1/2}$ being 33 ns [62], we estimate that the lifetime of the $A'^2\Delta_{3/2}$ state is τ =425 ns. We

note that the N" = 0,2 to $A'^2\Delta_{3/2}$ transitions address a different parity level than the N"=1 to $A'^2\Delta_{3/2}$ transition, but we do not find a different value of B, indicating that the parity splitting of the $A'^2\Delta_{3/2}$ state is smaller than the Doppler broadened linewidth of ∼60 MHz inside the cell.

8.2 Mixing of the $A'^2\Delta_{3/2}$ and $A^2\Pi$ states

In addition to performing an absorption measurement, we also calculate a lifetime estimate. While electric dipole forbidden, the decay from the $A'^2\Delta_{3/2}$ state is almost entirely due to mixing with the $A^2\Pi_{3/2}$ state, on the order of 3.5% [44]. The molecular potential can be approximated using the Rydberg-Klein-Rees (RKR) [63] method for the states of interest. The curves for the $X^2\Sigma$ and $A^2\Pi$ states can be corroborated with previous work [64]. After using a finite difference method to determine the wavefunctions to evaluate the vibrational overlap integrals and the $\langle v|\, 1/r^2\, |v'\rangle$ integrals we use the procedure outlined by Chalek and Gole [44] to compose the Hamiltonian including the electronic, rotational, vibrational, spin orbit, and coriolis operators. By diagonalizing this Hamiltonian for J=3/2, we express the $A'^2\Delta_{3/2}$ eigenstate in terms of the Born-Oppenheimer states, the first few terms of which are:

$$\left|\Psi_{\Delta_{3/2},v'=0}\right\rangle \approx 0.9865\left|\Delta_{3/2},v'=0\right\rangle - 0.1582\left|\Pi_{3/2},v'=0\right\rangle$$
$$-0.0369\left|\Pi_{3/2},v'=1\right\rangle + 0.0176\left|\Pi_{1/2},v'=0\right\rangle + ...$$

These coefficients squared indicate the mixing of the $A'^2\Delta_{3/2}$,v'=0 state with other states, with the largest being a 2.5% mixing with the $A^2\Pi_{3/2}$, v'=0 state. Summing over the various Born-Oppenheimer states and their associated Franck-Condon factors yields estimates for the vibrational branching ratios for the $A'^2\Delta_{3/2}$ to $X^2\Sigma$ transition. These and other state branching ratios are compiled in Table 8.2.

Table 8.2: Vibrational branching rates for various transitions of interest.

State 1	State 2	v_1	v_2	$q_{v_1 v_2}$	State 1	State 2	v_1	v_2	$q_{v_1 v_2}$
$A^2\Pi_{1/2}$	$X^2\Sigma$	0	0	0.9924	$A^2\Pi_{1/2}$	$X^2\Sigma$	1	0	0.0076
$A^2\Pi_{1/2}$	$X^2\Sigma$	0	1	0.0074	$A^2\Pi_{1/2}$	$X^2\Sigma$	1	1	0.9752
$A^2\Pi_{1/2}$	$X^2\Sigma$	0	2	2.4×10^{-4}	$A^2\Pi_{1/2}$	$X^2\Sigma$	1	2	0.0164
$A^2\Pi_{1/2}$	$X^2\Sigma$	0	3	2×10^{-6}	$A^2\Pi_{1/2}$	$X^2\Sigma$	1	3	7.8×10^{-4}
$A^2\Pi_{3/2}$	$A'^2\Delta_{3/2}$	0	0	0.9078	$A'^2\Delta_{3/2}$	$X^2\Sigma$	0	0	0.9422
$A^2\Pi_{3/2}$	$A'^2\Delta_{3/2}$	0	1	0.0860	$A'^2\Delta_{3/2}$	$X^2\Sigma$	0	1	0.0568
$A^2\Pi_{3/2}$	$A'^2\Delta_{3/2}$	0	2	0.0059	$A'^2\Delta_{3/2}$	$X^2\Sigma$	0	2	0.0011
$A^2\Pi_{3/2}$	$A'^2\Delta_{3/2}$	0	3	3.3×10^{-4}	$A'^2\Delta_{3/2}$	$X^2\Sigma$	0	3	$<10^{-4}$

Using 2.5% mixing and the known ∼30 ns lifetime of the $A^2\Pi_{3/2}$ state [62], we estimate the lifetime of the $A'^2\Delta_{3/2}$ state as 1200 ns. These two estimates of the lifetime of the $A'^2\Delta_{3/2}$ state, 425 ns from the absorption measurement and 120 ns from calculation are of similar order and give us a starting point for further calculations. From here on, we use an intermediate estimate of τ= 1 μs, yielding a linewidth of $\gamma = 2\pi\times160$ kHz.

8.3 Narrow-line cooling on the $X^2\Sigma$ to $A'^2\Delta_{3/2}$ transition

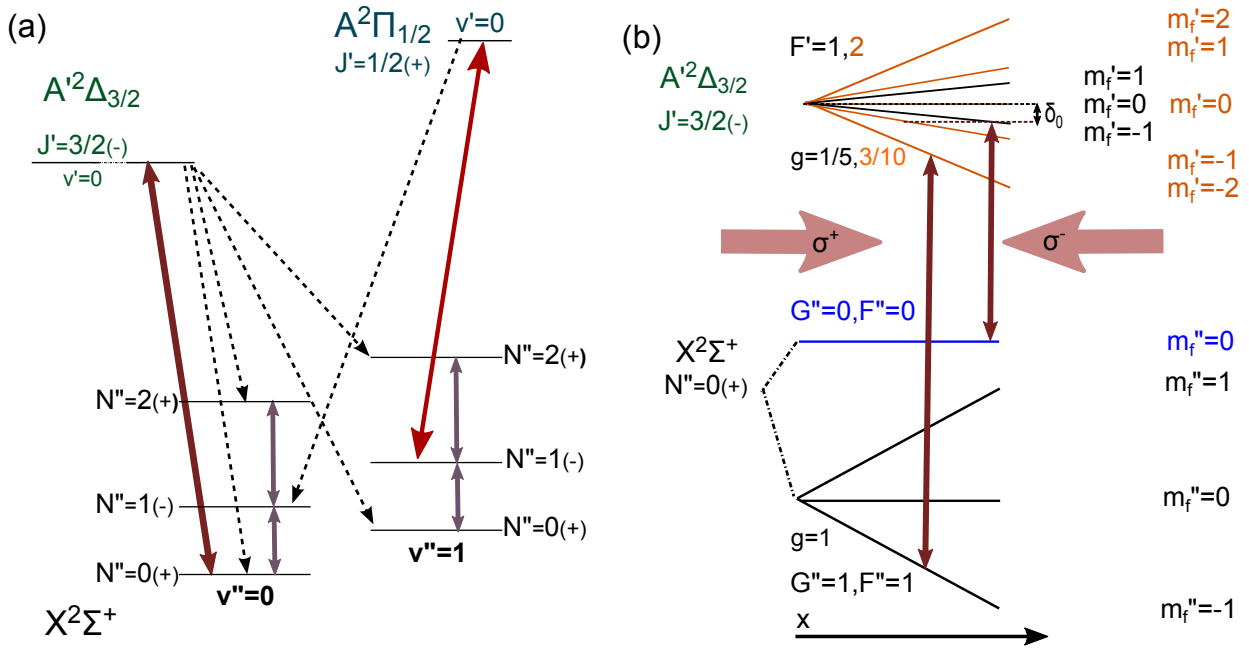

Figure 8.1: Level structure for the narrow-line MOT. (a) Maroon arrow indicates the transition used in the red MOT. Gray lines indicate microwave mixing which closes rotational branching. Red line indicates v"=1 repump, the same as used in the orange MOT. (b) Zeeman structure and MOT scheme. g represents the corresponding magnetic Landé factor. Large arrows indicate counter propagating circularly polarized laser beams. Both F"=0 $\rightarrow$ F'=1 and F"=1$\rightarrow F'$=2 transitions can effect a MOT action (maroon arrows).

Once molecules have been cooled with the orange MOT, we wish to further cool them utilizing the narrow $X^2\Sigma$ to $A'^2\Delta_{3/2}$ transition. This is acheivable by exciting from the N" = 0 level to the $A'^2\Delta_{3/2}$, J'=3/2 level, as in Figure 8.1(a). Decays from $A'^2\Delta_{3/2}$ can be to either N"=0 or 2. To maintain cycling, we use microwave mixing to address the v"=0, N"=0$\leftrightarrow$1, and N"=1$\leftrightarrow$2 rotational transitions, with frequencies $2B_0$ and $4B_0$, where B_0 is the rotational constant for the v"=0 level. Similarly, higher vibrational levels can be mixed by applying microwaves resonant with the N"=0$\leftrightarrow$1 and N"=1$\leftrightarrow$2 rotational transitions of that vibrational level, e.g. at $2B_1$ and

$4B_1$ for v"=1. Additionally, this microwave mixing scheme allows v">0 vibrational levels to be repumped with the same lasers used in the orange MOT. The rotational constants for the first few vibrational levels have been determined and so mixing will be straightforward to implement [65, 66]. The saturation intensity required $I_{sat} = (\pi hc)/(3\lambda^3\tau)$, is 60 μW/cm^2, an intensity obtainable with commercially available diodes.

In addition to the possibility of an optical molasses based on this transition, it is apparent that a narrow-line MOT is also achievable. While a MOT can be made using any or all F" states due to a non-zero g-factor for both the ground and excited states, the number of frequency components and polarization considerations go up considerably with the number of states [48]. The simplest possible MOT action in this system is that for the transition from the N"=0 level to the $A'^2\Delta_{3/2}$ state. The N"=0 level has G values 0 and 1, split by ~760 MHz. A type-I MOT can be performed on both sublevels, from G"=F"=1 to F'=2 and from G"=F"=0 to F'=1, as depicted in Figure 8.1(b). Additionally, since in type-I MOTs no Zeeman dark states can form, experimental implementation is simplified because it will not be necessary to perform the magnetic field switching and polarization chopping used in the orange MOT.

8.4 Narrow-line MOT simulation

We simulate the red MOT in one dimension with counter-propagating circularly polarized light with components addressing both the N"=0, G"=0 and G"=1 manifolds and exciting to available $A'^2\Delta_{3/2}$ states. Initial conditions are given by a 1 mK distribution using the parameters of an orange MOT with a trap oscillation frequency of $\omega_{MOT} = 2\pi\times155$ Hz [21]. Because the Doppler broadened linewidth at 1 mK is significantly greater than the narrow transition, we model the laser light with multiple frequency components spanning the broadened linewidth, each with saturation parameter s_0 [33, 35]. We use a carrier plus two pairs of sidebands spaced by $2\pi\times1$ MHz, with the detuning of the highest energy sideband from resonance labeled δ_1. Since microwave mixing and vibrational repumping are both fast compared to the optical cycling on this transition, we make the following assumptions about the population distribution in the ground state. Because

of the 760 MHz hyperfine splitting, G"=0 manifolds are only mixed with other G"=0 states, and G"=1 manifolds with other G"=1 states. So, population in a given G" manifold is weighted by the branching ratio from the $A'^2\Delta_{3/2}$ state, which is 1/4 and 3/4 into the G"=0 and 1 levels respectively. For a given G" level, the population is evenly distributed among all available v"=0, N"=0,1,2 states due to the microwave mixing. For a two level system, the force from a laser beam frequency component resulting in absorption and followed by spontaneous emission can be written as [67]

$$F = \frac{\hbar k s_0 \gamma/2}{1 + s_0 + (2\delta/\gamma)^2} \tag{8.1}$$

where k is the wavenumber, s_0 is the saturation parameter, δ the detuning experienced by the molecule, and $\gamma = 1/\tau$. In a MOT, δ can be written as $\delta = \delta_0 - kv + \mu' Ar/\hbar$, where δ_0 is the nominal detuning of the laser frequency component from resonance, v the velocity, A the magnetic field gradient, r the molecule's position, and μ' the differential magnetic moment for the transition. To compute the average force felt by an $N" = 0$ molecule, the force is averaged over the transitions available to all $N" = 0$ sublevels, and summed over both laser beams and all frequency components. Since we only optically address N"=0 which contains 1/9 of the microwave mixed states, the average force felt by a molecule mixed between N"=0,1,2 is $\bar{F}_{total}$=$\bar{F}_{N"=0}/9$. In addition, we simulate heating due to spontaneous emission by adding a random momentum kick when a photon is absorbed. For small detunings, the force reduces to $\bar{F}_{total} = -\beta v - \kappa r$, where β is the damping cofficient and κ the spring constant, which together characterize the trap.

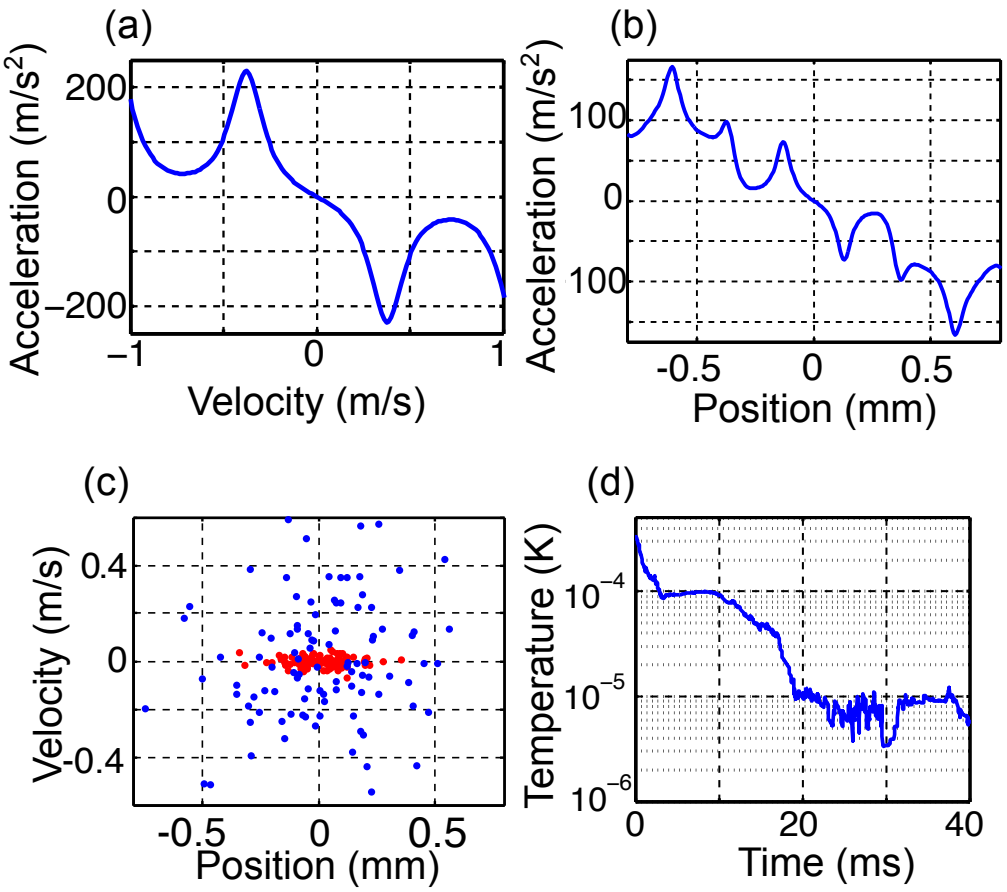

Figure 8.2: Results of simulation. (a) Velocity dependent force due to optical molasses. (b) Position dependent force due to magnetic field gradient for stationary molecules. (c) 1 mK distribution produced from orange MOT (blue) and distribution after red MOT has been on for 20 μs (red). (d) Temperature vs time after red MOT is turned on and the orange MOT is turned off. Oscillation of modeled temperature after 20 ms is an artifact of the limited number of molecules in the Monte Carlo simulation

We first model an optical molasses as shown in Figure 8.2(a) for the parameters δ_1 = -1.5γ and $s_0 = 3$, chosen to provide force to all moving molecules in an initial 1 mK distribution. From the slope, we can extract β and so the damping rate $\Gamma_D = 2\beta/m = 950$ Hz. Likewise, we extract κ from the rate of change of force with position for zero velocity molecules, as shown in Figure 8.2(b). Under the same parameters, and magnetic field gradient $A = 3$ G/cm, we find a MOT oscillation frequency $\omega_{MOT} = \sqrt{\kappa/m}$ of $2\pi\times33$ Hz. The characteristic trapping time is then $\Gamma_D/\omega_{MOT}^2 = 20$ ms

[67]. The simulation clearly shows phase space compression (Figure 8.2(c)), reaching a temperature of <10 μK at 20 ms, as shown in Figure 8.2(d). The simulation indicates a photon scatter rate $\sim 10^4$ per second, and cooling to <10 μK requires only ~200 photons. Naively extrapolating to three dimensions by dividing κ and β by three gives $\omega_{3D} = 2\pi \times 19$ Hz, Γ_{3D} =317 Hz, and requires ~600 photons to cool. We estimate the v" = 3 limited MOT lifetime to be >1 second. We note that for a molecule at rest, the maximum acceleration due to the three dimensional MOT is ~5 times that of gravity, allowing successful trapping. In sum, we find that the red MOT is capable of trapping and further cooling the molecules captured in an orange MOT, requiring only the addition of one 690 nm laser with frequency components 760 MHz apart to the current system, one for the G"=0 and the other for the G"=1 to $A'^2\Delta_{3/2}$ transition.

8.5 Conclusion

We have identified a transition in YO suitable for secondarily cooling a MOT on the $X^2\Sigma$ to $A^2\Pi_{1/2}$ transition by using a narrow-line transition from the $X^2\Sigma$ to $A'^2\Delta_{3/2}$ state. Two estimates indicate a lifetime of $\tau \approx 1$ μs for the $A'^2\Delta$ state, allowing a final temperature of ~10 μK. We have also determined that the vibrational branching from the $A'^2\Delta_{3/2}$ state is favorable enough to not necessitate any more vibrational repump lasers than the first stage MOT. Simulations indicate parameters for the red MOT of a damping rate of 317 Hz and a MOT frequency of $2\pi \times 19$ Hz.

There are a few other future experimental directions that we also find very exciting. Effective slowing has been shown in strontium by using chirped adiabatic stimulated emission slowing [68]. The method relies on using a sufficiently narrow transition such that stimulated emission can occur before spontaneous emission. The atoms are slowed by interacting with two laser beams, which have their frequency swept across resonance in such a way that the atoms absorb a photon from the counter-propagating beam and stimulatedly emit into the copropagating beam. This means that every absorption and emission cycle transfers $2\hbar$k of momentum from the atom. Additionally, because the mechanism involves stimulated emission, branching into undesired rotational or vibrational states is supressed. Because we have identified a narrow-line transition in our molecule, this

seems to be a viable course of action. The buffer gas cell would have to be modified to allow for a laser beam to copropagate with the molecules in the slowing region, but otherwise the experimental implementation would be relatively straightforward. In addition to slowing, the method can also be used to produce a robust narrow-line MOT, as in reference [69].

Another route that is promising is that of a gray or blue molasses, which has already been shown to produce sub-Doppler cooling in molecular MOTs, as in References [29, 30, 31]. These methods rely on first loading the MOT, then simultaneously blue detuning the trapping lasers. Because these MOTs are operating on a type II cooling transition, this allows for Sisyphus sub-Doppler cooling. This method has proven to be a robust way to laser cool molecules to the $\sim$50 μK level.

We also note that recently some more sophisticated theory calculations have been performed [70] using coupled-cluster methods. These calculations suggest that the level of mixing between the $A^2\Pi_{3/2}$ state and the $A'^2\Delta_{3/2}$ state is smaller than we'd expect, on the level of 0.1% rather than 2.5%. This lower level of mixing would indicate a significantly narrower linewidth of the $A'^2\Delta_{3/2}$ state. At this time we don't have an explanation for the lack of congruence between our experimental in-cell absorption estimate of the lifetime and these new calculated results. In the near future, we plan to more carefully measure the lifetime of the $X^2\Sigma \rightarrow A'^2\Delta_{3/2}$ transition in the molecular beam or in the MOT itself in order to constrain the linewidth further. The more accurate measurement will both be useful for us moving forward with the narrow-line cooling as well as to give further insight on the theoretical methods.

Appendix A

MOT coil layout and assembly

A.1 Coil design

Design of the coils is done using Mentor Graphics SSD PADS Layout. The program allows precise drawing of arcs and shapes where the copper is to be left, as well as various holes that need to be in place. PADS can convert to .dxf files which can be used on CNC machines to automate the cutting of the traces.

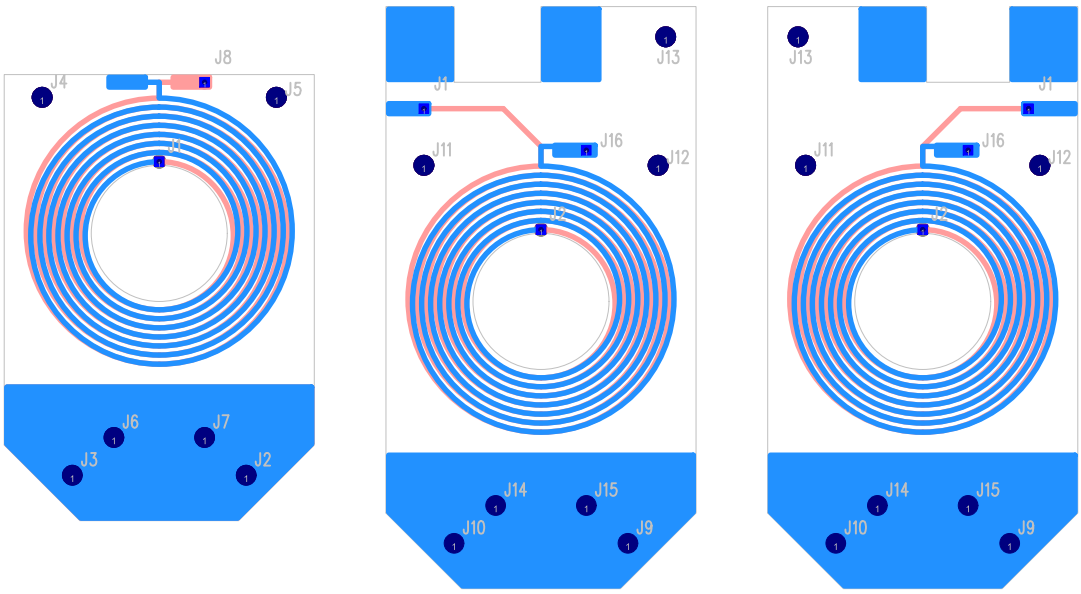

Figure A.1: PADS design for MOT coil boards.

In Figure A.1 are the schematics for the MOT coils, where blue (the 'top' trace) indicates the direction away from the MOT, and pink towards. Pink is not adjusted for flipping over the board, that is, the trace is correct as viewed from above, like the blue. For each separate half of the board, a little board will be outside of the larger inner board. The two inner boards are not identical to allow for a mounting bar to go between J13 of both. The drive connections for each board will be placed at the large and the small pads on the side, with the small pad being ground. The tuning capacitor will go between the two large pads, making the internal large pad the high voltage point on the board. This high voltage pad will be connected with a wire to the blue pad on the small board. Finally, the vias for the small board pink pad will connect to the blue pad on the large board vertically in line with them, that is J8 on the small board will connect to J16 on the big board. All larger vias are through holes used for mounting purposes. This new design allows for the two separate boards to be run in parallel, instead of in series as done previously. The symmetry should reduce the large electric field gradient between boards seen in the previous design.

A.2 Coil assembly

Assembly of the coils is somewhat tricky, first the two halves of the boards are partially assembled separately, there is a layer of indium, copper foil, and indium sandwiched between boards on a single side, where the heatlink will attach. Additionally, a layer of kapton film is between these boards as well across the non indium section to prevent shorting or arcing. The screws (2-56) not on the indium side have washers to hold the distance between boards at a millimeter. Then, the rectangular mating piece is attached via two 4-40 screws to the large L-shaped heatlink. The boards on the heatlink side are then connected through the c-clamp shaped pieces into the rectangular mating piece with 2-56 screws. The second set of boards are then attached to the c-clamp pieces (also with 2-56 screws), along with inserting the copper spacer on the non heatlink side between boards (attached via a 1-72 threaded rod). Finally, the whole construction is placed into the vacuum chamber, and the L shaped heat link is affixed to the feedthrough with two 8-32 screws. Each step must be done carefully and tightly to assure a good fit, as all heat transfer is done through direct

contact. I have not yet found a vacuum safe thermal grease that is sufficiently vacuum compatible even at temperatures above 50 degrees C. Apiezon H has a vapor pressure of $\sim 5 \times 10^{-8}$ Torr at 50 degrees C, and rises quickly to 1×10^{-6} Torr at 90 degrees C. It is possible that in the future we may find this acceptable. The capacitors used for setting the frequency of the MOT coils are from American Technical Ceramics, with part number 800E470GMN7200X for the 47 pF version. They are specified to have low equivalent series resistance, high Q, and can handle a voltage of 7.2 kV. Because of the resonant voltage enhancement in a LC tank circuit, we estimate we have approximately 1.5 kV peak voltage across the capacitor, necessitating a high voltage rated capacitor for this purpose.

Appendix B

Frequency calculation and locking for slowing and trapping

B.1 Introduction

In order to achieve the correct scanning frequencies during slowing as well as maintaining the appropriate stable frequencies during trapping, some care must be taken to the configuration of the lasers and their locks to the comb. While in the past when doing only slowing, we changed frep during the slowing and so moved all of the lasers along with the comb. Now however, as we require stable versions of all transitions, I have implemented the locking in such a way that the comb and all the master lasers (excepting the 1228 nm diode laser for doubling and slowing) can remain stationary.

The following are the lasers that we need to stabilize: the vibrational repump master lasers (1 and 2), the 1228 nm diode laser (for slowing) and the Toptica laser (for the MOT beams), and eventually a 690 nm diode laser for our narrow line cooling transition.

The resonance frequencies for our transitions of interest are here tabulated for the G"=0 hyperfine component:

Label	Transition	Frequency (MHz)
Main Cooling Transition	$X^2\Sigma$, v"=0, N"=1 $\rightarrow$ $A^2\Pi_{1/2}$, v=0, J=1/2	488492552.6
v=1 Repump	$X^2\Sigma$, v"=1, N"=1 $\rightarrow$ $A^2\Pi_{1/2}$, v=0, J=1/2	462837939.0
v=2 Repump	$X^2\Sigma$, v"=2, N"=1 $\rightarrow$ $A^2\Pi_{1/2}$, v=1, J=1/2	461735964.9
Narrow Line Transition	$X^2\Sigma$, v"=0, N"=0 $\rightarrow$ $A'^2\Delta_{3/2}$, v=0, J=3/2	434703100 (30)

A more detailed explanation of the locking scheme for each laser follows, but in summary the final frequencies of the lasers when locked to the comb are:

$$Raman = 2 * (f_{co} + n_0 * f_{rep} - beat_{raman} + 2 * offsetAOM_{raman}) \tag{B.1}$$

$$Toptica = Raman + VCO_{dye} - beat_{toptica} \tag{B.2}$$

$$v1 = f_{co} + n_1 * f_{rep} - beat_1 + offsetAOM_1 \tag{B.3}$$

$$v2 = f_{co} + n_2 * f_{rep} - beat_2 + offsetAOM_2 \tag{B.4}$$

Then the final frequencies as they enter the vacuum chamber for the slowing beam are:

$$Slowing_0 = Raman + slowAOM_{raman} \tag{B.5}$$

$$Slowing_1 = v1 + 2 * slowAOM_1 \tag{B.6}$$

$$Slowing_2 = v2 + 2 * slowAOM_2 \tag{B.7}$$

And the final frequencies for the MOT are:

$$MOT_0 = Toptica + motAOM_0 \tag{B.8}$$

$$MOT_1 = v1 + motAOM_1 \tag{B.9}$$

$$MOT_2 = v2 + motAOM_2 \tag{B.10}$$

Because the slowing lasers need to change frequency, the lasers are shifted by modifying $offsetAOM_{raman}$, $slowAOM_1$, and $slowAOM_2$. Because we want the Toptica laser to stay fixed, $VCO_{toptica}$ is also scanned.

B.2 Comb

Two parameters determine the frequencies of our comb teeth, the carrier offset frequency f_{co} and the repetition rate f_{rep}, such that any tooth can be described as $f_{tooth} = f_{co} + n * f_{rep}$ for integer n. Incidentally, this is true for the "doubled" comb as well, because addition happens with and between all teeth when doubling. Typically, we lock f_{co} to a couple tens of MHz, while f_{rep} ($\approx$ 99.5 MHz) is phase locked to (1 GHz - f_{synth})/10, where the 1 GHz signal comes from the Wenzel oscillator.

B.3 Raman Laser

The Raman laser consists of a 1228 nm seed laser which is then Raman amplified and doubled up to 614 nm for use in slowing. We choose lock the 1228 nm seed laser to the comb directly in the infrared, reducing the need to double the 1228 nm section of the comb spectrum. The optical setup is shown in Figure B.1. The double pass AOM before the comb beat allows the comb/1228 nm beat note to remain still as we vary the diode laser frequency.

Figure B.1: Optical setup for the Raman laser

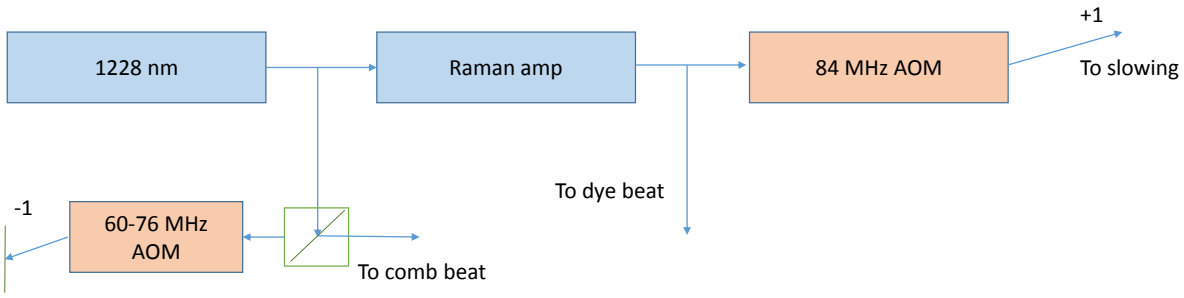

B.4 Toptica Laser

The Toptica laser is locked to the Raman laser after the Raman laser has been doubled to the visible. The optical setup for the toptica laser is shown in Figure B.2 In order to keep the Toptica laser stationary in frequency, the beatnote between the raman and dye laser is then mixed with a VCO which we scan from ∼230 MHz to ∼160 MHz. The resultant signal is then locked to ∼-30 MHz.

Figure B.2: Optical setup for the Toptica laser

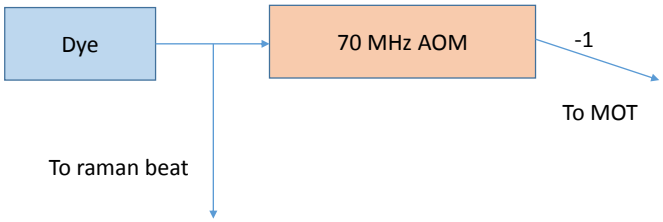

B.5 v=1 Laser

The v=1 master laser is locked to the comb light that has been doubled up to the visible, using a PPLN doubling crystal. In order to scan the frequency of the slowing repump light, the double passed AOM frequency is changed before seeding the tapered amplifier. The optical setup before the TAs is shown in Figure B.3.

Figure B.3: Optical setup for v=1 repump

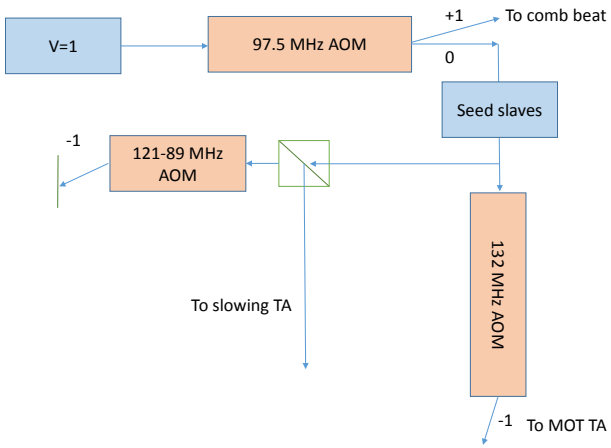

B.6 v=2 Laser

The locking setup for v=2 is very similar to that of v=1, its optical setup is shown in Figure B.4.

Figure B.4: Optical setup for v=2

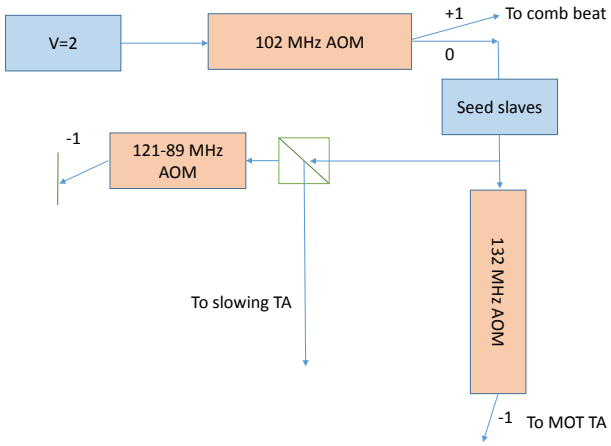

Appendix C

PMT characterization and transimpedance amplifier

We want our PMT to collect all incident photons, be insensitive to MCS discriminator level, have photon shot-noise limited error bars, and not have many coincident clicks (indicating we should be in current integration, not photon counting mode) We found that our previous mode of operation was very sensitive to MCS discriminator level, and did not register all counts. We were using a Hamamatsu R10699 PMT driven at 1000 Volts without any sort of transimpedance amplifier after it, and a MCS discriminator level of -2.6 mV falling, likely too close to the noise floor. In graphs, this will be labeled no amp 1000V.

We tried out a few different things to improve its performance: running the PMT at a higher voltage, as well as using a transimpedance amplifier on the output with a few different gains. (by changing R18 in the diagram C.1, at values of 226 ohms, 330 ohms, and 450 ohms)

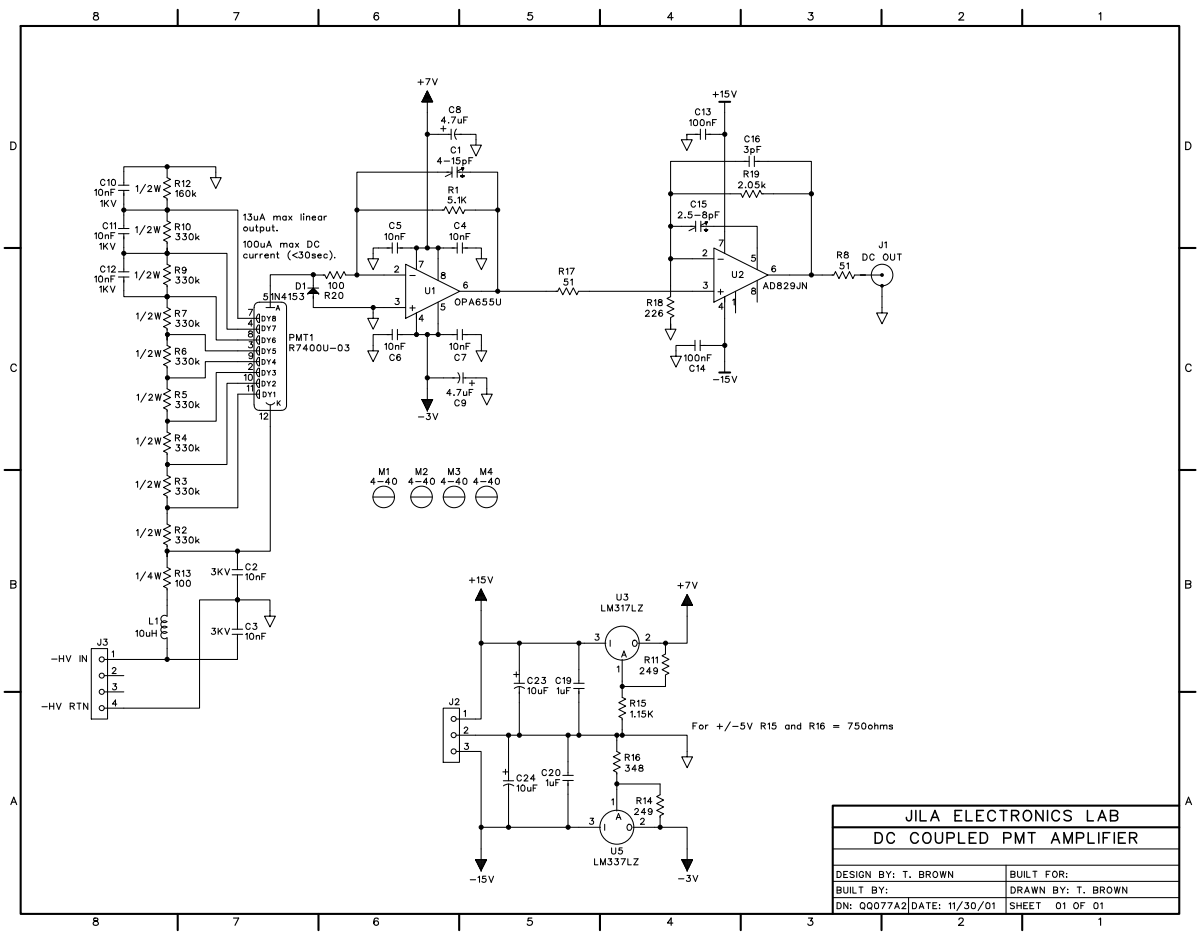

Figure C.1: Circuit schematic for PMT transimpedance amplifier.

In the remaining graphs please note that we tried to increase the light scatter for a given MOT beam power above what is normal by opening up all MOT beam irises and fully opening the PMT iris to give ourselves the largest range. Our usual operating conditions are more like the 5 mW scatter shown here than the 25 mW, even though we usually run with 20-30 mW per beam during MOT data collection.

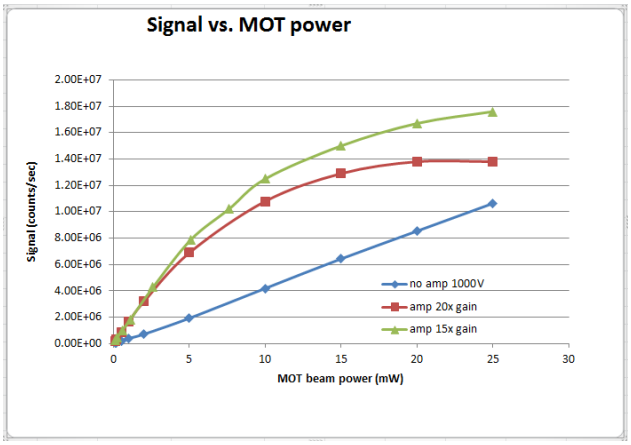

Figure C.2: Photons counted vs MOT beam laser power for different transimpedance amplifier gains.

By looking at signal counted vs photons applied in Figure C.2we can see that we were definitely missing counts with no amplifier, on the order of a factor of 4 (depending on beam power) We can also see that with the amplifier, particularly with the 20 x gain, that we are saturating the MCS's ability to distinguish separate counts at high (larger than 10^7)count rates.

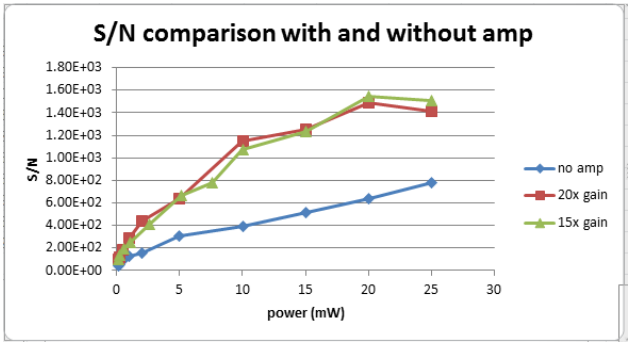

Figure C.3: Signal to noise ratio, for same acquisition time, for different amplifier gains vs laser beam powers.

We can also look at the signal to noise for these different scenarios, as in Figure C.3 Here we see that signal to noise is improved with the amplifier as opposed to without it. Now it is important to determine why the signal to noise ratio is better, so we check the exponent of the dependence on signal by putting them on a log-log plot, as in FigureC.4. looking at the fit, we see that all cases

show a 0.5 power scaling (for powers in the 0-5 mW regime. using the amplifier above 5 mW we see an increase in the exponent), indicating the noise is behaving as shot noise. The increased signal to noise ratio with the amplifier is then because we are collecting more photons with the amplifier as opposed to without it.

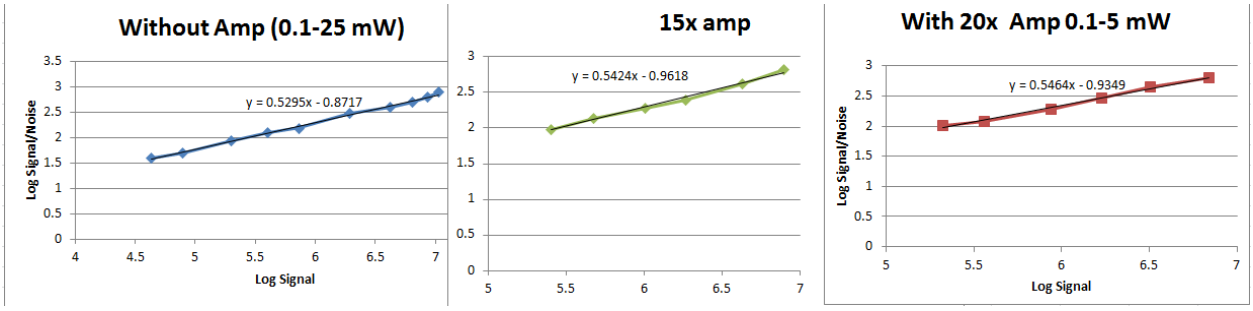

Figure C.4: Log-log plot of signal/noise vs signal for different transimpedance amplifier gains. All are well fit with y=.5x +b function, implying a square root dependence on signal/noise on signal.

Regarding sensitivity to discriminator level: we want ourselves to be in a situation where small dc fluctuations don't drastically alter our count rate. So, by parking at 5 mW and changing the discriminator level we can see how sensitive we are, as shown in Figure C.5. This shows that even running at a higher voltage still leaves us with a narrow window where our count rate is flat with respect to discriminator voltage, whereas using the amplifier can decrease our sensitivity to electrical pickup. We also find that running the amp at 10x gain doesn't bring the count rate up as high as with 15x or 1200 volts.

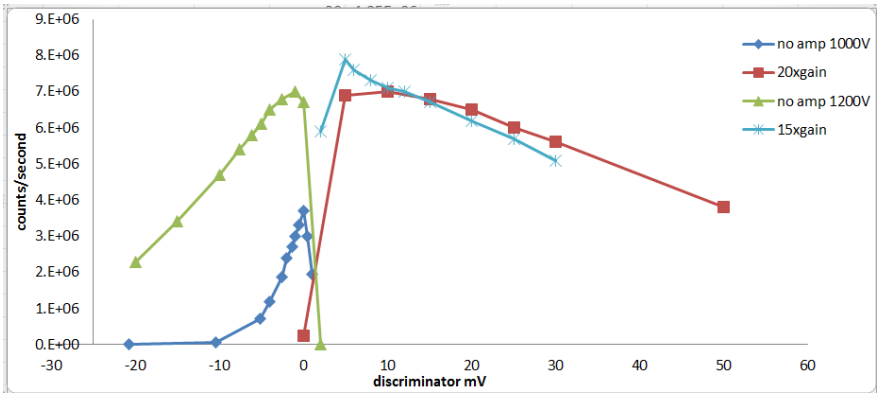

Figure C.5: Counts registered by MCS vs discriminator level for various PMT voltages and transimpedance amplifier gains.

MCS settings currently in use:

10.24 us, 16k bins per record trigger 2 volts rising discriminator level 10 mV rising 15x transimpedance amplifier 1000 V supply for PMT

Appendix D

Data Acquisition

D.1 Introduction

The primary ways in which we analyze our experiment is through the photons collected by either the photomultiplier tube (PMT) or the CCD camera both of which are directed at the MOT region. The PMT allows time-sensitive detection, while the CCD can give us spatially dependent information. However, in addition to these two devices, we also have the ability to change many aspects of how our experiment is run, which we achieve through the use of a PulseBlaster timing card, a couple of function generators, and some digital electronics. All the various components are controlled through a series of Matlab GUIs. In this section I detail how these various components interact with each other and enable us to run our experiment as desired. I also give a brief overview of how we typically process the data acquired in this way.

D.2 Acquisition devices

D.2.1 CCD

We have a CCD camera aimed at the MOT region, with a field of view of approximately 1 cm by 1 cm. We can pull frames off of the camera and directly onto the computer. Setting up the CCD to acquire data is achieved through the Matlab GUI, as shown in Figure D.1. From the GUI we can turn the cooler on and off and set the set temperature (usually -30 degrees C) We can tell the camera how many exposures to expect and how long the exposures should be. Finally, we can

Figure D.1: GUI for interfacing with the CCD

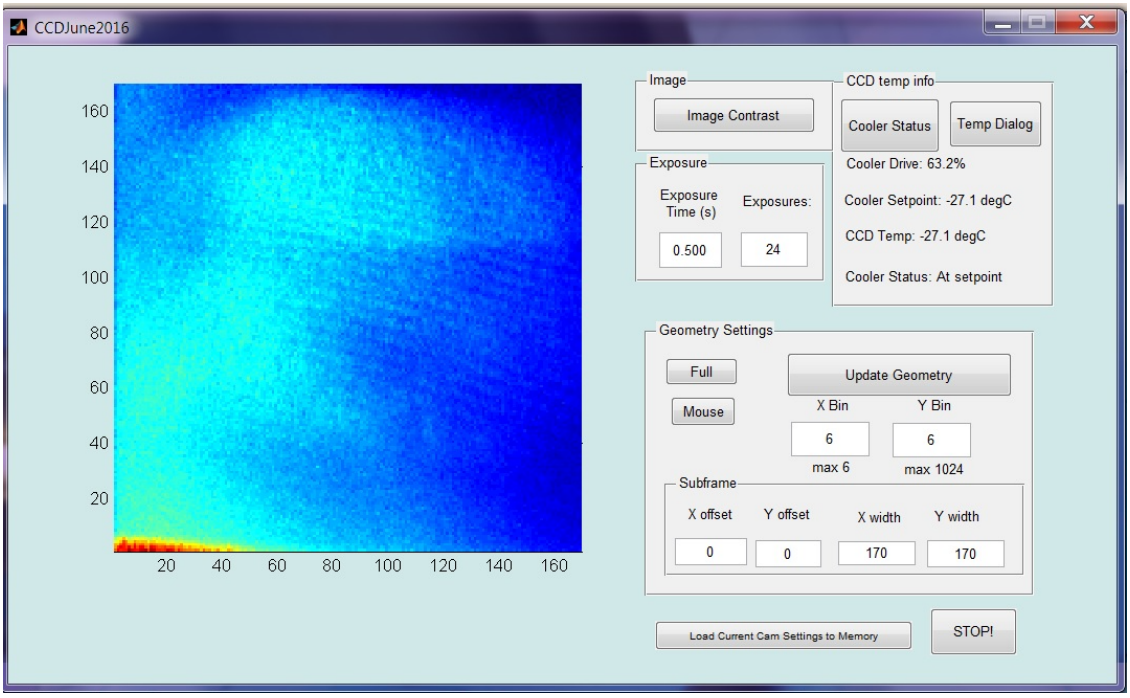

specify the region of interest on the sensor, and the on-chip binning. By allowing the camera to do binning itself, we can reduce the amount of time it takes to transfer data from the camera to the computer, as well as reduce the readout noise. The total number of camera pixels are 1024 by 1024. The camera can bin over entire rows, but has a maximum binning of 6 columns. We typically run with 6 by 6 binning, which yields 170 by 170 binned pixels. After modifying the geometry settings, the Update Geometry button must be pressed to load the settings. The left side of the GUI displays the first frame of the most recently aquired data, which can be useful for troubleshooting.

D.2.2 PMT

We have a photomultiplier tube that is looking at the MOT region. Its signal is then amplified and then plugged into the multichannel scaler (MCS) which records the voltage spikes as photon counts. There are no parameters to be set for the PMT itself.

D.2.3 Multi-channel scaler

The MCS is a photon counting device that accumulates data into time bins. Upon receiving a trigger, it starts accumulating. The total number of bins can be set to be any multiple of 1024 from 1 to 16. We typically run with 10 μs bins, and 9216 bins. With repeated triggers, the MCS continues to accumulate photon counts into the same bins until it reaches the specified number of records for which to acquire, and so the final signal is the total number of photon counts per bin over all the records. We usually convert this total number into a number of counts per second, in order to more easily compare values across different data sets which may have different numbers of records per acquisistion. Since the screen is not functional, all communication with the MCS is done via GPIB through Matlab.

D.2.4 Scope

When performing Doppler scans with the dye laser, we apply a sinusoidal voltage scan to the VCO that sets the offset between the dye laser and the raman laser. In order to know what frequency the laser is at what time, we put the VCO control voltage on the scope and save the scope trace in the data file, to later be able to plot signal vs VCO frequency (or velocity). The only parameter we usually change is the number of triggers the scope will average over (The number of averages field of the GUI shown in Figure D.2) Typically this is best matched to the number of records that the MCS is acquiring for. We have not been using the FastFrame capability within the last few years.

Figure D.2: GUI for interfacing with the TDS7104 scope

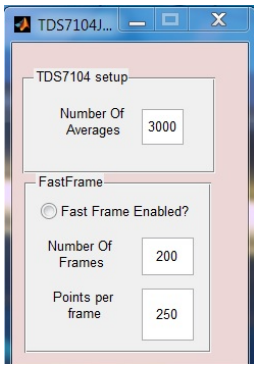

D.3 Control

The timing control of our system is controlled through a variety of elements. In this section I step through the various components and explain their use in running the experiment.

D.3.1 Digital Delay Generators

The master timing of our experiment is controlled through a digital delay generator (DDG) running at 10 Hz. This master DDG is continuously running and triggers things that prefer not to be interrupted. For example, we fire the YAG ablation laser every 100 ms regardless of whether the rest of the experiment is running, as it helps keep the optical power of the YAG more constant. This master DDG also usually triggers any voltage chirps (explained further in the function generator subsection). Finally, when we are running, the master DDG triggers a secondary DDG when we decide to run the whole experiment through the use of an AND gate (explained further in the Arduino subsection). This secondary DDG is used to trigger the PulseBlaster timing card.

D.3.2 PulseBlaster Timing Card

The timing card (a programmable TTL pulse generator) is used to control all other triggered parts of our experiment. For example, we trigger the MCS and CCD via the timing card, as well as shutters for slowing, phase switching of the MOT coils, and to turn off the 760 MHz hyperfine component when doing Doppler-sensitive detection. The timing card is programmed via a gui, but

once a program is loaded it is then triggered via a DDG. I'll go into more detail of the programming of the PulseBlaster in a later section.

D.3.3 PulseBlaster breakout board

The first 12 of the timing card outputs are broken out to various BNC outputs on the breakout board. All channels are default TTL low except when set high by the timing card. Some of the channels have been set up with a rotary switch. For these channels, we have an additional level of control available. These channels have 5 choices of settings: normal, on, off, not, and toggle. Normal means that the channel is triggered via the timing card as expected. On and off settings override the timing card settings, forcing that TTL high or low always (for on and off settings respectively). The not setting gives the inverse of the signal determined by the timing card (high when set low, and low when set high). Thus the timing is still controlled by the timing card, but the inverse of the usual setting. Finally, the toggle setting means that the channel goes through an AND gate with the Toggle Out signal from the MCS. I'll go into more detail on the Toggle output of the MCS later, but this means that the channel is triggered with the set timing when the MCS Toggle output is high, but is not triggered when the Toggle output is low. All channels without rotary switches are controlled solely from the timing card settings. Channels 13-24 have not yet been necessary, and so have not been broken out to BNC outputs.

D.3.4 Function generators

We have three function generators we use to manipulate the experiment. The Lecroy function generator is used to sinusoidally vary a voltage which is then combined with a voltage to form the dye-raman offset VCO control voltage. Because of the setup of our frequency locking scheme, this then sinusoidally scans the dye laser frequency. This laser can then be utilized to perform Doppler-sensitive detection of multiple velocities in a single data acquisition. We currently program the Lecroy function generator by hand, setting it to a sin output in gated mode. The timing of the scan can then be triggered by a channel on the timing card.

The second function generator that we use is the Tegam, which provides the control voltage for our slowing chirps. It is programmed via a GUI, as shown in Figure D.3. The GUI allows

Figure D.3: GUI for interfacing with the Tegam function generator

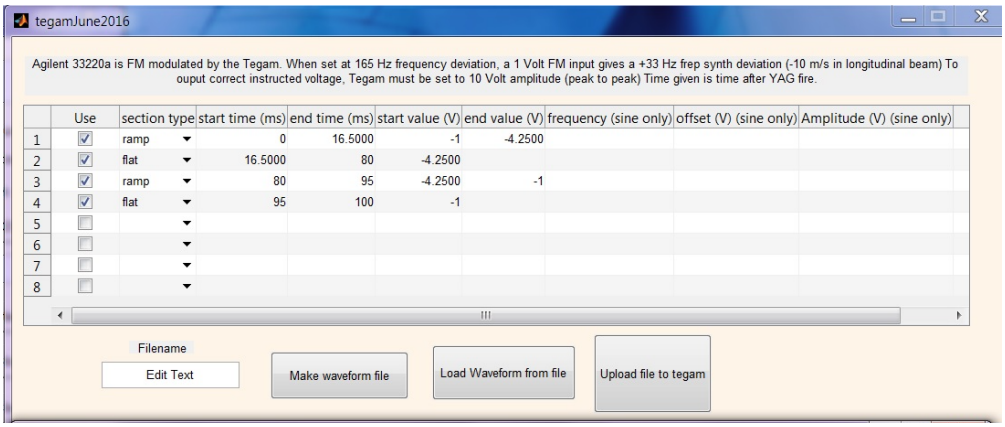

programming of flat sections and ramps of arbitrary timing. A waveform file must first be made, and then can be uploaded to the function generator. The Tegam is then be triggered by the master DDG.

Finally, we can set the Agilent synthesizer (which determines the value of f_{rep}) via the Agilent GUI. It will likely break the lock if this frequency is changed while f_{rep} is locked. Opening the GUI will read the current value of the synthesizer, allowing the value to be saved with the data files.

D.3.5 Arduino

We have a couple of Arduino controlled TTLs that can be talked to via Matlab. The GUI allows control of the Yag shutter and the timing card. The timing card is triggered when it's channel is high AND the master DDG hits time 0. The Yag shutter channel goes through an OR gate with the timing card Yag control.

D.3.6 Altbins box

The box has a switch on the front to be in "normal" or "altbins" mode. When in normal mode, the PMT signal goes directly to the MCS. When in altbins mode, the bin clock signal and

the Toggle out of the MCS go through an XOR gate, which then gates the PMT signal to the MCS. Note, the bin clock output is NIM logic, not TTL. We use a comparator in the altbins box to convert it to a TTL signal.

D.4 Data acquisition modes

In order to have flexibility when acquiring data, several different acquisition modes have been implemented.

D.4.1 MCS acquisition modes

The MCS can be set in three different modes: add, external, and toggle. This is controlled via the MCS gui in Matlab.

Add mode means that every record's bins are added to the total. This can be considered the default operation of the MCS.

External mode means the MCS checks the TTL status of its Subtract input at the time of the trigger, and if the input is high it will subtract photons counted from each bin, while if the input is low it will add photon counts to each bin as in add mode. We control this TTL with the "MCS subtract" channel on the timing card. When the MCS is not in external mode, the status of this TTL has no effect.

Toggle mode is one wherein the MCS controls its own addition and subtraction. In this mode we need to set the toggle number (N). For the first N records the MCS acquires it will subtract photon counts from its bins, while for the second N records it will add photons counted to bins. This continues until the MCS has reached the total number of records it is acquiring for. It is important to note that if the total records is not divisible by 2N, the number of added and subtracted records will not be the same, which is usually not desired. In Toggle mode the MCS also changes the state of its Toggle output synchronously with the records it is acquiring. The Toggle out will be TTL high when the MCS is subtracting and TTL low when adding. We utilize the Toggle out in a couple of ways. After buffering, it goes into the altbins box and the timing card breakout board. It is used

in the altbins box as discussed in subsection D.3.6. The toggle out is utilized with the timing card breakout board as discussed in subsection D.3.3. More information about the MCS can be found in its user manual here.

D.4.2 PulseBlaster acquisition modes

The timing card can be utilized in two main ways, single-state or multi-state. If the number of states is set to one, timing will be uploaded in single state mode, while if the number of states is another number, timing will loaded to the board in multi-state mode.

Single-state mode uploads a single sequence to the timing board, that will be looped over until either the CCD or MCS (or both, depending on which are enabled) have been triggered as many times as they are expecting. Upon pressing Acquire Data in the Master GUI, the timing card is enabled by setting the Arduino timing card output high, allowing the timing card to be triggered by the secondary DDG. Once the MCS or CCD have enough records or exposures respectively, they report back to the main program that they are done, and the timing card is turned off again.

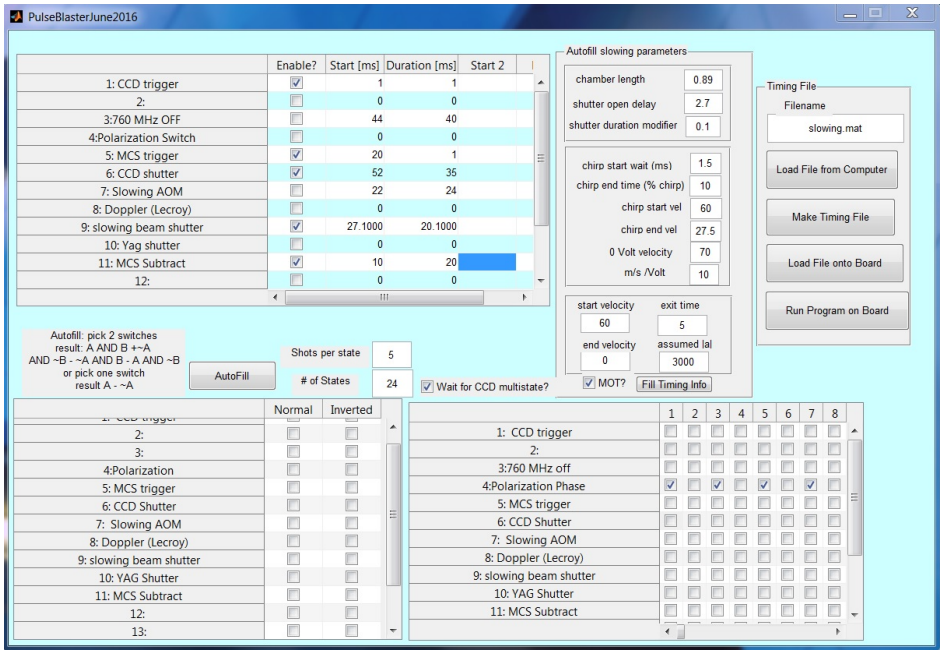

Figure D.4: GUI for interfacing with the PulseBlaster timing card

The sequence that is loaded is determined by the table in the upper left of the PulseBlaster GUI, as shown in Figure D.4. If the checkbox for a channel is not enabled, it will remain TTL low always. If the checkbox is enabled, then the channel will have a pulse at the time marked by start and lasting for the time labelled duration, after each time that the timing card is triggered. Here it is important to note that according to the timeframe of the timing card, the YAG trigger is fired at 20 ms. We incorporate this 20 ms delay to allow for things like the MCS subtract pulse, which need to be active before the experimental time 0. Additionally, it is necessary to not have the total time (start plus duration) for any channel to exceed the experimental rep rate, as the timing card cannot accept a new trigger while it is already running. When running at our usual 10 Hz, that means that no total times can exceed 100 ms.

Multi-state mode The Multi-state mode works very simlarly to single-state mode, with two notable exceptions. The first is the use of the "inhibit checkboxes" table in the lower right of the GUI. The inhibit checkboxes table has as many columns as the number of states specified. Each state will last for the number of shots entered in the shots per state box. If a box is checked in the inhibit checkboxes, that channel will not be triggered during that state. For example, if the slowing shutter box is checked for state number two, but not for state number one, the slowing shutter will be triggered as specified by its start and duration time given in the upper left table for the N shots per state. Then for the next N shots the slowing shutter will be inhibited, and so will not fire. The pattern entered into the inhibit checkboxes has no restriction.

The second difference between single and multi-state mode is that two channels become special when in checkbox mode, those are the YAG channel and the phase switch channel. When multiple states are used, these two channels will remain high or low for the entirety of the shots in that state, and will not obey the timing shown in the durations table in the upper left. Thus, if the YAG shutter has a checkbox for state 1, it will remain closed for all shots during that state. If it is not checked for state 2, it will remain open for all of state 2. Similarly if we have the phase switch channel checked, it will remain TTL low for the entire state.

When loading timing files for multi-state mode, we sometimes wish to use the CCD. If we

are using the CCD, the checkbox for "wait for CCD multistate" must be checked in order to allow time to offload data from the CCD before starting the next exposure. If we are not using the CCD, there is no need to wait for this time, and so the box should not be checked.

No matter the timing card mode, when uploading a timing file to the timing card, all the following buttons must be pressed in order: Make Timing File, Load File onto Board, and Run Program on Board. If all of these are not done, the behavior of the timing card will not be as expected.

Appendix E

Replacing Y_2O_3 targets in the cell

E.1 Epoxying targets

We epoxy the Y_2O_3 targets to a brass ring prior to placing them in the chamber. By affixing the targets to a removable piece, we are better able to glue up new targets while the old ones are in the chamber, as well as not have to fight against gravity. The cell is made out of copper, with a one inch hole bored perpendicular to the molecular beam direction. The brass ring is just smaller than one inch allowing it to fit snugly in the cell. We chose brass because it is well expansion matched to copper under thermal cycling, but easier to machine. Also, when removing old targets from a ring we do some mechanical scraping to remove old epoxy, and the brass holds up better than copper.

The epoxy we use is Stycast 2850 with catalyst 23LV. This epoxy/catalyst combination has good cryogenic properties as well as thermal cycling properties. The epoxy needs to be mixed according to weight in a well ventilated area, as the catalyst is rather noxious. We then epoxy two targets to the brass ring, being careful to have neither the targets nor the epoxy extend beyond the edge of the ring, or it has to be sanded off before it will fit in the cell. We use a small teflon spacer the same depth as the ring in order to hold up the targets while the epoxy dries. The cure time is usually overnight, though it can be rushed to a few hours by using a hot plate.

E.2 Disassembling

The targets are inserted in the cryostat from the side opposite the YAG beam, so that the ablated molecules can start in the middle rather than the outer edge of the cell. The first step (after

warming up the chamber and purging it with helium) is to remove the rectangular side vacuum flange on far side from the YAG. The flange is fastened with 10-32 bolts.

Figure E.1: vacuum chamber disassembly for target removal

(a) outer rectangular flange

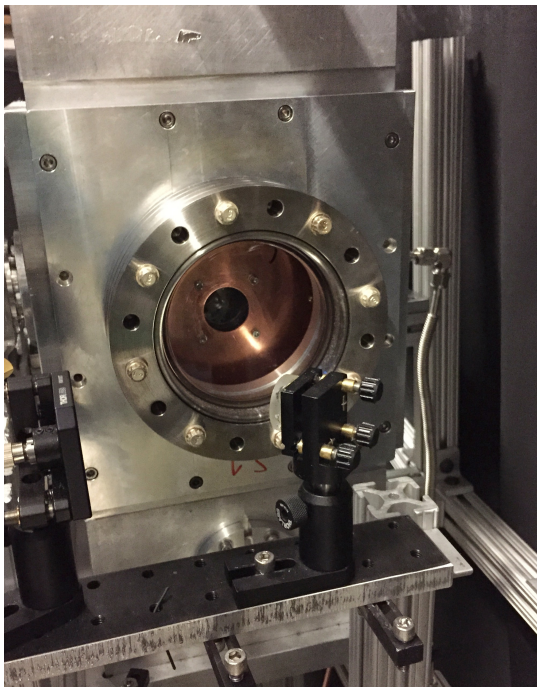

(b) 40 K shield

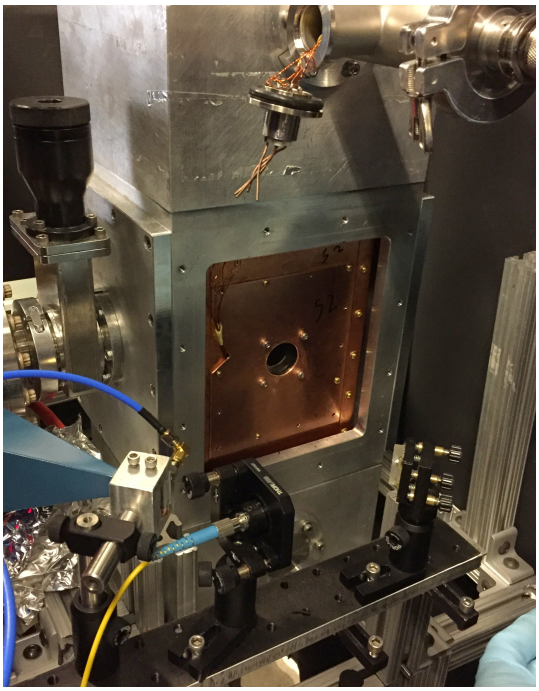

After removal of the flange, the 40 K shield is visible, and can be removed with a small screwdriver. Then the 4 K charcoal fin will be apparent, affixed with three screws at its top.

At this point, one can finally see the cell itself. Now is a good time to put tin foil down below the cell to prevent things like screws from falling down into the cryostat. The window can be carefully removed with a balldriver, but it is important to note that the window is not rigidly attached to the brass mount, it is just held in place with a thin layer of Kapton film between the window and the brass. After extricating the window, the brass ring with the targets can be accessed. It is sometimes fit in there snugly, so a short allen key can be used to try to pry the ring out. Now is a good time to take a look at the far window and see if it needs replacement due to accumulation of a film or haze that appears after many ablations. If it does, the other side is disassembled in much the same way.

Figure E.2: vacuum chamber disassembly for target removal

(a) 4 K fin

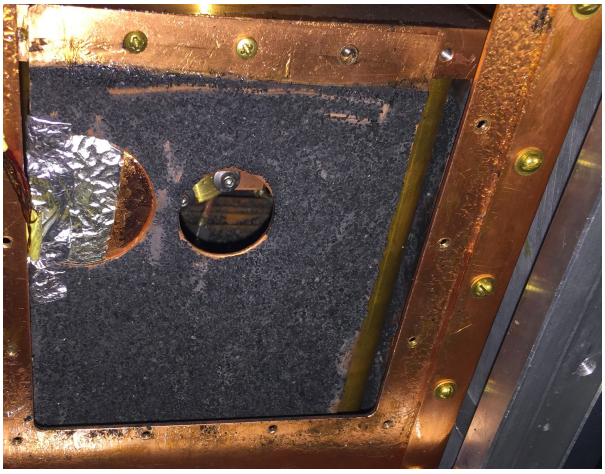

(b) cell with window

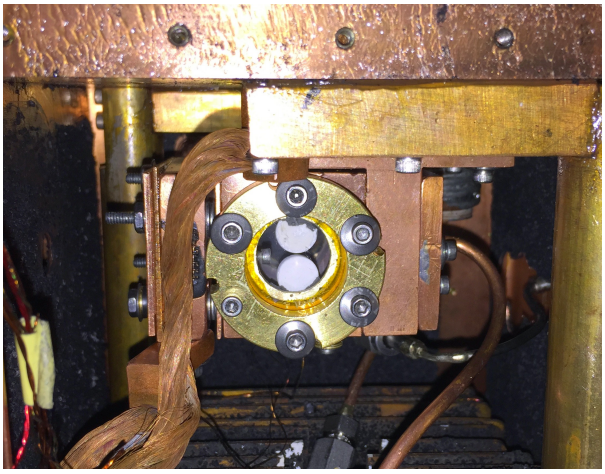

Figure E.3: vacuum chamber disassembly for target removal

(a) cell without window

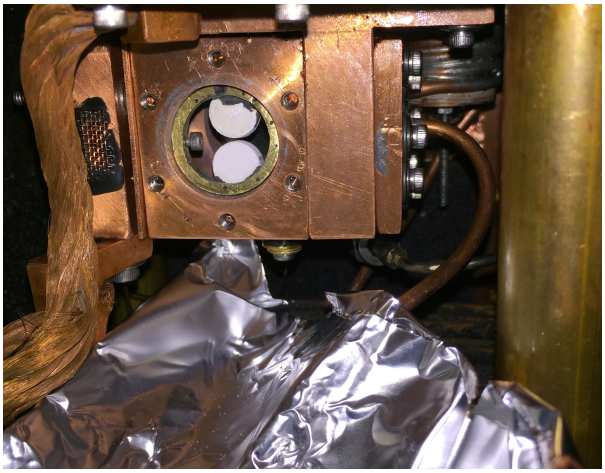

(b) empty cell

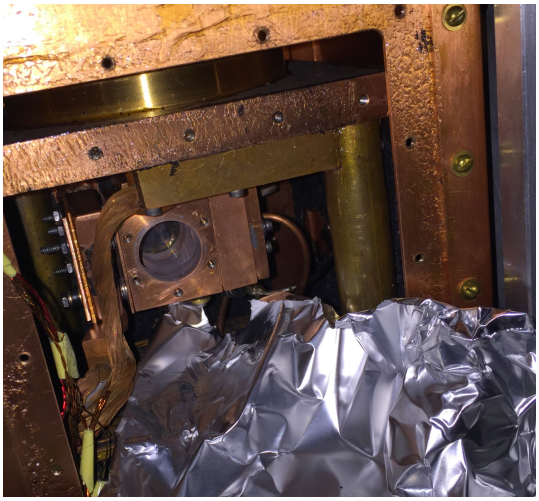

E.3 Reassembling

Now the entire process can be reversed to put in the new targets. When reinstating the 4 K fin and the 40 K shield, if more thermal grease is needed then more can be applied. We use Apiezon N for its good cryogenic properties. When placing the final vacuum flange on, it is important not to overtighten the bolts, as the cryostat is made of aluminum and we do not want to strip the holes.

Bibliography

[1] J. Baron, W. C. Campbell, D. DeMille, J. M. Doyle, G. Gabrielse, Y. V. Gurevich, P. W. Hess, N. R. Hutzler, E. Kirilov, I. Kozyryev, B. R. O'Leary, C. D. Panda, M. F. Parsons, E. S. Petrik, B. Spaun, A. C. Vutha, and A. D. West. Order of magnitude smaller limit on the electric dipole moment of the electron. Science, 343(6168):269–272, 2014.

[2] H. Loh, K. C. Cossel, M. C. Grau, K.-K. Ni, E. R. Meyer, J. L. Bohn, J. Ye, and E. A. Cornell. Precision spectroscopy of polarized molecules in an ion trap. Science, 342(6163):1220–1222, 2013.

[3] J. J. Hudson, D. M. Kara, I. J. Smallman, B. E. Sauer, M. R. Tarbutt, and E. A. Hinds. Improved measurement of the shape of the electron. Nature, 473(7348):493–6, May 2011.

[4] B. Yan, S.A. Moses, B. Gadway, J.P. Covey, K.R.A. Hazzard, A. Rey, D.S. Jin, and J. Ye. Observation of dipolar spin-exchange interactions with lattice-confined polar molecules. Nature, 501(7468):521–525, September 2013.

[5] S. Ospelkaus, K.-K. Ni, D. Wang, M. H. G. de Miranda, B. Neyenhuis, G. Quemener, P. S. Julienne, J. L. Bohn, D. S. Jin, and J. Ye. Quantum-state controlled chemical reactions of ultracold potassium-rubidium molecules. Science, 327(5967):853–857, 2010.

[6] M. T. Bell and T. P. Softley. Ultracold molecules and ultracold chemistry. Mol. Phys., 107(2):99–132, 2009.

[7] K.-K. Ni, S. Ospelkaus, M. H. G. de Miranda, A. Pe'er, B. Neyenhuis, J. J. Zirbel, S. Kotochigova, P. S. Julienne, D. S. Jin, and J. Ye. A high phase-space-density gas of polar molecules. Science, 322(5899):231–235, 2008.

[8] R. E. Smalley, L. Wharton, and D. H. Levy. Molecular optical spectroscopy with supersonic beams and jets. Acc. of Chem. Res., 10(4):139–145, 1977.

[9] N. R. Hutzler, H. Lu, and J. M. Doyle. The buffer gas beam: An intense, cold, and slow source for atoms and molecules. Chem. Rev., 112(9):4803–4827, 2012. PMID: 22571401.

[10] M. I. Fabrikant, T. Li, N. J. Fitch, N. Farrow, J. D. Weinstein, and H. J. Lewandowski. Method for traveling-wave deceleration of buffer-gas beams of ch. Phys. Rev. A, 90:033418, Sep 2014.

[11] S. Y. T. van de Meerakker, N. Vanhaecke, H. L. Bethlem, and G. Meijer. Transverse stability in a stark decelerator. Phys. Rev. A, 73:023401, Feb 2006.

[12] E. Narevicius, A. Libson, C. G. Parthey, I. Chavez, J. Narevicius, U. Even, and M.G. Raizen. Stopping supersonic oxygen with a series of pulsed electromagnetic coils: A molecular coilgun. Phys. Rev. A, 77:051401, May 2008.

[13] S. Chervenkov, X. Wu, J. Bayerl, a. Rohlfes, T. Gantner, M. Zeppenfeld, and G. Rempe. Continuous Centrifuge Decelerator for Polar Molecules. Phys. Rev. Lett., 112(1):013001, Jan 2014.

[14] Hsin-I Lu, Ivan Kozyryev, Boerge Hemmerling, Julia Piskorski, and John M. Doyle. Magnetic trapping of molecules via optical loading and magnetic slowing. Phys. Rev. Lett., 112:113006, Mar 2014.

[15] M.D. Di Rosa. Laser-cooling molecules. Eur. Phys. J. D, 31(2):395–402, 2004.

[16] B.K. Stuhl, B. C. Sawyer, D. Wang, and J. Ye. Magneto-optical trap for polar molecules. Phys. Rev. Lett., 101:243002, 2008.

[17] E S Shuman, J F Barry, and D DeMille. Laser cooling of a diatomic molecule. Nature, 467(7317):820–823, October 2010.

[18] J. F. Barry, E. S. Shuman, E. B. Norrgard, and D. DeMille. Laser Radiation Pressure Slowing of a Molecular Beam. Phys. Rev. Lett., 108(10):103002, March 2012.

[19] V. Zhelyazkova, A. Cournol, T. E. Wall, A. Matsushima, J. J. Hudson, E. A. Hinds, M. R. Tarbutt, and B. E. Sauer. Laser cooling and slowing of CaF molecules. Phys. Rev. A, 89(5):053416, May 2014.

[20] M. Yeo, M.T. Hummon, A.L. Collopy, B. Yan, B. Hemmerling, E. Chae, J.M. Doyle, and J. Ye. Rotational state microwave mixing for laser cooling of complex diatomic molecules. In preparation.

[21] M.T. Hummon, M. Yeo, B.K. Stuhl, A.L. Collopy, Y. Xia, and J. Ye. 2d magneto-optical trapping of diatomic molecules. Phys. Rev. Lett., 110:143001, Apr 2013.

[22] J. F. Barry, D. J. McCarron, E. B. Norrgard, M. H. Steinecker, and D. DeMille. Magneto-optical trapping of a diatomic molecule. Nature, 512(7514):286–289, August 2014.

[23] S. Truppe, H. J. Williams, M. Hambach, L. Caldwell, N. J. Fitch, E. A. Hinds, B. E. Sauer, and M. R. Tarbutt. Molecules cooled below the doppler limit. Nature Physics, 13:1173 EP –, 08 2017.

[24] Loïc Anderegg, Benjamin L. Augenbraun, Eunmi Chae, Boerge Hemmerling, Nicholas R. Hutzler, Aakash Ravi, Alejandra Collopy, Jun Ye, Wolfgang Ketterle, and John M. Doyle. Radio frequency magneto-optical trapping of caf with high density. Phys. Rev. Lett., 119:103201, Sep 2017.

[25] Ivan Kozyryev, Louis Baum, Kyle Matsuda, Benjamin L. Augenbraun, Loic Anderegg, Alexander P. Sedlack, and John M. Doyle. Sisyphus laser cooling of a polyatomic molecule. Phys. Rev. Lett., 118:173201, Apr 2017.

[26] M. A. Chieda and E. E. Eyler. Prospects for rapid deceleration of small molecules by optical bichromatic forces. Phys. Rev. A, 84:063401, Dec 2011.

[27] A. M. Jayich, A. C. Vutha, M. T. Hummon, J. V. Porto, and W. C. Campbell. Continuous all-optical deceleration and single-photon cooling of molecular beams. Phys. Rev. A, 89:023425, Feb 2014.

[28] H. Metcalf. Entropy exchange in laser cooling. Phys. Rev. A, 77:061401, Jun 2008.

[29] D. J. McCarron, M. H. Steinecker, Y. Zhu, and D. DeMille. Magnetically-Trapped Molecules Efficiently Loaded from a Molecular MOT. ArXiv e-prints, December 2017.

[30] L. Anderegg, B. L. Augenbraun, Y. Bao, S. Burchesky, L. W. Cheuk, W. Ketterle, and J. M. Doyle. Laser Cooling of Optically Trapped Molecules. ArXiv e-prints, March 2018.

[31] S Truppe, H J Williams, N J Fitch, M Hambach, T E Wall, E A Hinds, B E Sauer, and M R Tarbutt. An intense, cold, velocity-controlled molecular beam by frequency-chirped laser slowing. New Journal of Physics, 19(2):022001, 2017.

[32] H. Katori, T. Ido, Y. Isoya, and M. Kuwata-Gonokami. Magneto-optical trapping and cooling of strontium atoms down to the photon recoil temperature. Phys. Rev. Lett., 82:1116–1119, Feb 1999.

[33] T. H. Loftus, T. Ido, A. D. Ludlow, M. M. Boyd, and J. Ye. Narrow line cooling: Finite photon recoil dynamics. Phys. Rev. Lett., 93:073003, Aug 2004.

[34] Alejandra L Collopy, Matthew T Hummon, Mark Yeo, Bo Yan, and Jun Ye. Prospects for a narrow line mot in yo. New Journal of Physics, 17(5):055008, 2015.

[35] T. H. Loftus, T. Ido, M. M. Boyd, A. D. Ludlow, and J. Ye. Narrow line cooling and momentum-space crystals. Phys. Rev. A, 70:063413, Dec 2004.

[36] A. J. Berglund, J. L. Hanssen, and J. J. McClelland. Narrow-line magneto-optical cooling and trapping of strongly magnetic atoms. Phys. Rev. Lett., 100:113002, Mar 2008.

[37] P. M. Duarte, R. A. Hart, J. M. Hitchcock, T. A. Corcovilos, T.-L. Yang, A. Reed, and R. G. Hulet. All-optical production of a lithium quantum gas using narrow-line laser cooling. Phys. Rev. A, 84:061406, Dec 2011.

[38] P. Villwock, S. Siol, and Th. Walther. Magneto-optical trapping of neutral mercury. Eur. Phys. J. D, 65(1-2):251–255, 2011.

[39] M. Lu, N. Q. Burdick, S. H. Youn, and B. L. Lev. Strongly dipolar bose-einstein condensate of dysprosium. Phys. Rev. Lett., 107:190401, Oct 2011.

[40] A. Frisch, K. Aikawa, M. Mark, A. Rietzler, J. Schindler, E. Zupanič, R. Grimm, and F. Ferlaino. Narrow-line magneto-optical trap for erbium. Phys. Rev. A, 85:051401, May 2012.

[41] J. M. Brown and Al. Carrington. Rotational Spectroscopy of Diatomic Molecules. Cambridge University Press, 2003.

[42] W. J. Childs, O. Poulsen, and T. C. Steimle. Fine and magnetic hyperfine structure in the $A^2\Pi$ and $X^2\Sigma_+$ states of yttrium monoxide. J. Chem. Phys., 88(2):598–606, 1988.

[43] A. Bernard and R. Gravina. The emission spectrum of yttrium monoxide - new rotational and vibrational results on the $A^2\Pi$-$X^2\Sigma_+$ system. Astrophys. J. Supp. S., 52:443–450, August 1983.

[44] C.L. Chalek and J.L. Gole. Chemiluminescence spectra of ScO and YO: Observation and analysis of the AΔ, XΣ band system. J. Chem. Phys., 65:2845, 1976.

[45] D. J. Berkeland and M. G. Boshier. Destabilization of dark states and optical spectroscopy in zeeman-degenerate atomic systems. Phys. Rev. A, 65:033413, Feb 2002.

[46] M. Prentiss, A. Cable, J.E. Bjorkholm, S. Chu, E.L. Raab, and D. E. Pritchard. Atomic-density-dependent losses in an optical trap. Opt. Lett., 13(6):452–454, 1988.

[47] E. B. Norrgard, D. J. McCarron, M. H. Steinecker, M. R. Tarbutt, and D. DeMille. Submillikelvin dipolar molecules in a radio-frequency magneto-optical trap. Phys. Rev. Lett., 116:063004, Feb 2016.

[48] M. R. Tarbutt. Magneto-optical trapping forces for atoms and molecules with complex level structures. page 12, August 2014.

[49] V. B. Tiwari, S. Singh, H. S. Rawat, and S. C. Mehendale. Cooling and trapping of ^{85}Rb atoms in the ground hyperfine $f = 2$ state. Phys. Rev. A, 78:063421, Dec 2008.

[50] J A Devlin and M R Tarbutt. Three-dimensional doppler, polarization-gradient, and magneto-optical forces for atoms and molecules with dark states. New Journal of Physics, 18(12):123017, 2016.

[51] M. Yeo. The laser cooling and the magneto-optical trapping of the YO molecule . PhD thesis, University of Colorado Boulder, 2015.

[52] H. Lu, J. Rasmussen, M.J. Wright, D. Patterson, and J.M. Doyle. A cold and slow molecular beam. Phys. Chem. Chem. Phys., 13:18986–18990, 2011.

[53] J. Barry. Laser cooling and slowing of a diatomic molecule. PhD thesis, Yale University, 2013.

[54] M. Schioppo, N. Poli, M. Prevedelli, St. Falke, Ch. Lisdat, U. Sterr, and G. M. Tino. A compact and efficient strontium oven for laser-cooling experiments. Review of Scientific Instruments, 83(10):103101, 2012.

[55] Eunmi Chae, Loic Anderegg, Benjamin L Augenbraun, Aakash Ravi, Boerge Hemmerling, Nicholas R Hutzler, Alejandra L Collopy, Jun Ye, Wolfgang Ketterle, and John M Doyle. One-dimensional magneto-optical compression of a cold caf molecular beam. New Journal of Physics, 19(3):033035, 2017.

[56] S. Truppe, M. Hambach, S. M. Skoff, N. E. Bulleid, J. S. Bumby, R. J. Hendricks, E. A. Hinds, B. E. Sauer, and M. R. Tarbutt. A buffer gas beam source for short, intense and slow molecular pulses. Journal of Modern Optics, 65(5-6):648–656, 2018.

[57] E. Chae. Laser Slowing of CaF Molecules and Progress towards a Dual-MOT for Li and CaF. PhD thesis, Harvard University, 2015.

[58] R.C. Dye, R.E. Muenchausen, and N.S. Nogar. Laser ablation of y2o3 in an oxygen atmosphere. Chemical Physics Letters, 181(6):531 – 536, 1991.

[59] Darko Kajfez. Q factor measurements , analog and digital. 1999.

[60] R. V. Pound. Electronic frequency stabilization of microwave oscillators. Review of Scientific Instruments, 17(11):490–505, 1946.

[61] B. Simard, A.M. James, P.A. Hackett, and W.J. Balfour. On the $A'^2\Delta$-$X^2\Sigma_+$(0,0) band of YO. J. Mol. Spectrosc., 154(2):455 – 457, 1992.

[62] K. Liu and J. M. Parson. Laser fluorescence detection of nascent product state distributions in reactions of Sc and Y with O_2, NO, and SO_2. J. Chem. Phys., 67(5):1814–1828, 1977.

[63] A.L.G Rees. The calculation of potential-energy curves from band-spectroscopic data. Proc.Phys. Soc., 59(6):998, 1947.

[64] P. Sriramachandran and R. Shanmugavel. Spectroscopic parameters for certain band systems of astrophysically important molecule: Yttrium oxide. New Astron., 16(2):110 – 113, 2011.

[65] R. D. Suenram, F. J. Lovas, G. T. Fraser, and K. Matsumura. Pulsed nozzle Fourier transform microwave spectroscopy of laser evaporized metal oxides: Rotational spectra and electric dipole moments of YO, LaO, ZrO, and HfO. J. Chem. Phys., 92(8):4724–4733, 1990.

[66] A. Bernard, R. Bacis, and P. Luc. Astrophys. J., 227:338–348, January 1979.

[67] H.J. Metcalf and P. van der Straten. Laser Cooling and Trapping. 1999.

[68] Matthew A Norcia, Julia R K Cline, John P Bartolotta, Murray J Holland, and James K Thompson. Narrow-line laser cooling by adiabatic transfer. New Journal of Physics, 20(2):023021, 2018.

[69] J. A. Muniz, M. A. Norcia, J. R. K. Cline, and J. K. Thompson. A Robust Narrow-Line Magneto-Optical Trap using Adiabatic Transfer. ArXiv e-prints, June 2018.

[70] L. Cheng. Coupled-cluster calculations for low-lying electronic states of heavy-metal containing molecules. ISMS, 2018.

[71] B. K. Stuhl, M. T. Hummon, M. Yeo, G. Quemener, J. L. Bohn, and J. Ye. Evaporative cooling of the dipolar hydroxyl radical. Nature, 492(7429):396–400, December 2012.

[72] L. Scharfenberg, H. Haak, G. Meijer, and S. Y. T. van de Meerakker. Operation of a stark decelerator with optimum acceptance. Phys. Rev. A, 79:023410, Feb 2009.

[73] R. Grimm, M. Weidemüller, and Y. B. Ovchinnikov. Optical Dipole Traps for Neutral Atoms. Advances in Atomic Molecular and Optical Physics, 42:95–170, 2000.

[74] D. J. McCarron, E. B. Norrgard, M. H. Steinecker, and D. DeMille. Improved magneto-optical trapping of a diatomic molecule. ArXiv e-prints, December 2014.